2013

Tunnel-diode resonator and nuclear magnetic resonance studies of low-dimensional magnetic and superconducting systems

Steven Lee Yeninas
Iowa State University

Tunnel-diode resonator and nuclear magnetic resonance studies of low-dimensional magnetic and superconducting systems

by

Steven Lee Yeninas

A dissertation submitted to the graduate faculty
in partial fulfillment of the requirements for the degree of
DOCTOR OF PHILOSOPHY

Major: Condensed Matter Physics

Program of Study Committee:
Ruslan Prozorov, Co-major Professor
Yuji Furukawa, Co-major Professor
Marshall Luban
Adam Kaminski
John Lajoie
Gordon Miller

Iowa State University
Ames, Iowa
2013

DEDICATION

I dedicate this work to Anton and Margie Rebel. I miss you Grandpa.

TABLE OF CONTENTS

LIST OF TABLES

LIST OF FIGURES

ACKNOWLEDGEMENTS

I must express my deepest gratitude to my advisers Prof. Ruslan Prozorov and Prof. Yuji Furukawa, and my undergraduate adviser Prof. Jose Lozano. I would also like to include a special thanks to Prof. Marshall Luban and Dr. Makariy Tanatar for our countless conversations, and the large role they played throughout my graduate studies. The time, guidance, patience, support, and the vast research and collaboration opportunities they provided to develop me as a well-rounded young scientist have also left me a more humble and worldly human being.

I also extend a very special thanks to my group members Dr. Hyunsoo Kim, Dr. Kyuil Cho, Dr. Catalin Martin, Prof. Matt Vannette, Prof. Ryan Gordon, (soon to be Dr.) Beas Roy, rest of the Prozorov lab, as well as Dr. Michael Baker and Dr. Lorenzo Bordonali for their help and guidance around the laboratory.

I would like to express my very great appreciation to a number of individuals who offered support throughout my graduate education. I am grateful to Professors John Lajoie, Gordon Miller, and Adam Kaminski for serving on my Program of Study Committee. I am very grateful to Dr. William A. Coniglio and Prof. Chuck Agosta from Clark University, and Oscar Dr. Ayala Valenzuela, Jon Betts, Prof. James Brooks, Dr. Neil Harrison, Dr. Ross McDonald, and Dr. Chuck Mielke from the National High Magnetic Field Laboratory at Los Alamos National Laboratory. Their support and the opportunities to work at these pulsed field facilities were invaluable professional experiences. I must also thank the number of collaborators who have provided samples, experimental help, theoretical support, or just guidance and conversations. I especially need to acknowledge Prof. Richard Winpenny and Dr. Grigore Timco for the Cr-based

magnetic molecule samples; Professors Larry Engelhardt, J$\acute{}$urgen Schnack, and Christian Schr$\acute{}$oder for their theoretical support; and Prof. David Johnston and Dr. Abhishek Pandey for the $BaKMn_2As_2$ samples; also Professors David Vaknin, Ferdinando Borsa, Daniel Procissi, and countless others. The genuine kindness and support demonstrated within the scientific community exceeded any expectations and I am glad to call these people friends.

I also wish to extend a heartfelt thank you to the hundreds of friends throughout the world from grade school and my time at Bradley and Iowa State who have supported, sacrificed, and helped me maintain sanity throughout my education. This includes my long time friend Brian Pierce, and high school teachers Howie Perlow and Bryan Wright. Without their friendship and guidance I certainly would never have pursued such a lofty academic achievement. I must also thank Kevin Walat who has proved time and time again that he is the best friend a guy could ask for. Kevin, I hope some day I can be there for you as much as you have been there for me. To Megan Flannery, not a day goes by that I don't think of you. I will forever value our friendship and this work will forever serve as a bittersweet symbol of the times and memories we shared together.

Lastly, I wish to thank all my family who have done everything possible to help me along my journey. I must thank my father and mother for all their love and support, as well as my brothers Jason and Ryan, and my sister Alicia. I must also thank Grandpa and Grandma Yeninas and Grandma and Grandpa Rebel. It is with great sadness that Grandpa Rebel and Grandma Yeninas could not see me graduate, both of whom I've lost in just this last year. I cherish every moment and memory I have of them. To Grandpa Rebel, you were my hero and role model. Everyday, I wake up aspiring to become even half the man you were; this is only one small step. Finally, I am especially grateful to Selena Russell and the relationship we have built over the last six years. Selena, you are my foundation, my dearest friend, and I could never have done this without you. I look forward to building our future together.

ABSTRACT

This thesis emphasizes two frequency-domain techniques which uniquely employ radio frequency (RF) excitations to investigate the static and dynamic properties of novel magnetic and superconducting materials. The first technique is a tunnel-diode resonator (TDR) which detects bulk changes in the dynamic susceptibility, $\chi = dM/dH$. The capability of TDR to operate at low temperatures (less than 100 mK) and high fields (up to 65 T in pulsed fields) was critical for investigations of the antiferromagnetically correlated magnetic molecules $Cr_{12}Cu_2$ and $Cr_{12}Ln_4$ (Ln = Y, Eu, Gd, Tb, Dy, Ho, Er, Yb), and the superconductor $SrFe_2(As_{1-x}P_x)_2$ ($x = 0.35$). Investigations of $Cr_{12}Cu_2$ and $Cr_{12}Ln_4$ demonstrates the first implementation of TDR to experimentally investigate the low-lying energy spectra of magnetic molecules in pulsed magnetic fields. Zeeman splitting of the quantum spin states results in transitions between field-dependent ground state energy levels observed as peaks in dM/dH at 600 mK, and demonstrate good agreement with theoretical calculations using a isotropic Heisenberg spin Hamiltonian. Increasing temperature to 2.5 K, TDR reveals a rich spectrum of frequency-dependent level crossings from thermally populated excited states which cannot be observed by many conventional static magnetometry techniques. The last study presented uses TDR in pulsed fields to determine the temperature-dependent upper-critical field H_{c2} to investigate the effects of columnar defects arising from heavy ion irradiation of $SrFe_2(As_{1-x}P_x)_2$. Results suggest irradiation uniformly suppresses T_c and H_{c2}, and does not introduce additional features on $H_{c2}(T)$ and the shapes of the anisotropic H_{c2} curves indicates a nodal superconducting gap. The second technique is nuclear magnetic resonance (NMR) which yields site specific magnetic and electronic information arising from hyperfine in-

teractions for select magnetic nuclei. NMR spectra and nuclear spin-lattice relaxation measurements are reported for the geometrically frustrated magnetic molecule $W_{72}V_{30}$, and for $BaMn_2As_2$ and $Ba_{1-x}K_xMn_2As_2$ (with K-concentration x = 0.04 - 0.40) which are analogs of the high T_c iron arsenides. For the magnetic molecule $W_{72}V_{30}$, ^{1}H and ^{51}V NMR and DC magnetization were used to investigate geometric frustration arising from antiferromagnetic interactions between 30 V^{4+} ions occupying the edge sites of an icosidodecahedron. This system serves as a molecular representation of the 2-dimensional kagome lattice whose finite-size allows precise quantum calculations. Analysis of $W_{72}V_{30}$ data suggests a large distribution of exchange values are necessary to characterize the field and temperature-dependent magnetic properties. For the insulating $BaMn_2As_2$ and hole-doped metallic $Ba_{1-x}K_xMn_2As_2$, both local moment antiferromagnets, ^{55}Mn and ^{75}As NMR spectra and spin-lattice relaxation rates $1/T_1$ were conducted to investigate the local magnetic and electronic properties as a function of K-concentration x. NMR independently confirms G-type antiferromagnetism from spectra measurements, while a Korringa relation in $1/T_1$ indicates conduction electrons in both the Mn $3d$ and As $4d$ orbitals. The observation of ferromagnetic enhancement of the ^{55}Mn NMR signal and no appreciable shift observed in the ^{75}As spectra, combined with the absence of a structural phase transition in neutron diffraction measurements suggests, the K-doped system may exhibit a previously unseen coexistence of local-moment antiferromagnetism from the Mn^{2+} moments and weak ferromagnetism, possibly arising from the Mn $3d$ orbitals. In summary, the data presented in this work demonstrates the diversity of novel materials and physical properties which can be investigated by the RF techniques TDR and NMR.

CHAPTER 1. INTRODUCTION

The development of new radio-frequency (RF) techniques and novel materials have played a pivotal role in the world's modern technology-driven economy. Extensive research efforts to further understand the basic physical properties of magnetism and superconductivity, especially those derived from rare-earth materials such as the neodymium magnet $Nd_2Fe_{14}B$ (abbreviated as NdFeB) where the $4f$ Nd ion features a large axial anisotropy, have and will continue to drive advancements in such areas as computers, motors, generators, and clean energy technologies such as wind turbines, photovoltaics, and electric vehicles. It is important for physicists to delve deeper into understanding the quantum mechanics of the natural world, for this fundamental research into the small scale is a necessary precursor for big innovation. Historically Ames Laboratory has been at the forefront of rare earth materials' science and technology since its establishment during the Manhattan Project after developing an efficient process for producing large quantities of high-purity rare-earth elements. The commitment and strong research record of The Ames Laboratory and Iowa State University were recently (January 2013) recognized by the U.S. Department of Energy through establishing an Energy Innovation Hub to continue this research. This initiative highlights the importance of collaboration between public and private institutions in understanding and developing new energy critical-materials.

This thesis focuses on RF spectroscopic techniques to investigate systems spanning two major and closely intertwined areas of condensed matter physics: magnetism and superconductivity. The remainder of this chapter will focus on basic introductions and

motivations for this work. Chapter 2 will introduce the fundamental principles for a tunnel-diode resonator (TDR) and nuclear magnetic resonance (NMR), the two primarily employed RF techniques used in this thesis. Chapters 3, 4, and 5 will discuss the experimental investigations of magnetic molecules, classified by their organometallic structures which prevent long range magnetic ordering. The macroscopic magnetic properties of these systems can be characterized by the microscopic magnetism of each individual molecule. Chapters 3 and 4 focus on a class of magnetic molecules known as antiferromagnetic (AFM) rings, which can be treated as a 1-dimensional chain of magnetic ions. Chapter 5 focuses on a member of a family of spherical molecules known as Keplerates where antiferromagnetically interacting ions occupy the edge sites of corner-sharing triangles resulting in geometric spin frustration. Chapter 6 and 7 focus on further understanding the origins of superconductivity for systems with the same structure as the family of high-T_C '122' superconductors. Chapter 6 investigates a system which does not exhibit superconductivity, but whose properties share those of both the high-T_C cuprates and iron arscenides. Chapter 7 investigates the effects of heavy-ion irradiation on superconductivity by investigating the temperature-dependent upper critical field. Chapter 8 ends with a general conclusion.

The work in Chapters 3, 4, and 5 center around a class of molecule based magnets spawned from advancements in organometallic chemistry over the last few decades. Molecule based magnets feature a lattice of molecules where each molecule contains a cluster of magnetic ions (often $3d$ transition metals) bridged by organic ligands and can be created with a variety of shapes, symmetries, and magnetic ions: 1D rings, 3D cubes and spheres, $3d$ transition metals and $4f$ rare-earth elements [4–6]. These so called magnetic molecules - or single molecule magnets (SMMs) for systems with high spin ground states - are characterized as nanometer-scale magnets which act as zero-dimensional model systems. The macroscopic magnetic properties are governed by the local-moment magnetic behavior of each microscopic molecule with total spin ground states ranging

from zero to high spin states, up to 51/2 for Mn25 [7]. Magnetic molecules typically experience relatively strong intramolecular magnetic exchange interactions, compared to very weak intermolecular interactions which are shielded by large organic ligand shells. The finite size of the spin clusters allows direct comparisons between direct diagonalization of isotropic spin Hamiltonian quantum calculations and experimental results. The discussion of magnetic molecules in this work investigates issues in magnetism such as transitions from classical to quantum behavior, the spectrum of discrete low-lying energy levels, and critical slowing down and spin dynamics by studying two classes of molecules: 1) structures which are an extension of AFM rings featuring a 1-dimensional array of magnetic ions and 2) quasi-spherical Keplerate structures to understand the physical characteristics of geometric frustration arising from ions at edge sites of corner sharing triangles with competing AFM interactions. Some of the many technological implications of quantum devices tied to further understanding the magnetic properties of magnetic molecules include spintronics, magnetic recording, ultrafast switches, and possible application as qubits for quantum computational technology [8, 9].

Chapter 3 looks to establish TDR as a spectroscopic probe of the low lying energy levels while simultaneously validating the use of quantum Monte Carlo simulations using a simple isotropic Heisenberg Hamiltonian in the special case where intermolecular interactions, anisotropy, and Dzyaloshinsky Moriya interactions are ignored. Using pulsed magnetic fields at low-temperatures, TDR investigates $Cr_{12}Cu_2$, effectively a 1-dimensional heterometallic magnetic molecule featuring Cr^{3+} ions with $S = 3/2$ and Cu^{2+} ions with $S = 1/2$. TDR measurements detects multiple temperature-dependent peaks. It will be shown that these correspond to ground state and excited state level crossings, in good agreement with analysis from QMC.

Chapter 4 introduces Ln ions to Cr_6 "horseshoes" in the form $Cr_{12}Ln_4$ (Ln = Y, Eu, Gd, Tb, Dy, Ho, Er, and Yb) to further understand the nature of $3d - 4f$ interactions. Ln ions are a powerful tool for effectively tuning a number of physical parameters such

as unit cell size, size of the local moment and anisotropy, and magnetic Curie or Neél ordering temperatures in conventional intermetallic compounds [10–14]. This poses the question of whether introducing various Ln ions would systematically alter the zero-field energy levels in magnetic molecules? There is also great interest in developing systems with Ising type anisotropy as observed in Nd for NdFeB for developing more powerful and energy efficient magnets. It will be shown that switching between Ln ions in the magnetic molecule does not have the effect of tuning the low lying energy levels, but rather increases them indiscriminately.

Chapter 5 looks at ^{51}V and ^{1}H NMR to investigate $W_{72}V_{30}$, an icosidodecahedron system which serves as a finite-sized analog to the 2-dimensional kagomé lattice of interlocking pentagons and triangles [15, 16]. Due to the low spin $S = 1/2$ for V^{4+} ions, it is possible to conduct highly accurate quantum calculations rather than being limited to classical approximations, despite the large dimension for the Hilbert space (2^{30} =1,073,741,824) [17, 18]. Surprisingly, this system does not observe field induced steps in the magnetization as a result of quantum spin transitions determined for a regular icosidodecahedron with a single nearest-neighbor exchange interaction. Instead the system exhibits an inhomogeneous distribution of V-V exchange constants which vary by as much at 30%.

Chapters 6 and 7 work to understand the origins of high-temperature superconductivity in the family with $ThCr_2Si_2$-type structure 122 iron pnictides. For these systems, the onset of superconductivity has been observed by hole-doping with alkali earth metals, transition metal substitutions, isoelectron substitution, and under high pressure. Chapter 6 uses ^{55}Mn and ^{75}As NMR spectrum and relaxation measurements to study the electronic and magnetic properties of $Ba_{1-x}K_xMn_2As_2$. While this system does not demonstrate superconductivity, the properties of the parent compound and hole doped compound span those of the two well studied families of high-T_C superconductors. Results suggest a previously unobserved coexistence of local moment antiferromagnetism

and itinerant ferromagnetism arising from the Mn ions. In Chapter 7 we found evidence that columnar defects in the structure for isolectron P-substituted $SrFe(As_{1-x}P_x)_2$ caused by heavy ion irradiation suppress T_c and H_{c2} in the anisotropic nodal superconductor using TDR in pulsed magnetic fields up to 65 T.

1.1 Introduction to Magnetism

The magnetic susceptibility is typically defined for a collection of spins by the change in magnetization (M) versus a change in magnetic field (H). This is defined in differential form as

$$\chi = \frac{\partial M}{\partial H}. \tag{1.1}$$

If H is sufficiently weak or T sufficiently large then χ can be characterized independent of H, $M = \chi H$. The magnitude of χ is typically comprised from the sum of all magnetic contributions in the sample, however, the dominant terms typically arise from ions with unpaired electrons. The interesting physics discussed in this work arise from the magnetic susceptibility of correlated magnetic moments and to less extent the non-interacting paramagnetic susceptibility at high temperatures, in contrast to the diamagnetic susceptibility arising from filled electron orbitals, typically weaker by several orders of magnitude.

If we consider a magnetic system with an energy spectrum $E_n(n = 0, 1, 2, \dots)$ in an external magnetic field H, then the microscopic magnetization for each energy level is given as

$$\mu_n = -\frac{\partial E_n}{\partial H}. \tag{1.2}$$

The macroscopic magnetization could then be expressed in terms of the classical Boltzmann distribution,

$$M = N_A \langle \mu_n \rangle = N_A \frac{\sum_n (-\partial E_n/\partial H) exp(-E_n/k_B T)}{\sum_n exp(-E_n/k_B T)}, \tag{1.3}$$

where k_{B} is the Boltzmann constant, N_A is Avogadro's number, H is an applied magnetic field, T is the temperature, and the summation in the denominator is defined as the partition function Z. The magnetization M and susceptibility χ can be expressed in terms of the partition function as

$$M = N_A k_B T \frac{\partial \ln Z}{\partial H}, \tag{1.4}$$

and

$$\chi = N_A k_B T \frac{\partial^2 \ln Z}{\partial H^2}. \tag{1.5}$$

From Eqn. (1.4), it follows that the field dependent magnetization per unit volume V can be expressed in terms of the total angular momentum J as

$$M = \frac{N}{V}(g\mu_B J)B_J(\beta g\mu_B JH). \tag{1.6}$$

where μ_{B} is the Bohr magneton, g is the Landé g-factor (typically ≈ 2), $\beta = 1/k_B T$, and $B_J(x)$ is the Brillouin function defined by

$$B_J(x) = \frac{2J+1}{2J}\coth\frac{2J+1}{2J}x - \frac{1}{2J}\coth\frac{1}{2J}x. \tag{1.7}$$

with $x = \beta g\mu_B JH$.

In the special case of high fields or low temperatures ($x \gg 1$), $B_J(x) \simeq 1$, corresponding to magnetic saturation $M = \frac{N}{V}(g\mu_B J)B_J$. On the other hand, at low fields and high temperatures ($x \ll 1$) the function $B_J(x)$ can be written as $B_J(x) \approx \frac{1}{3}(1+\frac{1}{J})x + \ldots$ resulting in a collection of non-interacting spins. In the limit of low fields and high temperatures, the susceptibility is inversely proportional to T and expressed in the simple form

$$\chi = \frac{C}{T}. \tag{1.8}$$

This expression is known as Curie's law with constant C given by

$$C = n\frac{N_A(g\mu_B)^2}{3k_B}J(J+1), \tag{1.9}$$

where n is the number of spin moments per molecule and J is the total angular moment. It is convenient to note that $N_A\mu_B^2/3k_B \approx 0.125 = 1/8$ in cgs·emu units.

If the system experiences an interaction between magnetic moments then it is necessary to modify the Curie law in Eqn. (1.8). The magnetic susceptibility for interacting systems (FM or AFM) can be treated to good approximation in the paramagnetic region above the ordering temperature (T_c of T_N) by the Curie-Weiss law. The Curie-Weiss law is given as

$$\chi = \frac{C}{T - \Theta}. \tag{1.10}$$

Here θ is the characteristic Weiss temperature given by

$$\Theta = \frac{zJ(J+1)J_{ex}}{3k_B}, \tag{1.11}$$

where z is the number of nearest neighbors, J is the total orbital angular momentum, and J_{ex} is the magnitude of the exchange energy. Positive values of θ (i.e. positive J_{ex}) typically correspond to ferromagnetic ordering, while negative values indicate antiferromagnetic ordering. The magnitude of θ often serves as good approximation for the ordering temperature. If there is no exchange energy ($J_{ex} = 0$) then the system remains in a paramagnetic state, θ goes to zero, and you recover the simple form of Curie's law.

CHAPTER 2. MEASUREMENT TECHNIQUES

2.1 Introduction

Oscillators have long served as versatile transducers for experimental measurements. The frequency of electrical oscillators can be measured with great precision and can operate in compact environments under extreme conditions, such as extremely low temperatures and high magnetic fields. Oscillators which operate in the radio-frequency (RF) range are particularly attractive for measuring an array of physical properties in solids: thermal expansion, magnetostriction, electrostriction, surface impedance, and magnetic and electric susceptibilities. Measurements of novel magnetic and superconducting materials typically examine the response of a sample's *ac* magnetic susceptibility. In conjunction with SQUID measurements, two very different RF techniques were used extensively in this work: a tunnel-diode resonator (TDR) and nuclear magnetic resonance (NMR).

While both techniques employ inductor-capacitor (LC) circuits operating in the RF range, the operating principles are drastically different. A TDR operates by detecting shifts in the resonance frequency of an LC tank circuit driven by a tunnel-diode capable of better than ppb sensitivity [19]. Measured frequency shifts for TDR reflect the net response of all quantities which affect the inductance or capacitance of the tank circuit. For this reason TDR is sometimes referred to as a 'bulk' measurement.

NMR operates by tuning an LC circuit to the Larmor frequency, for which nuclei absorb and re-emit electromagnetic radiation in an external magnetic field. [20, 21]

This resonance method allows one to isolate a particular magnetic contribution, even if relatively weak, from the total magnetic susceptibility. In practice, NMR allows a user to probe the electromagnetic environment for specific nuclei within a system whose behavior is influenced by nearby electrons through hyperfine interactions. Hence NMR is referred to as a 'local' measurement.

This chapter will discuss the operating principles of each technique.

2.2 Tunnel-diode resonator

The tunnel-diode (TD) is the main operating component of a TDR circuit first developed in 1957 by Leo Esaki while working at Tokyo Tsushin Kogyoa, the company today known as Sony. Consisting of heavily doped p- and n-type terminals, a TD is a semiconductor diode with a very narrow ($\sim$100 $\mathring{A}$) $p-n$ junction. The I-V curve for a typical TD is shown in Fig. 2.1. When a DC voltage is applied in the forward bias operation, a TD I-V curve features a region of negative differential resistance. At low voltages (< 0.5 V in Fig. 2.1) electrons from the conduction band of the n-side will tunnel to the hole states of the valence band of the p-side through the narrow $p-n$ junction, creating a forward bias tunnel current. In this region the energy of the potential barrier is high, while the energy of the electron and conduction bands overlap. As the voltage increases, the region where the energy of electrons in the conduction band overlap with the hole band starts to decrease and leads to a decrease in the tunneling current. This is the negative differential resistance region marked by the red line in Fig. 2.1. At higher voltages the potential barrier decreases and the TD produces a forward diffusion current as seen in a regular $p-n$ diode. The negative differential characteristic feature allows a TD to function as a low current ac power source capable of very fast operation ($\sim$ GHz). Esaki would later share the 1973 Nobel Prize in Physics with Ivar Giaever and Brian David Josephson for their experimental and theoretical contributions regarding electron

tunneling in semiconductors and superconductors.

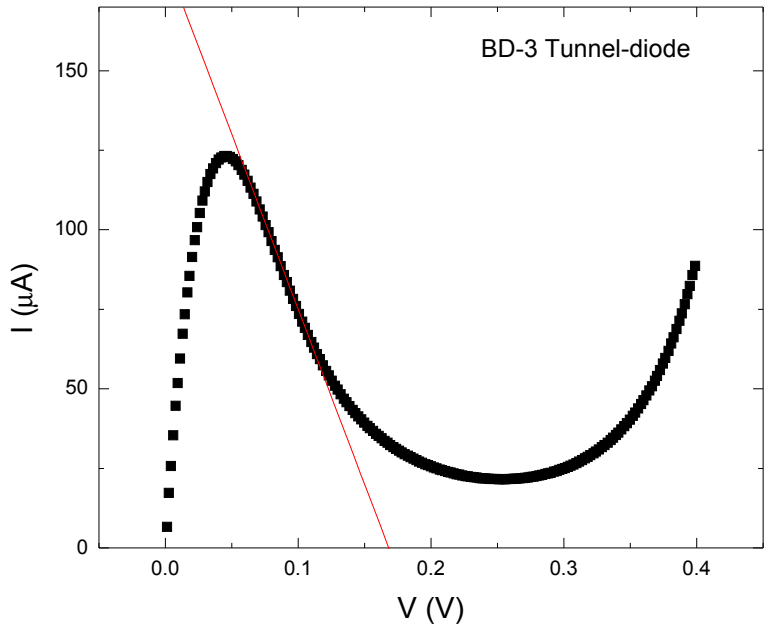

Figure 2.1: This figure shows the I-V charactersitic for a tunnel-diode for a TDR experiment. The red line highlights the characteristic negative differential resistance region. A bias voltage set in this region allows a tunnel-diode to act as an ac power source.

TDR was extensively developed as an experimental probe starting in the 1970's. Early setups were devised for measuring NMR spectra [22, 23] and magnetic susceptibility [24–26]. The circuit design and optimization put forth by Van Degrift [27] has largely served as a model for the circuit designed for this study. His setup was designed to measure changes in dielectric constants down to liquid helium temperatures with part-per-billion sensitivity.

This work primarily focuses on TDR as an instrument for measuring magnetic susceptibility for isolated magnetic clusters which experience antiferromagnetic or ferromagnetic exchange couplings. The robust performance of TDR is ideal for these systems as measurements often require extremely low temperature ranges (T down to 0.05 mK in a

dilution refrigerator) and extremely high magnetic fields (up to 65 T in pulsed magnetic fields). The last chapter uses TDR as a means of determining the upper-critical field H_{c2} for superconductors.

2.2.1 Operating principles of TDR

The operating principle of a TDR centers on a TD which drives a self-resonating LC tank circuit. When driving a LC tank circuit, the frequency of the *ac* current matches the resonance frequency of the LC circuit. In this sense the TDR locks on to the resonance frequency and changes in frequency are directly associated with variations of inductance or capacitance. Optimized circuits with good thermal stability can resonate in the megahertz range with a frequency stability better than 0.01 Hz.

For this work a sample is placed directly within the primary inductor coil of a TDR's LC tank circuit. The magnetic response of a sample to varying temperature (T) or an applied magnetic field (H) will change the the inductance of the primary coil, resulting in a shift of the TDR resonance frequency. This shift in the resonance frequency reflects the sample's magnetic susceptibility, $\chi(H,T)$, measured in the frequency domain. The resonant frequency for an LC circuit is expressed generally as

$$f_0 = \frac{1}{2\pi\sqrt{LC}}, \tag{2.1}$$

with inductance L and capacitance C. If a perturbation introduce a small change of inductance to $L + \Delta L$ than the shifted frequency can be expressed as

$$f_0 + \Delta f = \frac{1}{2\pi\sqrt{(L+\Delta L)C}} = f_0(1 + \frac{\Delta L}{L})^{-1/2}. \tag{2.2}$$

By taking the binomial expansion in the case of small ΔL this term can be approximated as

$$\Delta f \approx -\frac{1}{2}\frac{\Delta L}{L} f_0. \tag{2.3}$$

The self inductance for the coil is defined by

$$L = \frac{d\Phi}{dI}, \tag{2.4}$$

where Φ is the magnetic flux through the coil and I is the *ac* current through the coil inducing the flux. The integrated magnetic flux for an empty coil is given by

$$\Phi = B_0 V_c, \tag{2.5}$$

where B_0 is the flux density from the TDR and V_c is the volume of the coil. The flux density is, generally, given by $B = H + 4\pi M$ in CGS units, and for an empty coil the flux density B_0 is equal to the magnetic field H_0, since the magnetic moment M for vacuum would be zero. For a sample in a magnetic field H_0, the flux density would be expressed as

$$B_s = H_0 + 4\pi M_s, \tag{2.6}$$

with a non-zero sample magnetization per unit volume M_s for the sample. If the sample is placed inside the TDR coil then the change in magnetic flux as a result of the sample, Φ', is given by

$$\Phi' = B_0(V_c - V_s) + B_s V_s = B_0 V_c + (B_s - B_0)V_s. \tag{2.7}$$

This expression is simply the sum of contributions from the sample and the empty coil, with sample volume V_s. Using Eqn. (2.6) we can write Eqn. (2.7) as

$$\Phi' = H_0 V_c + 4\pi M_s V_s, \tag{2.8}$$

separating contributions from the empty coil and the sample. The new inductance is given by the change in magnetic flux with a sample Φ' with respect to current. Using the chain rule this can be expressed in terms of an applied field H and simplifying we get

$$L' = \frac{d\Phi'}{dI} = \frac{d\Phi'}{dH}\frac{dH}{dI} = V_c \frac{dH}{dI} + 4\pi V_s \frac{dM_s}{dH}\frac{dH}{dI} = L + \Delta L. \tag{2.9}$$

This expresses the new inductance for a coil containing a sample in terms of the empty coil inductance, $L = V_c \frac{dH}{dI}$, and a change in this inductance arising from the sample, $\Delta L = 4\pi V_s \frac{dM_s}{dH}\frac{dH}{dI}$. From here readily we see the ratio for the change in inductance

versus the original inductance:

$$\frac{\Delta L}{L} = 4\pi \frac{V_s}{V_c}\chi'. \tag{2.10}$$

Plugging this result in to Eqn. (2.3) and rearranging we get

$$\frac{\Delta f}{f_0} \approx -\frac{4\pi}{2}\frac{V_s}{V_c}\chi', \tag{2.11}$$

which relates the change in the TDR frequency in terms of the real part of the *ac*-magnetic susceptibility χ' multiplied by a constant, where the constant is expressed simply in terms of the empty coil frequency and the volumes of the sample and the coil. It is clear from this expression that we can maximize the signal intensity (Δf) by maximizing the filling factor, V_s/V_c, and can increase the signal intensity by increasing the LC resonant frequency f_0. As a result, an increase (decrease) in the magnetic susceptibility will result in a decrease (increase) in the resonant frequency.

For measurements in this work, the *ac* magnetic field generated within the TDR coil runs collinear with applied magnetic fields so measurements reflect the real part (χ') of the complex susceptibility $\chi_{zz}(\omega) = \chi'_{zz}(\omega) + i\chi''_{zz}(\omega)$ [24]. Therefore, from linear response theory [28], TDR probes the real part of the longitudinal magnetic susceptibility given as

$$\chi_{zz}(\omega) = \chi_{zz}(0)\left[1 - i\omega \lim_{\epsilon \to 0+} \int_0^\infty dt e^{-(i\omega+\epsilon)t} \times \left(\frac{\langle S_z(0)S_z(t)\rangle - \langle S_z\rangle^2}{\langle S_z^2\rangle - \langle S_z\rangle^2}\right)\right], \tag{2.12}$$

where $\langle\rangle$ represent thermal averages, $S_z(t)$ is the time dependence of the total spin operator S_z from the Heisenberg Hamiltonian, and $\chi_{zz}(0)$ is the static susceptibility. For a purely isotropic Heisenberg system where S_z commutes with the Hamiltonian, the term $\langle S_z(0)S_z(t)\rangle$ is independent of time. Therefore $\chi_{zz}(\omega) = \chi_{zz}(0)$ and there is no frequency-dependent component for a purely isotropic Hamiltonian.

In order to observe the excited state level crossings discussed in Chapters 3 and 4, a model must allow for non-zero off diagonal matrix elements, $\langle\alpha|S_z|\beta\rangle$, arising from very

small anisotropic terms [29]. Such terms would permit a time-dependence where

$$\langle S_z(0)S_z(t)\rangle = \frac{1}{Z}\sum_{\alpha,\beta} e^{-E_\alpha/k_BT}|\langle\alpha|S_z|\beta\rangle|^2 e^{i(E_\beta-E_\alpha)t/\hbar}, \tag{2.13}$$

with $|\alpha\rangle$ and E_α, $|\beta\rangle$ and E_β denote eigenvectors and eigenenergies of the Heisenberg Hamiltonian.

For a general Hamiltonian which does not commute with S^2 andS_z, plugging Eqn. (2.13) in to Eqn. (2.12) gives

$$\chi_{zz}(\omega) = \chi_{zz}(0)\left[1 - \frac{\hbar\omega}{Z(\langle S_z^2\rangle - \langle S_z\rangle^2}\sum_{\alpha,\beta} e^{-E_\alpha/k_BT}\frac{|\langle\alpha|S_z|\beta\rangle|^2}{\hbar\omega - (E_\beta - E_\alpha)}\right], \tag{2.14}$$

with small, non-zero values for $\langle S_z(0)S_z(t)\rangle$. Thus, a TDR with resonant frequency ω will cause a resonance when $\hbar\omega \geq E_\beta - E_\alpha \approx 1$ mK at 15 MHz.

While TDR is good for determining changes in χ with high precision, assigning the absolute value for χ is often not straightforward. Absolute values are best achieved by comparing background subtracted data to DC SQUID measurements. Since a TDR measurement responds to the total change in the primary coil inductance, the frequency shift reflects the susceptibility of all magnetic components present in the coil. For example, in addition to the intrinsic magnetization of interest one may also detect other contributions which may make subtracting the background signal difficult. These contributions could include the nuclear spin moment, diamagnetic contributions, or impurity contributions to name a few. In addition, the susceptibility may exhibit a frequency dependence, and the *ac*-susceptibility measured by TDR may exhibit a non-linear response to the DC susceptibility measured by SQUID, often at low temperatures. This is perhaps from the critical slowing down of the electron spin, due to a short T_1, resulting in saturation [24]. Therefore, TDR is best suited for observing abrupt changes in susceptibility as observed in AFM spin-cluster, the second order phase change from a paramagnetic to ferromagnetic phase or normal-superconducting transitions.

2.2.2 General TDR setup

The circuit diagram for a simple TDR is shown in Fig. 2.3. The LC tank circuit consists of a primary inductor (sample coil) and capacitor represented by LP and CP, respectively. Samples are placed at the center of the sample coil which is typically a solenoid coil, however, pulsed field measurements of upper-critical fields for thin plate samples of $SrFe_2(As_{1-x}P_x)_2$ were conducted on flat "pancake" coils (see Fig. 2.2). Capacitors $C1$ ($\sim$ 50 pF) and $C2$ ($\sim$ 10 nF) act as filters to decouple the tank circuit from the room-temperature electronics. At operating frequencies the small value for $C1$ with an RF impedance of $\sim$ 320 Ω and the large value for $C2$ with an rf impedance of $\sim$ 1.5 Ω, permit only a small portion of the signal to pass up to the electronics. Resistors $R1$ and $R2$ act as voltage dividers to properly bias the tunnel-diode, and R3 acts as a parasitic resistor to reduce unwanted oscillations. The typical resistor values are: $R1 \approx 1$ kΩ; $R2$ and $R3 \approx 300\Omega$.

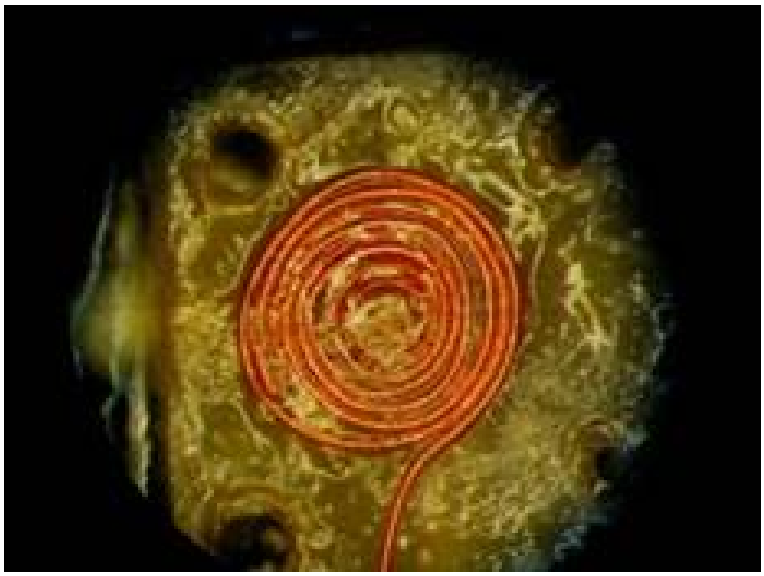

Figure 2.2: Example of a flat "pancake" coil in which a wire is wrapped in-plane around a central point increasing the radius for successive turns.

Three different TDR setups were necessary to accommodate the experimental environments and cryogenic equipment in this work. Though measurements in the dilution

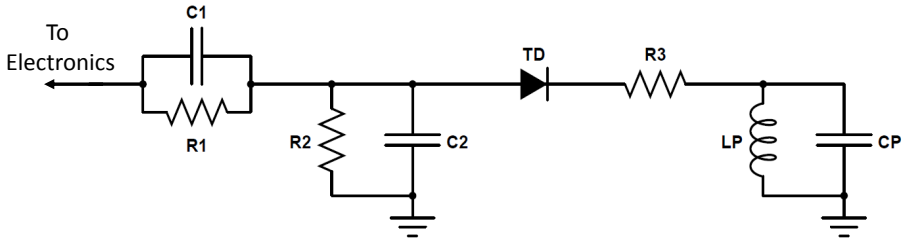

Figure 2.3: Circuit diagram for a basic TDR circuit which connects to the external hardware described in Fig. 2.4. The primary inductor LP and capacitor CP act as an LC tank circuit driven by the tunnel-diode (TD). See text for further specific component details. [Adapted from [1]]

refrigerator and pulsed fields required special designs to minimize heat load and fit in compact environments, all TDR circuits followed a similar design. A typical TDR setup operates at low temperatures with the circuit temperature stabilized, typically around 5 K, to minimize noise and drift. Temperature instabilities on the order of mK are sufficient to cause noticeable fluctuations in the resonant frequency. Therefore, precise temperature control of the circuit is extremely crucial for precision measurements.

To achieve this stability, most experimental setups are designed with several thermally decoupled stages. For example, a conventional ^{4}He cryostat operates within a temperature range from 1.5-100 K. A sample is mounted at the end of a sapphire rod which is delicately designed to slide into a thermally isolated pickup coil without making contact. The other end of the sapphire rod is mounted in a copper block with a thermometer and heater to control temperature. The sample experiences a weak thermal link with the ^{4}He "1 K pot," such that the link is strong enough to cool the sample yet weak enough to control the sample temperature with a 50 Ω resistor. The circuit is then rigidly mounted with good thermal coupling to a strong cooling source. The entire

apparatus is isolated within a vacuum can and evacuated to a typical pressure of 10^{-5} - 10^{-6} Torr. This pressure, combined with careful construction to thermally isolate the circuit from the sample, allows separate and precise control of the circuit and sample.

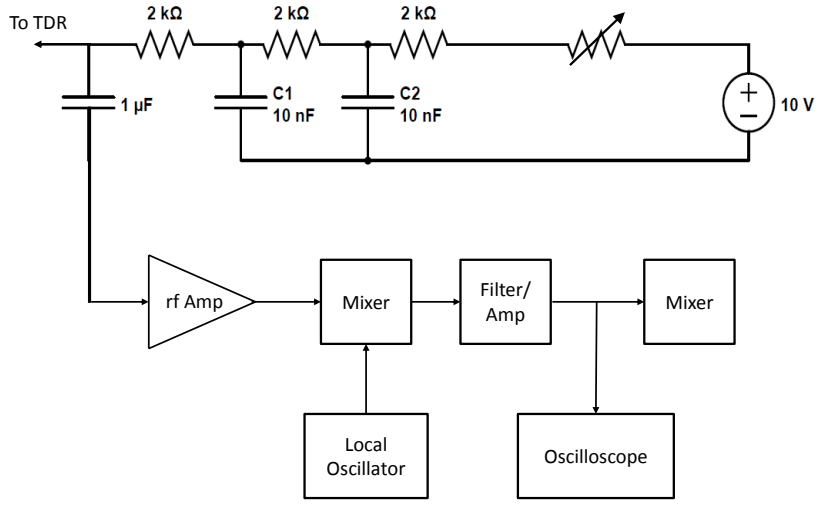

Figure 2.4: Basic external hardware configuration for a TDR setup consisting of common RF components. See text for further details. [Adapted from [1]]

Typical hardware for a TDR setup is shown in Fig. 2.4. A homemade biasing box supplies a bias voltage tunable to the optimal region of the tunnel-diode for the TDR circuit. The 10 nF capacitors and 2 kΩ resistors act as low pass filters shunting frequencies below ≈ 50 MHz. The 1 μF capacitor acts as a high pass filter which shunts the RF signal to an external amplifier. The output data is then mixed with a local oscillator f_{LO} using a non-linear frequency mixer, filtered and amplified, then sent to a counter and oscilloscope. The output of this heterodyned signal is given by $df = f_{LO} \pm f_{TDR}$. Since $\Delta f \propto -\chi$, by setting the local oscillator frequency above the circuit resonance, an increase in susceptibility corresponds to an increase in df. In practice f_{LO} is typically set a few kHz above resonance and the output frequency, measured by a counter, is given by $df = f_{LO} - f_{TDR}$. However, in some cases when frequency shifts are really large (pulsed

fields or large paramagnetic backgrounds) f_{LO} might be set tens of kHz above resonance, and mixing/filtering may be done several times to decrease noise.

2.2.3 TDR in pulsed magnetic fields

Interest in pulsed magnetic fields span a wide range of research areas. Many physical properties can be studied using pulsed fields: specific heat, photo-luminescence, magnetization, resistivity, and GHz and MHz conductivity. Work using TDR in pulsed magnetic fields were conducted in the Agosta Lab at Clark University (up to 45 T), and at the National High Magnetic Field Lab at Los Alamos National Laboratory (NHMFL LANL; up to 65 T) at temperatures ranging from 600 mK to 300 K. The system at Clark University and NHMFL were both designed by Chuck Milke, a former student from the Agosta lab. As such similarities can be seen between the two setups.

The pulsed magnetic fields in this study were created using capacitor bank-driven resistive magnets. The 65 T magnets at NHMFL LANL used a 1.6 mega-joule capacitor bank with a maximum voltage of 9.05 kV, maximum capacitance of 32 mF, max resistance of 40 mΩ, and a 25 ms pulse duration with a 8 ms rise time. Since a large amount of energy is thermally dissipated from the magnet wire, liquid nitrogen was used to cool the magnets. For a 65 T pulse, up to 1.5 hours is required between successive shots to allow the magnet to sufficiently cool. While firing the magnets before maximum cooling is permissible (the temperature of the magnet is monitored by the magnet resistance) inequivalent magnet conditions have a large effect on the background signal and are the dominant contribution to inconsistent background subtractions.

The high fields and tight spaces introduce many technical problems for designing pulsed field cryostats. Inserts were constructed from long ($>$ 1 m long) and thin rods ($\sim$ 2.5 cm outer diameter) of a fiber glass/epoxy composite material known as G-10 because of the materials poor thermal conducting properties. Inserts were placed within a stainless steel "fridge" which was submerged in a liquid helium bath for cooling. The diameter

of the inner magnet bore at both pulsed facilities was 2.5 cm. Since the field greatly affects the electrical properties of the TDR electronics, it was necessary to distance the circuit from the sample and coil in the magnet. The circuit at NHMFL was designed in a RF shielded box which was externally connected to the probe approximately 1 m above the magnet and operated at room temperature. A pickup coil containing the sample was coupled to the TDR primary coil via a transformer. Isolating the circuit at Clark University was achieved by placing the unshielded circuit components inside the fridge further up the G-10 rod, above the magnet, yet still operating at near liquid He temperatures. The difference between in apparatus designs was a trade off. The configuration at Clark allowed the circuit to operate at lower temperatures, without the use of a transformer, resulting in much lower noise compared to the NHMFL configuration. Conversely, the NHMFL's robust design reliably operate throughout both up and down sweep cycles. The difference in circuit stability is apparent when comparing measurements at Clark (Fig. 3.2) and measurements at NHMFL (Fig. 3.4). In both cases, however, given the short duration of the pulse and the large noise associated with the TDR designed for operating in pulsed fields, care was not taken to stabilize the temperature of the circuit.

Due to the large change in magnetic flux inherent to pulsed field experiments, counter-wound coils were employed to limit the induced electromotive force and reduce the magnetoresistive background subtracted from our pulsed field data. The roughly linear background was observed as a ∼90 kHz shift over a field range of 45 T, compared to the ∼100 Hz shift observed for ground state level crossing in $Cr_{12}Cu_2$ and $Cr_{12}Ln_4$. The need for such measures was evident at Clark University where triggering the pulsed field would cause one of the TDR circuits to stop resonating. A pulse magnet with an 8 ms rise time and a maximum field of $H = 45$ T would result in an average $dH/dt = 5625$ T/s. This results in an emf sufficiently large to push the circuit voltage out of the tunnel-diode's optimal negative differential resistance bias region. After reaching the maximum field the change in flux is much smaller, the circuit would return to a suitable bias voltage

allowing proper operation during the down sweep.

Coils were made using extremely delicate 48-50 AWG (25 μm) wire to minimize coil dimensions and maximize filing factor. The painstaking task of winding and mounting the fragile coils under a microscope was an art in itself. For the powder magnetic molecule systems, two 8-turn counter wound solenoids were placed side by side with the sample placed directly in the coils. Upper-critical field measurements of the thin-plate superconducting $SrFe_2(As_{1-x}P_x)_2$ (1 mm x 1 mm x 0.1 mm) single crystals were performed with the sample GE varnished atop a flat counter-wound pancake coil. These coils were mounted to a rotating insert to obtain angular-dependent measurements for the field with respect to the crystallographic axes.

Given the cost, energy requirements, and time between successive shots associated with pulsed field measurements, probes were designed to accommodate multiple samples per pulse field shot, when possible. At Clark, 2 samples were mounted for each shot. At NHMFL, four coaxial lines per probe allowed up to 4 samples to be mounted per cool down measuring two samples per shot. During measurements, each sample was connected to individual hardware for signal mixing, filtering, and amplifying. In addition, data collected using two samples per shot showed good agreement with data collected for individually mounted samples ensuring negligible coupling between coils when multiple samples were mounted.

2.2.3.1 TDR design for dilution refrigerator

Obtaining continuous temperatures below 0.3 K requires a ^{3}He/^{4}He dilution refrigerator (DR), a multi-stage cryogenic refrigerator which takes advantage of the ^{3}He/^{4}He phase separation below 870 mK. Base temperature is achieved through an endothermic process of diluting ^{3}He from a concentrated ^{3}He rich phase to a mixed ^{3}He/^{4}He phase. During circulation a primarily ^{3}He vapor condenses as it passes through a 1K pot. This condensed liquid is further cooled by a dilute ^{3}He mixture exiting the mixing chamber

via a series of silver sintered heat exchangers. In the mixing chamber ^{3}He from a near pure ^{3}He phase transfers through the phase boundary, while absorbing energy, into a dilute (6.6% ^{3}He, 93.4% ^{4}He) phase. The dilute mixture exits the mixing chamber where it warms through exchange as it enters the still. In the still ^{3}He separates from the superfluid ^{4}He, due to a higher partial pressure for ^{3}He. The pressure in the still is kept low ($\sim$ 10 Pa) which regulates circulation by drawing more ^{3}He from the concentrated phase to the dilute phase.

The dilution refrigerator measurements in this work were performed on an Oxford Instruments Kelvinox MX-400 dilution refrigerator. The challenge for designing an apparatus for a DR is limiting the heat load to the mixing chamber. A previously built TDR apparatus, optimized for measuring superconducting transitions T_c for single crystals in zero field (the T-sweep setup), attained a base temperature of $\approx$ 20 mK without applying a bias to the TDR circuit. Once a bias is applied and locks on to resonance the temperature increases by a modest 10 mK. However, this design was optimized for single crystals in zero-fields. This was not suitable for measuring powdered samples which would contaminate the TDR coil, and the emf generated by sweeping magnetic fields resistively heated the circuit causing (causing temperature instability and increased noise) and the sample stage (increasing the base temperature). The T-sweep setup minimized the mixing chamber heat load by mounting the circuit at the still stage where the cooling power is much greater. The sample mounts directly to the mixing chamber and inserts into the coil on a sapphire rod, remaining thermally isolated from the coil and circuit.

The He costs and time commitment for dilution refrigeration measurements is considerable. Several days are required to prepare for each cool down, and 2 hours and 20 minutes is required to sweep up to 14 T at the superconducting magnet's sweep limit 0.1 T/min. This was the motivation behind designing a new sample holder to accommodate up to 4 samples per cool down, allowing multiple TDR circuits to operate simultaneously. When measuring powdered samples it is convenient to pack the sample directly

inside the pickup coil. The issue with this design is that the sample and coil must sit at the same temperature (with a desired base temperature < 100 mK), while the circuit operates at a much warmer temperature (~ 2.6 K). Therefore, it is necessary to establish a strong thermal break between the coil and circuit to minimize the sample's base temperature and reduce the heat load to the mixing chamber. Further, measurements of the empty coil background for the first design attempt resulted in the observation of a reproducible background which appeared to be quantum oscillations arising from the copper coil. This was a surprising result at our temperature of approximately 100 mK and the onset at a low field of only 8 T.

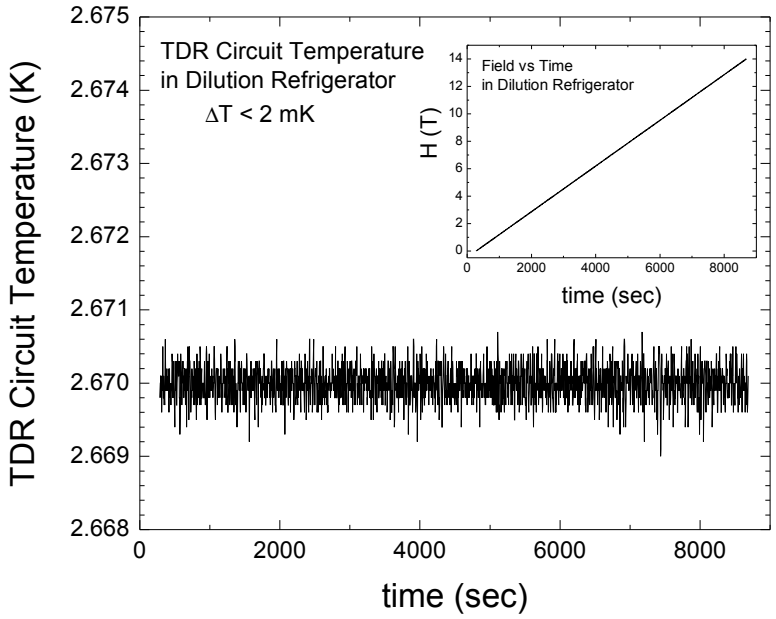

Figure 2.5: Plot demonstrating the temperature stability of the TDR set up for H-sweep in a dilution refrigerator. Four circuits were mounted on a copper plate using a 50 Ω resistor as a heater.

To resolve the thermal heating, 4 circuits were designed in several stages with most of the components mounted to circuit boards bolted to a copper plate fixed to the bottom of the mixing chamber using a stainless steal rod which resulted in a weak thermal break.

This allowed a heater and thermometer mounted to the copper plate to allow an accurate temperature control of the circuit components. The circuit temperature was set tens of millikelvin above the the 1 K pot temperature with a temperature fluctuation less than 2 mK (demonstrated in Fig. 2.5). Temperatures were controlled using a Lakeshore Cernox CX-1030-SD thermometer and 50 Ω heater. The tank capacitor was mounted to the bottom of the mixing chamber via high resistance wire as a thermal break, and well out of the center of the field to minimize magnetoresistance and heating from eddy currents while sweeping the magnetic field. The tank capacitor was connected to the primary coil using a rigid copper coax. This configuration allowed a thermal break from the tunnel-diode and resistive components, while ensuring a good thermal link to the mixing chamber.

Resolving the quantum oscillation issues required using a different coil material with no magnetic contribution and minimum resistivity. To this end we used phosphor-bronze wire, commonly used as a low temperature thermometry lead. The resistivity of phosphor-bronze at dilution refrigerator temperatures is approximately 90 nΩ·m, compared to approximately 10 nΩ·m for copper. By reducing the values of the circuit components, a lower power diode could be used, and hence lower bias voltage/current reducing the heat load for the resonating current: $R1 = 220\ \Omega$, $R2 = 150\ \Omega$, $R3 = 22\ \Omega$, $C_C = 39$ pF, $C_B = 12$ nF, and $C_T = 100$ pF.

The result was a low noise system with an operating base temperature of 100 mK and an order of magnitude reduction in the field-dependent background.

2.3 Nuclear Magnetic Resonance

Nuclear magnetic resonance has long been realized as a powerful probe for studying physical static and dynamic properties [20, 21]. NMR enables one to characterize the local electronic and magnetic properties by manipulating the quantum mechanical

properties of a local atomic nucleus with an rf field. This technique is exploited in the physical sciences to study novel materials, in chemistry to characterize molecular structures, in biochemistry to determine 3-dimensional molecular structures, and as an *in vivo* imaging technique in medicine. The general principles of NMR will be discussed in the next section

Resonance occurs when an oscillator is tuned to some natural frequency, for example, the energy difference between two magnetic energy levels in atomic spectra in an external magnetic field. This energy difference typically falls in the radio frequency (RF) range for nuclear spins and microwave frequency (GHz) for electron spins. This resonance process for nuclear spin moments is the foundation for NMR.

2.3.1 General resonance theory

A great deal of information is encrypted in the internal fields at the atomic nuclei arising from hyperfine interactions with local electron spins. To unlock this information one can observe changes in the field and temperature dependent static and dynamic properties of the nuclear spins. If one considers the total spin angular moment $\mathbf{I}$ of a nucleus, a nuclear magnetic dipole moment $\boldsymbol{\mu}$ will be given as

$$\boldsymbol{\mu} = \gamma\hbar\mathbf{I}, \tag{2.15}$$

where γ is the gyromagnetic ratio of the nucleus and $\hbar$ is Planck's constant divided by 2π. The energy of $\boldsymbol{\mu}$ in an external magnetic field H_0 is given by

$$\mathcal{H} = -\boldsymbol{\mu} \cdot \mathbf{H_0}. \tag{2.16}$$

The magnetic spin moment will posses $2I + 1$ eigenstates denoted as $|m_z\rangle$, where m_z are the eigenvalues of I_z for a field H_0 applied along the z direction. Rewriting Eqn. (2.16) in terms of these eigenstates we get the Hamiltonian

$$\mathcal{H} = -\gamma\hbar H_0 I_z. \tag{2.17}$$

The external field will Zeeman split these eigenstates with resulting energies

$$E = -\gamma\hbar H_0 m_z \quad m_z = I, I-1, ..., -I. \tag{2.18}$$

Magnetic dipole transitions are permitted between states with $\Delta m = \pm 1$. The energy gap between allowed transitions can be expressed as

$$\Delta E = \gamma\hbar H_0 = \hbar\omega_n, \tag{2.19}$$

which yields the Larmor frequency for a nuclear spin moment in a magnetic field as

$$\omega_n = \gamma_n H_0. \tag{2.20}$$

2.3.2 Moments in alternating magnetic fields

The behavior of a magnetic spin moment in a constant external field is described by the Larmor theorem. The time-dependent behavior obeys the classical equation of motion in a magnetic field,

$$\frac{d\boldsymbol{\mu}}{dt} = \boldsymbol{\mu} \times (\gamma_n \mathbf{H_0}). \tag{2.21}$$

From this equation the nuclear magnetic moment will precess around the external magnetic field. The expectation value of the z-component will remain constant while the x- and y-components will oscillate sinusoidally with at the Larmor frequency.

If we introduce a linearly oscillating, transverse magnetic field $\mathbf{H_1(t)} = H_1(\mathbf{i}\cos\omega_z t + \mathbf{j}\sin\omega_z t)$ then the equation of motion can be described as

$$\frac{d\boldsymbol{\mu}}{dt} = \gamma_n \boldsymbol{\mu} \times [\mathbf{H_0} + \mathbf{H_1}(t)]. \tag{2.22}$$

It is convenient to express Eqn. (2.22) in terms of a rotational reference frame with the rotational axes x' and y' rotating with a constant angular velocity ω about $z' \parallel \mathbf{H_0}$. If we take H_1 to lie along the x'-axis then the time-dependent equation of motion in the rotating reference frame is expressed as

$$\frac{\delta\boldsymbol{\mu}}{\delta t} = \boldsymbol{\mu} \times [(\gamma_n H_0 + \omega)\hat{\mathbf{z}}' + \gamma_n H_1 \hat{\mathbf{x}}'], \tag{2.23}$$

with the time derivative given by $\frac{\delta \boldsymbol{\mu}}{\delta t} = \frac{d\boldsymbol{\mu}}{dt} + \boldsymbol{\mu} \times \omega$. The term in the square brackets of Eqn. (2.23) represents an effective field $\mathbf{H_{eff}} = (H_0 + \omega/\gamma_n)\hat{\mathbf{z}}' + H_1\hat{\mathbf{x}}'$.

When $\omega = -\gamma_n H_0$ (the Larmor frequency) the system is said to be in resonance. The effective field is simply given by H_1 and μ precesses about x' with a rate $\omega_1 = -\gamma_n H_1$. By controlling the length and duration of H_1 we can manipulate the rotation of μ in to the yz-plane by some angle θ. We can create a "90° pulse" by applying H_1 for a duration τ such that the angle of rotation is $\theta = \pi/2 = \gamma_n H_1 \tau$. If the nuclear spin moment is oriented along z' at time $t = 0$, then after such a pulse μ would be oriented along the y'-axis. After the pulse this system would then precess in the xy-plane. Similarly, one can achieve a "180° pulse" rotating the nuclear spin moment aligned along z' towards $-z'$ by applying H_1 for a duration of 2τ.

2.3.3 Nuclear relaxation

The total magnetization $\mathbf{M}$ for a system of N non-interacting spins in a volume V can be expressed as a summation of individual moments, $\mathbf{M} = V^{-1} \sum \boldsymbol{\mu_i}$, where the sum is taken over all N moments. Therefore, the evolution of the nuclear magnetization could be expressed in a manner similar to Eqn. (2.23). Expressing the magnetization M_i ($i = x, y, z$ components) yields the phenomenological Bloch equations:

$$\frac{dM_x}{\delta t} = \gamma_n(M_y H_z - M_z H_y) - \frac{M_x}{T_2}, \tag{2.24}$$

$$\frac{dM_y}{\delta t} = \gamma_n(M_z H_x - M_x H_z) - \frac{M_y}{T_2}, \tag{2.25}$$

$$\frac{dM_z}{\delta t} = \gamma_n(M_x H_y - M_y H_x) - \frac{M_x - M_0}{T_1}. \tag{2.26}$$

For the Bloch equations, H_z is given by the longitudinal static field H_0, $H_{x,y}$ is given by the oscillating transverse field H_1, and M_0 represents the equilibrium magnetization along H_0. The values T_1 and T_2 are characteristic NMR relaxation recovery times. Relaxation time T_1 corresponds to the relaxation of the longitudinal magnetization to

the equilibrium value M_0. T_1 is commonly known as the spin-lattice relaxation time as it measures the duration over which nuclear spins exchange energy with the lattice and return to equilibrium. Often this value is referenced as $1/T_1$, known as the spin-lattice relaxation rate. Relaxation time T_2, also known as the spin-spin relaxation time, is characteristic to the time required for the transverse magnetization component M_{xy} to dephase due to spin-spin interactions and field inhomogeneity. During spin-lattice relaxation processes energy is not conserved, while for spin-spin relaxation energy is conserved.

2.3.4 Spin-lattice relaxation

Spin-lattice relaxation is the mechanism in which the longitudinal magnetization relaxes from a perturbed orientation to equilibrium. The process requires energy dissipation from the perturbed spin into the lattice (e.g. phonons, conduction electrons). The source of this relaxation arises from fluctuations of the local magnetic field from interactions between the nucleus and the local environment.

This process is governed by the probability that a spin will transition between adjacent energy levels. If we consider a simple two state system where N_m is the number of spins in state m and N_n is the number of spins in state n. Nuclear spins states in m will have lower energies (ground state), while spins in n will be excited states. The probability per unit time for inducing a transition are given by W_{nm} for transitions from the excited state to ground state and W_{mn} for transitions from ground state to excited states. The change of population could then be written in terms of a linear differential rate equation

$$\frac{dN_m}{dt} = (N_n W_{nm} - N_m W_{mn}). \tag{2.27}$$

This so called "master equation" characterizes population differences following an RF pulse. The longitudinal magnetization is proportional to the population for each level,

$$M_z(t) = \gamma_N \hbar \sum \langle m|I_z|n\rangle N_-(t), \tag{2.28}$$

where $N_- = N_m - N_n$ is the population difference. The task of solving the nuclear spin-lattice relaxation rate is therefore reduced to solving the relaxation rate W_{mn}.

The equilibrium populations for a two state system (spin 1/2) are given by

$$\frac{N_n^0}{N_m^0} = e^{-\gamma_n \hbar H_0/kT}, \tag{2.29}$$

where $\gamma\hbar\ H_0$ represents the energy difference between the two states. Using the expression for the rate equation and the fact that $dN_m/dt = 0$ in the steady-state to obtain an expression for the transition probabilities,

$$\frac{W_{nm}}{W_{mn}} = \frac{N_n^0}{N_m^0} = e^{-\gamma\hbar H_0/kT}. \tag{2.30}$$

In the high temperature limit, where $\gamma\hbar H_0 \ll k_B T$, we obtain an expression for the spin-lattice relaxation rate

$$\frac{1}{T_1} = \frac{1}{2}\frac{\sum_{m,n} W_{mn}(E_m - E_n)^2}{\sum_n E_n^2}. \tag{2.31}$$

This limit assumes the partition function becomes the total number of states. That is $Z = Z_{T=\infty} = (2I+1)^N$. This approximation is legitmate in most cases since only a small number of partake in relaxation, and this treatment for $1/T_1$ remains valid unless the energy of a small number of spins is proportional to $k_B T$.

To calculate the relaxation probabilities it is convenient to use first-order time-dependent perturbation theory, assuming the rf excitation $\mathcal{H}_1(t)$ is very weak compared to the Zeeman Hamiltonian ($\mathcal{H}_1(t) \ll \mathcal{H}_0$). This is called the weak collision limit. The relaxation rate W_{mn} is given by the so called Fermi's golden rule,

$$W_{mn} = \frac{2\pi}{\hbar}|\langle m|\mathcal{H}_1|n\rangle|^2 \delta(E_m - E_n - \hbar\omega). \tag{2.32}$$

Eqn. (2.32) applies only when the exact energy values of the lattice are known, or at low temperatures when energy levels can be approximated.

This approach effectively treats the nuclear spins with a common spin-temperature T_s and the lattice as a heat reservoir with T_L. Following a perturbation, the $T_s > T_L$. In

equilibrium $T_s = T_L$. By treating the spins by a spin-temperature we indirectly account for spin-spin couplings.

For the case $I = 1/2$,

$$\frac{1}{T_1} = W_{1/2,-1/2} + W_{-1/2,1/2} = 2W, \tag{2.33}$$

where $W_{nm} \cong W_{mn} \equiv W$ since $|\langle m|\mathcal{H}_1|n\rangle|^2 \approx |\langle n|\mathcal{H}_1|m\rangle|^2$ in Eqn. (2.32). For $I > 1/2$, additional terms for the relaxation must be considered to account for the distribution between energy levels.

2.3.5 Detection methods

A majority of NMR measurements are conducted using a pulsed NMR setup to detect the NMR signal. This method, which can also be referred to as Fourier transform NMR, uses an RF pulse to excite the nuclear magnetization. The equilibrium magnetization $M_z = M_0$ can be rotated from the z-axis into the transverse plane by applying an RF pulse of frequency ω_n for a duration τ such that $\gamma H_1 \tau = \pi/2$. Following this $\pi/2$ pulse, the magnetization in the rotating frame will start to dephase due to inhomogeneities in field at the local nuclei. The field inhomogeneity can arise from the applied field and/or distributions of the local hyperfine fields. For this reason, high homogeneity magnets and shimming of the magnetic field are used to increase uniformity of the field.

Following rotation into the transverse plane the magnetization will precess in the laboratory frame inducing a voltage in the pickup coil. As a result of field inhomogeneity, the distribution of the local field will cause the precessing magnetic moments to fan out; some spins will precess faster than the average ω_n, while some precess slower. This process will be observed as a voltage response with the resulting signal envelope called a free induction decay (FID). The characteristic decay time of this response is given by T_2^*. It should be emphasized that T_2^* is related to the dephasing magnetization in the transverse plane arising from all sources of inhomogeneity. This is in contrast to T_2 arising from the

irreversible decay of the transverse magnetization arising from characteristic properties of a sample ($1/T_2^* \sim 1/T_2 + \Delta H$).

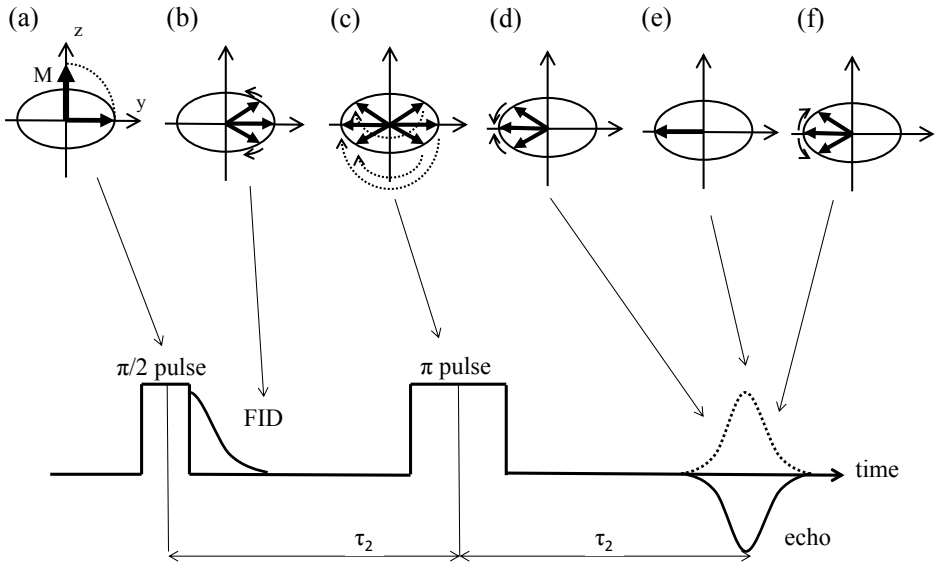

Figure 2.6: (a) $\pi/2$ pulse rotates magnetization into transverse plane. (b) Dephasing of magnetization arising from field inhomogeneities at spin sites. (c) π pulse rotates spins about the x-axis mirroring previous spin configuration. Spin echo forms: (d) refocusing spins, (e) maximum rephasing occurs, (f) spins dephase again.

To minimize the effects of field inhomogeneity, a spin-echo technique is often used in NMR experiments. This technique is sometimes called a Hahn echo after Erwin Hahn explained the phenomenon [30]. The process is depicted in Fig. 2.6 ignoring the effects of longitudinal relaxation. Fig. 2.6 (a) shows the magnetization initially in equilibrium aligned with the external field. Fig. 2.6 (b) shows the magnetization in the transverse plane following a 90^o ($\pi/2$) pulse. The dephasing of the signal, with faster and slower spins respectively leading and lagging the average spin procession, results in the FID. Fig. 2.6 (c) shows the effect of a 180^o (π) pulse where all components of the magnetization are rotated about the x axis. The time between the $\pi/2$ pulse and π pulse is defined as

τ_2. After the π pulse, slower spins will now lead the average spin moment while faster spins will trail. Fig. 2.6 (d-f) Shows the refocusing of the spin moments creating what is called an echo. The echo will occur at a time approximately $t = \tau_2$ after the π pulse, and $t = 2\tau_2$ after the initial $\pi/2$ pulse. Note that the spin echo is inverted with respect to the FID.

Measurements of the spin-lattice relaxation require an additional time component to monitor the recovery of M_z. This process begins with $\pi/2$ pulse to initially rotate the magnetization in to the xy plane such that $M_z = 0$. This step is often called saturation with the pulse referred to as a saturation pulse. At time $t = \tau$ after the saturation pulse, the Hahn echo sequence is then used to detect the signal intensity. Varying τ results in a time dependent spin echo intensity where the recovery of M_z for the simple case $I = 1/2$ follows as

$$M_z(t) = M_0[1 - exp(-\tau/T1)], \tag{2.34}$$

with T_1 given by Eqn. (6.6).

CHAPTER 3. PULSED FIELD STUDIES OF $Cr_{12}Cu_2$

3.1 Introduction

From an experimental perspective $Cr_{12}Cu_2$ offered an interesting and complex system to validate quantum Monte Carlo (QMC) calculations using an isotropic Heisenberg Hamiltonian. Specifically, this is a low-symmetry heterometallic system featuring two different spin values, where characterizing this system required three different exchange values (2 antiferromagnetic and 1 ferromagnetic) exhibiting a spin triplet ground state. Studying this system experimentally was of particular interest as the system was expected to demonstrate a rich field dependent spectra with a saturation field of 80.7 T, within available experimental pulsed field limits. Furthermore, the use of TDR in pulsed fields was particularly intriguing as the frequency dependence of pulsed fields allowed us to observe excited state level crossing which are unobservable in traditional pulsed field methods, such as DC magnetometers.

Previous studies of the magnetic molecule $Cr_{12}Cu_2$ by the Prozorov group used TDR to compare the low-energy spectrum with theoretical simulations conducted by Profs. Luban and Engelhardt [31, 32]. The $Cr_{12}Cu_2$ molecule, see Fig. 3.1, is an hourglass structure with five-coordinate Cu^{2+} ($S_{Cu} = 1/2$, $g_{Cu} = 2.1$) ions bridging the ends of two Cr_6 "horseshoes" of Cr^{3+} ($S_{Cr} = 3/2$, $g_{Cr} = 1.98$) with metallic ions lying in plane. The full chemical structure for $Cr_{12}Cu_2$ is $[N(C_2H_5)(C_3H_8)_2]_2[Cr_{12}Cu_2F_{16}(O_2CCMe_3)_{26}]$. The Cr and Cu ions are bridged by fluoride and carboxylate ligands. Each Cu ion has one Cr-Cu site with a single carboxylate ligand, while all other Cr-Cr and Cu-Cr sites feature

two carboxylate ligands yielding inversion symmetry. We will find that this leads to two distinct exchange pathways for each Cu ion: Cr-Cu and Cu-Cr. This results in 180^o spherical symmetry with magnetically equivalent sites on opposite sides of the molecule.

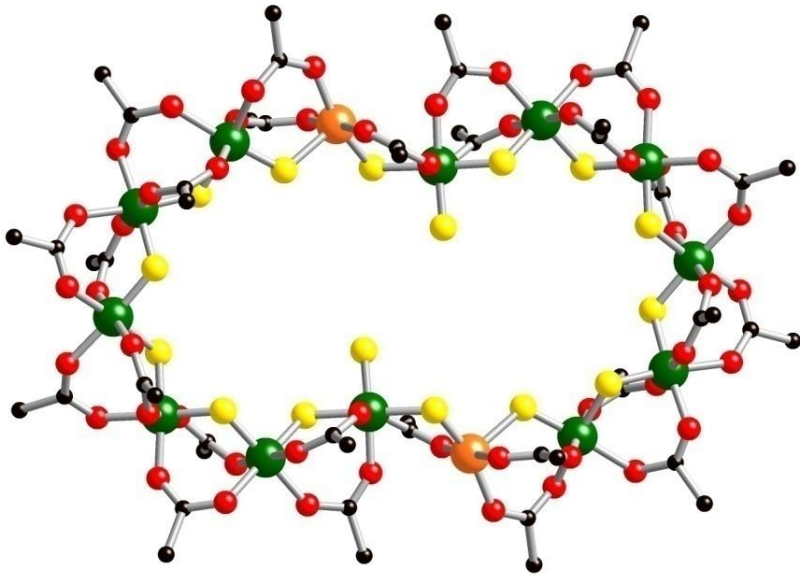

Figure 3.1: Molecular structure of hourglass shaped $Cr_{12}Cu_2$ structure with metallic ions lying in plane. Colors: Cr, green; Cu, orange; O, red; F, yellow; C, black.

Generally, at high temperatures ($T > J/k_B$) ions in magnetic molecules behave as uncorrelated spins whose behavior follows Eqn. (1.8). At low temperatures ions evolve into a correlated collective spin system, one can obtain field and temperature dependent information with regard to spin dynamics for an exactly solvable finite system. The magnetic properties for AFM rings can be well treated using the spin Hamiltonian

$$\mathcal{H} = -2J \sum_{i=1}^{N} \boldsymbol{S}_i \cdot \boldsymbol{S}_{i+1} + D \sum_{i=1}^{N} S_{i,z}^2 + g\mu_B \boldsymbol{H} \cdot \sum_{i=1}^{N} \boldsymbol{S}_i. \tag{3.1}$$

The first term corresponds to the isotropic Heisenberg Hamiltonian for neighboring spins S_i and S_{i+1} with exchange coupling constant J which can be antiferromagnetic ($J < 0$) or ferromagnetic ($J > 0$). The second term represents uniaxial single-ion anisotropy

along the easy z-axis ($D < 0$) for N number of ions. The last term is the field-dependent Zeeman interaction.

The $Cr_{12}Cu_2$ system was treated as a 1-dimensional chain with magnetic properties well characterized using the isotropic Heisenberg Hamiltonian in Eqn. (3.1), without the anisotropic term ($D = 0$). Since the total spin operators S^2 and S_z both commute with the Hamiltonian, the eigenstates of the spin operators are described by the quantum numbers S and m_s with values ranging from 0 to 19 (12 x 3/2 + 2 x 1/2) and from $-S$ to S, respectively. The enormous size of the Hilbert space of dimensionality $(2S+1)^N$, for N particles of spin S, leads to direct diagonalization to be impractical. To overcome this theoretical hurdle a number of classical and quantum methods are employed [17, 18, 33–35]. It was determined from QMC calculations that three exchange constants were necessary for a good fit of the low-field DC magnetic susceptibility $\chi(T) = M(H,T)/H$. The exchange constant $J_1/k_B = -7.8$ K describes the Cr-Cr interactions, while the exchange constants $J_2/k_B = -28.6$ K and $J_3/k_B = 10.4$ K describe the two distinct Cr-Cu and Cu-Cr pathways.

QMC was used to calculate the low-temperature differential susceptibility, dM/dH, as a function of external magnetic fields. In zero field the ground state is in a total spin $S = 1$ state. Zeeman splitting of the energy levels results in a field-dependent ground-state with transitions occurring between $S_{i-1} \rightarrow S_i$. The level-crossing fields were determined by QMC with a saturation field of 80.7 T. The field values for the level crossings in Tesla are: 8.15, 11.9, 16.2, 19.8, 24.1, 27.6, 31.7, 35.15, 39.3, 42.6, 47.1, 50.1, 55.2, 57.65, 64.3, 65.5, and 80.7. Each peak corresponds to an approximately 2 μ_B step in the magnetization. Calculating the zero-field energy values from these values is straight forward. By denoting zero-field energy of a lower-energy multiplet as E_S, the energy gap between successive multiplets is given by $E_{S+1} - E_S = g\mu_B H_S$. It is of no consequence to shift the ground state energy level to $E_{S=1} = 0$, and therefore the one can determine the entire zero field energy spectrum.

TDR measurements were conducted in the Prozorov Group's dilution refrigerator by sweeping magnetic field, limited up to 14 T, to experimentally determine dM/dH. Two peaks are observed at lowest temperatures (80 mK - 500 mK) corresponding to steps in the magnetization as the system transitions from an $S = 1 \rightarrow S = 2$ ground state at 8.1 T, and from an $S = 2 \rightarrow S = 3$ ground state at 11.9 T. These experimentally determined field values for the level crossings are in excellent agreement with the first two fields determined by QMC. Upon increasing temperature, additional peaks become progressively visible with a rich spectrum at 2.5 K. These states arise as the increased thermal energy allows for the population of excited spin states within an energy range k_BT of the ground state. In Fig. 4 of [31], peaks for excited transitions are shown to be in good qualitative agreement with theoretically predicted field values.

The excellent agreement observed for theoretical QMC calculations and TDO dM/dH measurements validate the treatment of $Cr_{12}Cu_2$ as strictly isotropic Heisenberg system with negligible intermolecular magnetic interactions, and the use of TDR as a low-temperature probe of quantum spin systems at low energies (fields). The pulsed field facilities of Clark University and the National High Magnetic Field Lab at Los Alamos National Laboratory (NHMFL LANL) offered the opportunity to validate higher field level-crossings. Further, the 100 T system at NHMFL offered an experimental setup to confirm the predicted values up to saturation of the magnetic spin moments.

3.2 Results and discussions

For pulsed field measurements, samples were packed directly in to the counter-wound pickup coils. Measurements at Clark used coils lined with Teflon tape so the same coil could be used for multiple measurements without contamination, while at NHMFL a new coil was wound for each sample. In both cases the powder samples were mixed with small quantities ($\sim$ 10% by mass) of diamagentic Apiezon N Grease to ensure uniform

cooling of the poor thermal conducting powder samples.

Fig. 3.2 and Fig. 3.4 show the pulsed field TDR data, after background subtraction, collected during the downs sweep at Clark University ($T = 570$ mK and $T = 2.5$ K; up to $H = 45$ T) and NHMFL ($T = 600$ mK; up to $H = 65$ T), respectively. The background was subtracted using a background curve determined using a fifth-order polynomial fit to the approximately linear background regions between level crossing peaks, where the background regions were determined from the first-derivative of the experimental data. The difference between resolution is obvious upon initial inspection for reasons discussed in chapter 2. At $T \approx 600$ mK, both figures clearly observe several peaks which tend to form in pairs (doublets). Applied fields lift the $(2S + 1)$-fold degeneracy of the zero-field energy levels such that crossings between energy levels occur. This is due to a $g\mu_B m_s H$ shift originating from the Zeeman term. Therefore, these peaks correspond to changes in dM/dH as a result of transitions between H-dependent ground state level-crossings. Specifically, observed transitions correspond to changes between quantum states by increasing the total spin quantum number S by one unit. For example $(S, m_S) => (1, -1) \rightarrow (2, -2)$, or more generally $(S, m_s = -S) \rightarrow (S + 1, m_s = -|S + 1|)$. For higher fields, the separation between two peaks forming a doublet decreases, becoming hard to distinguish two peaks in the case of NHMFL data. Fig. 3.3 shows the field dependence of the Zeeman splitting for the eleven lowest $(S, m_S = -S)$ energy levels.

The 2.5 K data from Clark shows a rich spectrum of peaks corresponding to excited state level crossings. In order to observe these peaks there must be a sufficiently large thermal energy to thermally populate excited states, i.e. $k_B T > \Delta$, where Δ is the energy gap between the ground state and excited state. These features are not observable in static DC SQUID measurements and require measurements of the dynamic susceptibility using, for example, TDR. Many of these transitions are of $\Delta S = 2$, in violation of the selection rules. In order to reconcile this one must add a weak anisotropic contri-

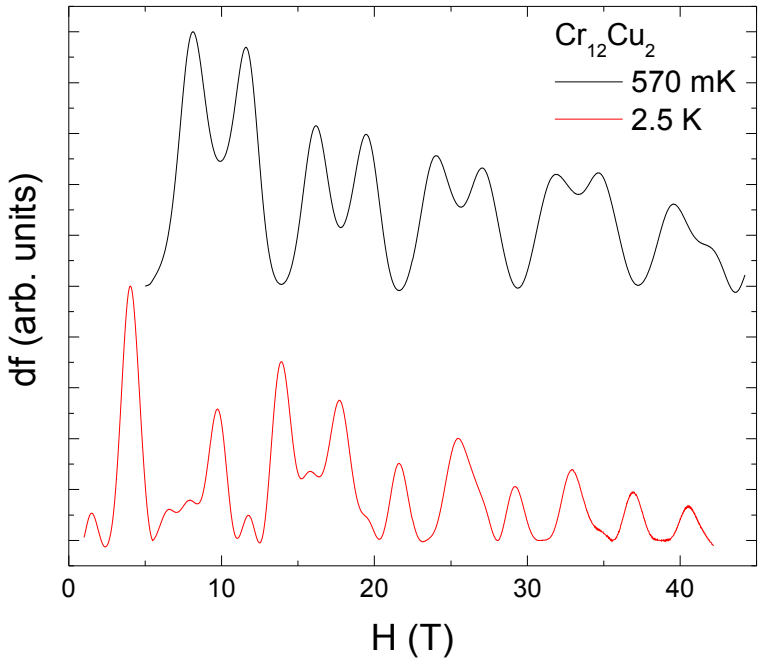

Figure 3.2: Pulsed field TDR measurements from the down sweep in fields up to 45 T. The black curve (top curve) corresponds to measurements at $T = 570$ mK. Peaks indicate transitions between ground state level crossings between $S_{i-1} \rightarrow S_i$. The red curve (lower curve) was measured at 2.5 K. The rich spectrum of peaks arises from transitions involving excited states where the thermal energy sufficiently populates excited energy levels.

bution from non-Heisenberg terms to the Hamiltonian to allow such transitions. These anisotropic contributions give rise to a small energy gap δ (i.e. avoided level crossings) when two levels would otherwise cross. The frequency of the TDR must satisfy the inequality $2\pi\hbar f_0 > \delta$, putting an upper limit of ≈ 0.8 mK on the size of these energy gaps for TDR frequency $f_0 \approx 15$ MHz.

The peaks in Fig. 3.4 were fit with Gaussian curves using the "Multi-peak Fitting" program included in Igor Pro 6.22 graphical analysis software. This software uses a Savitzky-Golay smoothing filter to perform a polynomial regression fit for the data. Fig. 3.5 compares the field values of the level-crossing peak positions vs transition i for

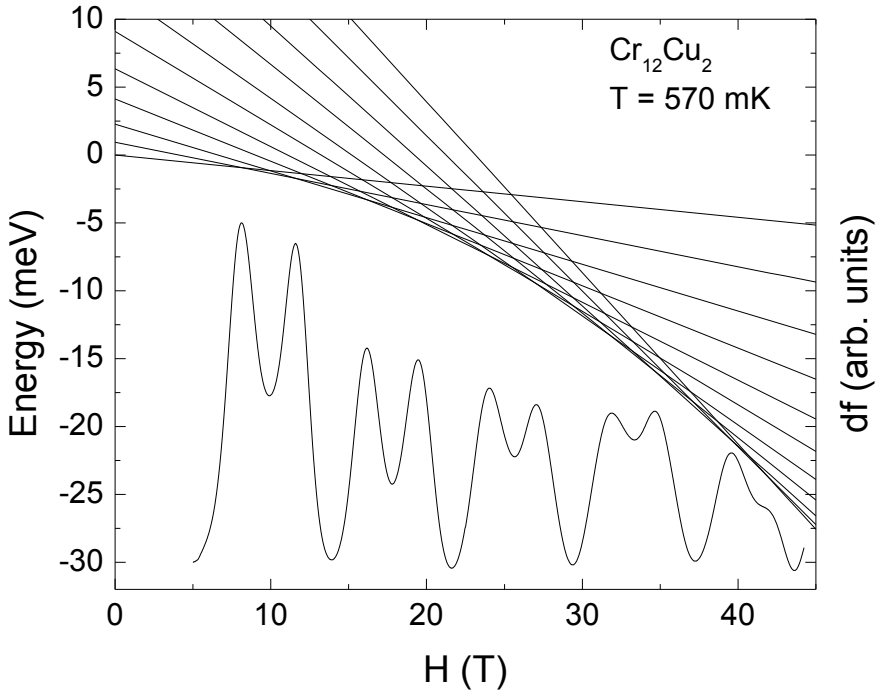

Figure 3.3: Zeeman split energy level diagram including $(S, -m_s)$ levels, corresponding to the left axis where the zero-field ground state equals zero. Crossing of energy levels correspond to ground state level crossings. The 45 T pulsed field data from Clark is included to emphasize agreement, corresponding to the right axis.

the 65 T NHMFL data (black circles) and the theoretically calculated values from QMC (red crosses), where i corresponds to transitions from total spin state $S_{i-1} \rightarrow S_i$. The agreement was remarkably good, typically within 1 T. It is noted that the fitting method was unable to distinguish a doublet peak near 48 T, corresponding so $i = 12$ and 13, and thus a single peak is reported in Fig. 3.3 for $i = 12$. Level crossing field data from Clark was not plotted for clarity, however, it should be noted that peaks through $i = 11$ were typically within 0.5 T agreement with the calculated values.

The dM/dH data from Clark was fit using a similar process as described above to further understand TDR as a spectroscopic tool in pulsed fields. Fig. 3.6 shows the results of this analysis. The first observed parameter is the field separation between

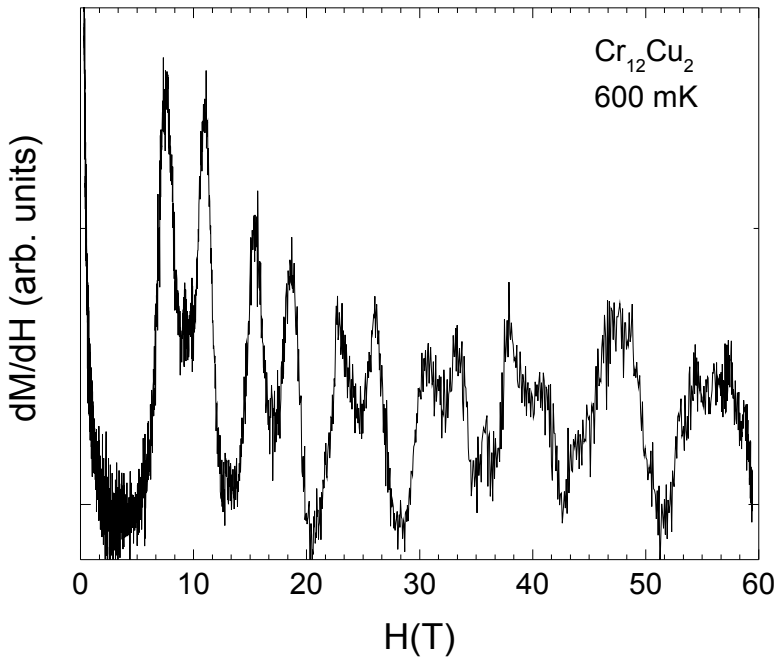

Figure 3.4: Pulsed field TDR spectrum from the down sweep of a 65 T pulse measured at NHMFL LANL. The noise, compared to the pulse field data from Clark, is due to a different TDR setup. The increase in noise is a trade off for a more robust circuit designed for operating in the presence of high electromotive forces.

successive peaks, ΔH, in units of Tesla. Next parameter is the peaks full width at half amplitude (FWHA), in units of Tesla. Last, the area of each peak plotted in arbitrary units.

While the linear behavior for the level crossing field vs transition i is linear, the peak to peak separation is more complicated. The systems stays in a total spin $S = 1$ ground state in applied fields $0 \leq H \leq 8.23$ T (0.48 meV). The field required for this first transition between $S = 1 \rightarrow S = 2$ is much larger than for subsequent transitions, by approximately 1.6 times. After this first transition the peak separation alternates between 3 T (0.17 meV) and 5 T (0.29 meV) arising from the doublet structure. What is interesting is that although the peak to peak separation within each doublet decreases

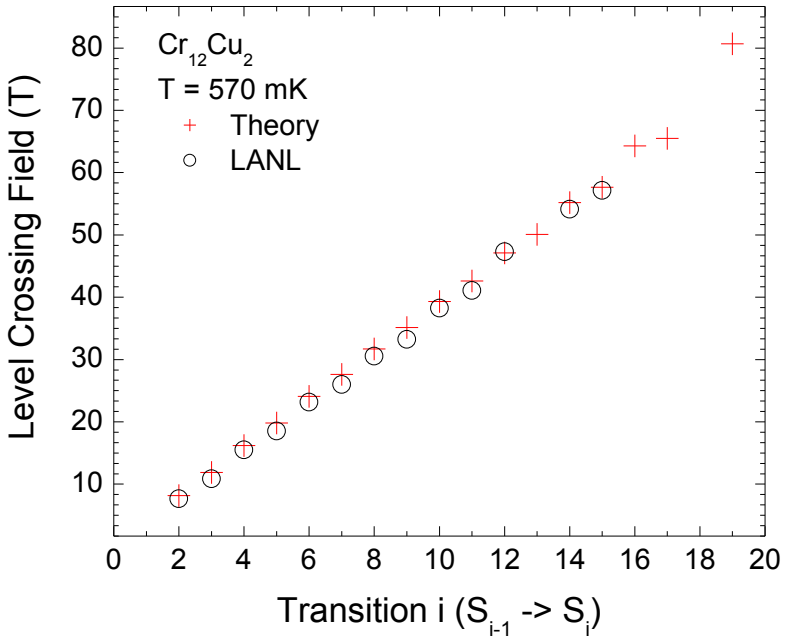

Figure 3.5: Plot demonstrates the agreement between theoretically predict level crossings and level crossings determined pulsed magnetic field measurements at LANL. Fitting of the peaks were unable to identify two peaks for $S = 12, 13$. Level crossings for measurements from Clark were also in good agreement but excluded for clarity.

for higher S_i (from 3.27 T between $S = 2 \rightarrow S = 3$ to 2.24 T between $S = 10 \rightarrow S = 11$) the separation from doublet to doublet remains almost constant (4.7 T to 4.9 T) when measured as the separation from the second peak of a doublet to the first peak of the next successive doublet.

The theoretically calculated peak to peak separations show the same behavior, alternating between 3 T and 4.3 T in the same range. The peak to peak separation for the last three calculated transitions are 6.7 T, 1.2 T, then a large separation to 15.2 T at saturation (where S goes from $17 \rightarrow 19$). Therefore large energy gaps exist before the first excited state and before reaching saturation, with alternating sized potential barriers in between. This suggests even values for the total spin state are energetically less favorable then odd values. A similar behavior is observed for $Cr_{10}Cu_2$ with an $S = 0$

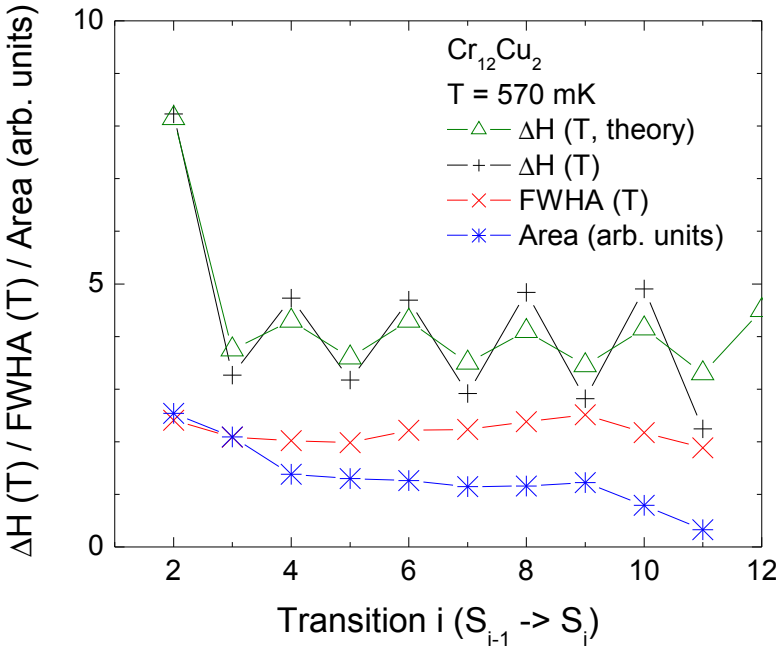

Figure 3.6: Plot of the peak area, FWHA (T), and field separation between peaks ΔH (T) for the first 10 ground state level crossings determined from the 45 T Clark pulsed field data.

ground state, however, only a small gap is observed for $S = 0 \rightarrow S = 1$ and even values for the total spin state are more stable with a larger separation between $S = 2 \rightarrow S = 3$ [31].

In addition to the peak to peak separation the FWHA and area were also analyzed. Somewhat unexpectedly the FWHA remained constant while the area decreased upon transitioning to higher spin ground states. The peak area is calculated with dimension $frequency \times Tesla$ and reported in arbitrary units. Since shifts in frequency for TDR are proportional to dM/dH, the total area under the peak should represent the change in magnetization which should be a constant 2 μ_B/step. However, the decreasing peak area indicates a non-linear response as a function of field.

Other possible origins for the non-linear response could include the process for sub-

tracting background, and the time-dependent shape of the pulse field. The background subtraction process is straightforward at high fields where the only contribution to the background arises from a near-linear magneto-resistive term. This region can be well fit by a fifth order polynomial leaving only the peaks in dM/dH. Subtracting from lower fields is more tricky where the background is non-linear. This could give rise to over or underestimating the peak amplitude. However, for this explanation to make sense I would expect the peak area to be almost constant for higher fields which is not the case. The non-linear response could then be a consequence of the pulse shape where the field sweeps faster at high fields than low fields as expected for the decay of an LC circuit. This could possibly explain the peak area and constant FWHA, but it would require spin transitions to take place on time scales slower than the field sweep rate, which is orders of milliseconds.

3.3 Conclusions

This study represents the first use of TDR in pulsed magnetic fields for detecting quantum spin transitions in magnetic molecules. Further, $Cr_{12}Cu_2$ offered a system to test the legitimacy of QMC calculations using a purely isotropic Hamiltonian. This fact may be surprising given a small anisotropy is necessary for observing excited state level crossings. While the ambitious intention for this work was to validate the theory up to saturation in a field $H = 80.7$ T on the 100 T magnet at NHMFL, time and magnet availability restrictions limited us to the first 15 of 17 predicted peaks. Treating $Cr_{12}Cu_2$ with three exchange constants accurately predicts a triplet ground state. The most significant result of this study is the remarkable agreement between theoretically calculated and experimentally determined field values for the ground state (and excited state) level crossings using TDR in pulsed fields. From these measurements it is clear that TDR is a powerful tool for observing the dynamic magnetic susceptibility of magnetic

molecules in pulsed fields.

CHAPTER 4. STUDIES OF MOLECULAR MAGNET $Cr_{12}Ln_4$

4.1 Introduction

The extension of adding $4f$ orbital Lanthenide (Ln = Y, Eu, Gd, Tb, Dy, Ho, Er, and Tb in this study) elements was an obvious progression for magnetic molecules, where most magnetic molecules previously focused on $3d$ orbital metals (M = V, Cr, Mn, Fe, Ni, Cu) [36]. For a physicist the interest lies in the magnetic nature of inner shell valence f orbitals and the nature of the $3d$-$4f$ interactions. The majority of Ln^{3+} ions have orbitally degenerate ground states split by spin-orbit coupling and crystal field effects. Since spin-orbit coupling is much larger for $4f$ electrons compared to $3d$ electrons, and crystal field effects much smaller, therefore orbital angular momentum is more important for determining magnetic behavior in rare earth ions than transition metals. This is a result of the the partially filled $4f$ shells lying inside the $5s$ and $5p$ shells. Further, this internal electronic shell structure is expected to give rise to weak magnetic interactions between Ln-Ln and Ln-Cr ions.

The total angular momentum, total electron spin, and orbital angular momentum for rare earths Y^{3+} ($J = S = L = 0$) and ground state for Eu^{3+} ($J = 0$ and $S = L$) results in a diamagnetic ground state. Gd provides an interesting comparison with $3d$ systems as the orbital angular momentum is quenched, $L = 0$, and the total angular momentum is given by the total electron spin, $J = S$. For the remaining rare earth systems J, L, and S are non-zero. The values of J, L, and S are given using the traditional ground state

Table 4.1: J, L, S, and g_J Values for Select Triply Ionized Rare Earths

Element	Ground State	g_J
Gd	$^8S_{7/2}$	2
Tb	$^7F_6$	3/2
Dy	$^6H_{15/2}$	4/3
Ho	$^5I_8$	5/4
Er	$^4I_{15/2}$	6/5
Yb	$^2F_{7/2}$	8/7

notation, $^{(2S+1)}L_J$, in Table 4.1. In this notation $L = S, P, D, F, G, H$, and I correspond to orbital angular momentum values of $L = 0, 1, 2, 3, 4, 5$, and 6, respectively [37, 38]. A critical consequence of compounds with orbitally degenerate $4f$ ions, $L \neq 0$, is they can not be treated with simple isotropic spin Hamiltonians as used for transition metal compounds due to anisotropy arising from the orbital angular momentum.

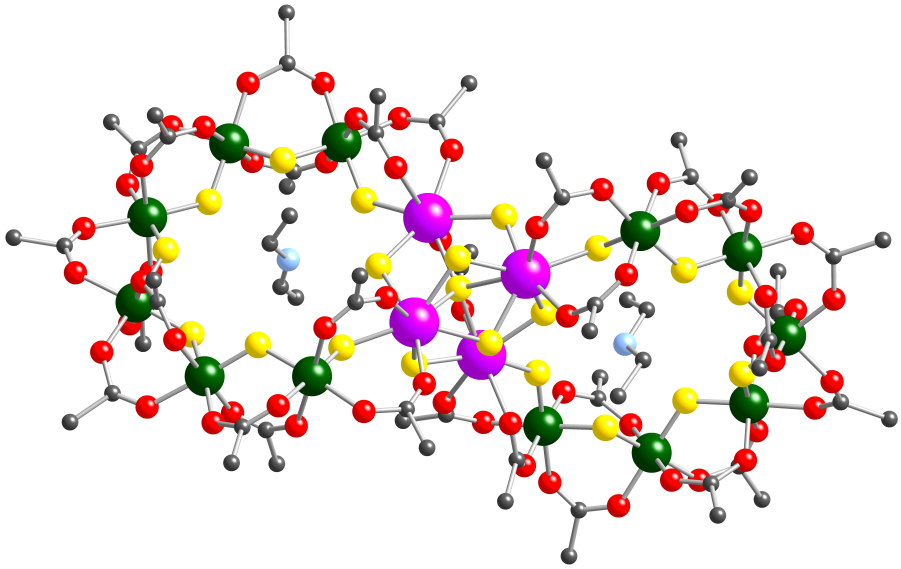

Figure 4.1: (Color online) Structure for $Cr_{12}Ln_4$. Tetrahedral structure for Ln ions leads to 98.4^o between planes of the two Cr horseshoes. Colors: Cr, green; Ln, purple; O, red; F, yellow; N, blue, C, black.

The possibility of binding RE ions to Cr_6 structures presented an open question chemically. Given the monovalency and high electronegativity for fluorides bridging

Cr-Cr sites, it was uncertain whether the fluorides bind with sufficient strength to allow Ln ions to bind to ligands at Cr sites, rather than forming LnF_3 salts [39]. Assembly of the $Cr_{12}Ln_4$ structure begins with a pair of Cr_6 horseshoes, $\{Cr_6\}_2$, whose general formula is $[(Et_2NH_2)_3\{Cr_6F_{11}(O_2C^tBu)_{10})\}]_2$, with three terminal fluoride ligands at the end of each terminal chromium site. The general formula for $Cr_{12}Ln_4$ is $[(Et_2NH_2)_2\{Cr_{12}Ln_4F_{21}(O_2C^tBu)_{29}\}]$ with the corresponding structure shown in Fig. 4.1. The molecule consists of two $\{Cr_6\}$ horseshoes connected by a distorted tetrahedron of Ln ions with each Ln ion bridging a different terminus of the Cr horseshoe. This results in a near orthogonal 98.4^o between mean planes of the two $\{Cr_6\}$ horseshoes yielding a non-crystallographic 2-fold C_{2v} symmetry. In both structures the Cr-Cr, and Cr-Ln sites for $Cr_{12}Ln_4$, are bridged by a single fluoride and two pivalate groups. This structure allows for magnetic exchange between Cr-Cr sites, Cr-Ln sites, and Ln-Ln sites [39]. Initial efforts to grow $Cr_{12}Ln_4$ compounds with light rare earths (La, Ce, Pr, Nd, Pm, and Sm) were unsuccessful with the only synthesized structure being a heptametallic ring of six Cr ions and one Ce ion [40]. Sample synthesis and magnetization measurements were conducted by the Winpenny group in the Department of Chemistry, University of Manchester. All measurements were on powder samples and pulsed field measurements were conducted with the sample placed directly inside the coil.

Magnetic properties of rare earths are well known to be dominated by the inner shell $4f$ orbitals. Spin-orbit coupling of the trivalent ions splits the ^{2S+1}L multiplets in to J states of energy

$$E(^{2S+1}L_J) = (\lambda/2)[J(J+1) - L(L+1) - S(S+1)], \tag{4.1}$$

with $J = |L-S|$ for light rare earths and $J = L+S$ for the rare earths in this study (Gd - Yb). λ gives the strength of the spin-orbit coupling in units of energy. The g factor of a given J multiplet is given by (see Table 4.1)

$$g_J = \frac{3}{2} + \frac{S(S+1) - L(L+1)}{J(J+1)}. \tag{4.2}$$

Generally, the lowest lying J multiplet lies well below excited states. The values calculated for χT in Table 4.2 are given by the usual form

$$\chi T = \frac{N_A(g_J\mu_B)^2}{3k_B} J(J+1), \tag{4.3}$$

where J is the total angular momentum. Deviations from Curie's law for coupled rare earth and transition metal ions can arise from the single-ion effect of the rare earth ion or Curie-Weiss behavior.

4.2 DC magnetization

Fig. 4.2 (a) shows the DC magnetic susceptibility χ taken in an external field of $H = 0.1$ T for the family $Cr_{12}Ln_4$ (Ln = Y, Eu, Gd, Tb, Dy, Ho, Er, and Tb). For convenience samples will be identified by the corresponding rare earth ion (i.e. the "Gd sample") and "$\{Cr_6\}_2$" corresponding to two Ln-free horseshoes. The inset shows a near identical behavior above approximately 100 K corresponding to all magnetic ions in the paramagnetic region. Below 100 K systems with samples containing magnetic rare earths show an increase in χ as T goes to zero, exhibiting Curie-like behavior. For $\{Cr_6\}_2$, Y, and Eu samples, χ approaches zero as T goes to zero offering definitive proof of antiferromagnetic interactions between Cr-Cr ions as observed in previous Cr chains and rings [31, 41, 42].

A plot of χT is shown in Fig. 4.2 (b). The value of χT as T goes to zero, is proportional to the ground state for the total angular momentum, as seen in Eqn. (4.3). Since $\chi T \to 0$ as T goes to zero for $\{Cr_6\}_2$, Y, and Eu provides direct evidence of a $S = 0$ spin singlet ground state. While systems containing magnetic Ln ions sharply decrease for χT below 50 K, it is not possible to determine the ground state from this data (for closer inspection, a plot of χT below 20 K is provided in Fig. 4.4 (b) after subtracting the χT contribution for $Cr_{12}Y_4$). Above 100 K, χT for Eu (and possibly Tb) continues to increase, rather than saturate. For Eu, this is readily observed upon comparison with χT plots for $\{Cr_6\}_2$ and

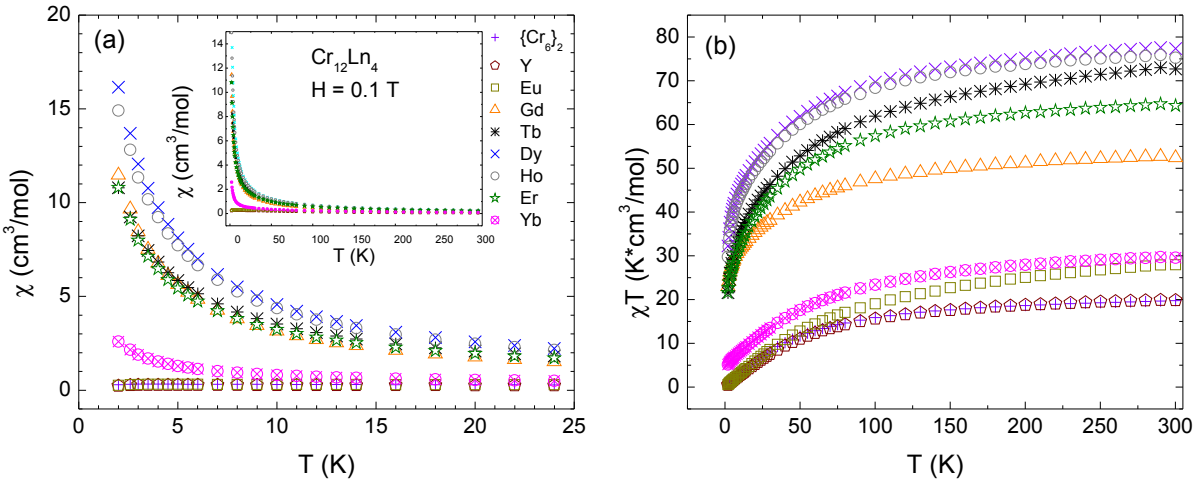

Figure 4.2: (Color online) (a) DC magnetic susceptibility χ at $H = 0.1$ T. Systems exhibiting upward Curie-Weiss behavior at low temperature correspond to systems with magnetic Ln ions. The three curves trending towards zero correspond to systems with non-magnetic Ln ions. The inset shows the DC susceptibility over the entire temperature range. (b) Plot of χT versus temperature. The values of $\chi T(T = 0)$ is directly proportional to the total spin ground state.

$Cr_{12}Yb_4$. This behavior likely arises from a low lying J-multiplet just above the ground state such that excitations into higher J levels can be appreciable at room temperature. I make a special note that the earliest publication I could find regarding such behavior for Eu^{3+} was reported by Frank Spedding in 1940, while working at what was then named Iowa State College [43].

Fig. 4.3 shows magnetization as a function of field at a constant temperature $T = 2$ K. The $\{Cr_6\}_2$, Y, and Eu samples show only a small linear increase as the external field increases while the magnetic Ln systems show an abrupt Brillouin-like increase in magnetization for $H \neq 0$.

The near identical behavior in Fig. 4.2 and Fig. 4.3 for $\{Cr_6\}_2$ and the diamagnetic Y sample suggest very similar magnetic behavior arising from the Cr ions upon assembly

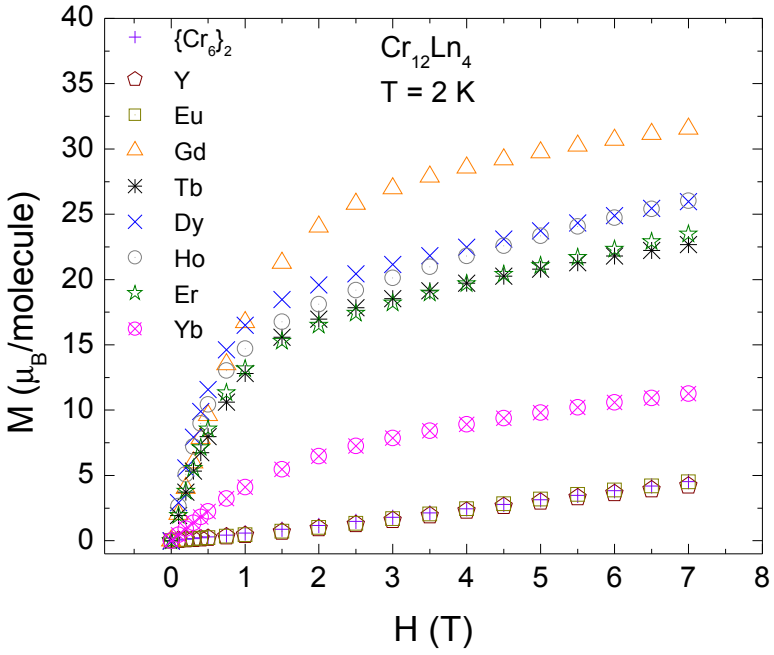

Figure 4.3: (Color online) $M(H)$ measurements conducted in DC SQUID at $T = 2$ K.

into the $Cr_{12}Ln_4$ structure. Further, the plots of χ, χT, and $M(H)$ indicate the Ln ions behave as nearly paramagnetic, weakly-interacting systems. Therefore, in order to further understand the behavior of the $\{Ln_4\}$ tetrahedra contributions for $Cr_{12}Y_4$ were subtracted from χ, χT, and $M(H)$ for systems with magnetic Ln ions. These reduced values are identified with an asterisk (e.g. χ^* in Fig. 4.4). $Cr_{12}Y_4$ with non-magnetic Y^{3+} ion was choosen over the Eu sample to avoid issues arising from excited J-orbitals at high temperatures. Further, the similar structures of the assembled the $Cr_{12}Y_4$ system and the remaining $Cr_{12}Ln_4$ systems was the primary motivation behind using data for the Y system rather than the $\{Cr_6\}_2$ horseshoes. However, it is noted that the difference between the $\{Cr_6\}_2$ data and Y data is quite small: $\Delta\chi T(300\text{ K}) = 0.3\text{ K}\cdot\text{cm}^3/\text{mol}$ and $\Delta M(7\text{ T}) = 0.3\ \mu_B/\text{molecule}$. By making this approximation it is assumed the exchange constants between Cr-Ln ions are very weak, as expected for interactions involving $4f$

ions [36, 44–49].

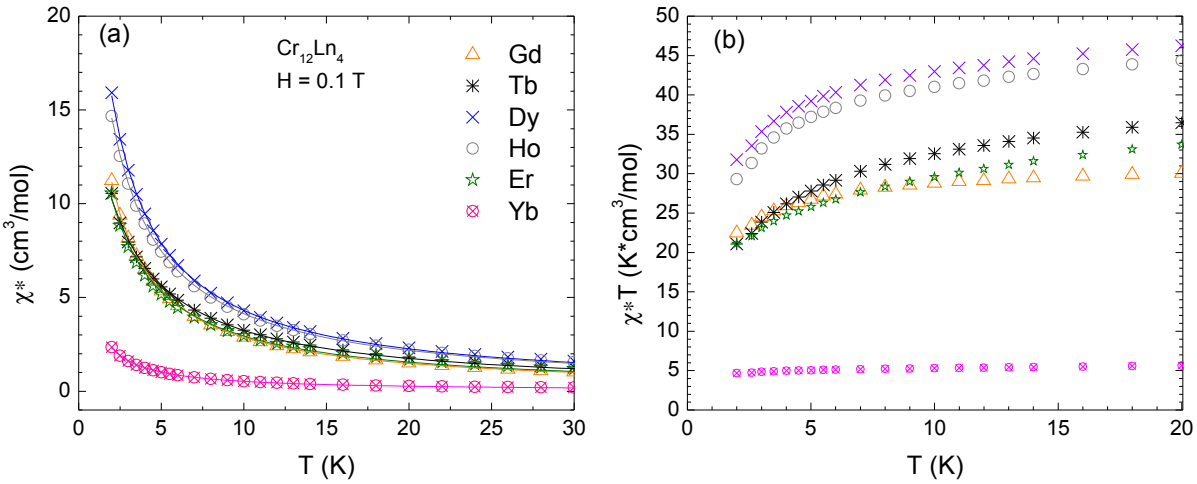

Figure 4.4: (Color online) a) Plot of χ^* for systems with magnetic Ln ions after subtracting the contribution from $Cr_{12}Y_4$. It is presumed this contribution arises from the four weakly interacting $4f$ Ln ions. The solid lines correspond to Curie-Weiss fits for $T <$ 100 K as described in the text. b) Low temperature plot of χ^*T versus temperature.

Fig. 4.4 (a) shows the reduced magnetic susceptibility χ^* for the six magnetic Ln systems below 30 K. The data were analyzed using a Curie-Weiss fit, Eqn. (1.10), in the temperature range 2 K $< T <$ 100 K. The results of these fits are included in Table 4.2. The values observed for Curie constant C_{exp} are only slightly lower than the theoretical values for corresponding non-interacting ions (see χT_{calc} in Table 4.2). The experimentally determined Weiss temperatures Θ_{exp} are also reported. All systems exhibit a negative Weiss temperature suggesting a very weak AFM interaction associated with Ln-Cr interactions, ranging from $\Theta = -0.37$ K to -1.71 K for the Yb and Tb samples, respectively. This is in contrast to other complexes containing lanthenide and transition metal ions, where the Ln-TM exchange interactions are either ferromagnetic or too weak to determine [36, 44–49].

Table 4.2: Curie Weiss Data

Element	$\mathbf{C_{calc}}$ **(cm^3·K/mol)**	$\mathbf{C_{exp}}$ **(cm^3·K/mol/Ln)**	$\mathbf{\Theta_{exp}(K)}$	$\mathbf{\chi^*T(300\ K)}$ **(cm^3·K/mol/Ln)**
Gd	7.88	7.74	-0.78	8.15
Tb	11.82	9.50	-1.71	13.22
Dy	14.17	11.88	-1.02	14.38
Ho	14.07	11.53	-1.17	13.85
Er	11.48	8.25	-1.23	11.12
Yb	2.57	1.37	-0.37	2.43

Calculated Curie values for triply ionized Ln ions. Experimental values determined from a Curie-Weiss fit of χ^* or χT^*(300 K) after subtracting the magnetic susceptibility contribution from $Cr_{12}Ln_4$.

Fig. 4.4 (b) plots the reduced susceptibility as χ^*T in the low temperature region. At sufficiently high temperatures a plot of χT will become constant arising from the paramagnetic behavior, $\chi T = C$, where C is Curie's constant. All of the systems are near saturation at room temperature with the values of χ^*T(300 K) for the magnetic Ln ions listed in Table 4.2. The values are all in good agreement with the calculated values for χT. It is also interesting to note here that the Gd sample, with $L = 0$, approaches saturation much more rapidly, reaching 90% of saturation by 16 K, compared to approximately 65 K for Dy and Ho, 75 K for Er, and 160 K for Yb.

Further analysis of the low temperature region of χ^*T in Fig. 4.4 makes determining the ground state for the magnetic Ln ions difficult. Again, the $\{Cr_6\}_2$, Y, and Eu showed a clear trend towards zero at low temperatures. Most of the Ln systems show the onset of a sharp downward trend towards zero below 5 K. However, the Yb sample, with the smallest Weiss temperature of Θ = -0.37 K, observes almost no decrease at low temperatures. Extrapolating this curve to $T = 0$ K, results in χT^* =4.5 cm^3·K/mol/Ln, approximately half the calculated value of 10.28 cm^3·K/mol/Ln. To accurately determine the spin value of the ground state, a lower temperature DC measurement is required. However, these results suggest that a high spin ground state is plausible.

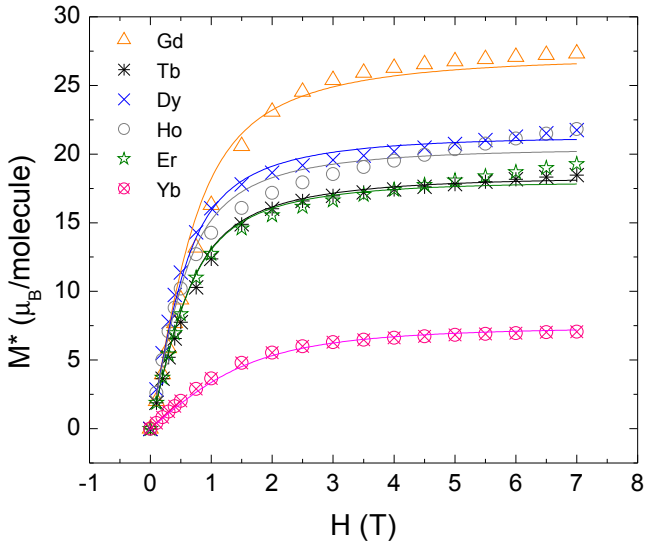

Figure 4.5: (Color online) $M(H)$ for systems with magnetic Ln ions after subtracting the contribution from $Cr_{12}Y_4$. The remaining contribution arises from paramagnetic Ln ions. The lines correspond to fits using a Brillouin function as described in the text.

The reduced magnetization is plotted in Fig. 4.5 after subtracting $M(H)$ for $Cr_{12}Y_4$. The solid line in the data corresponds to a fit using the Brillouin function as expressed in Eqn. (1.6) and Eqn. (1.7). The magnetic contribution in this reduced scheme arises entirely from the four Ln ions. Therefore, the saturation value for the magnetization as a function of field should be proportional to the g-factor multiplied by the total angular momentum as $g_J J$. The theoretically calculated values and values as determine for $M^*(H = 7\text{ T})$ can be found in Table 4.3. Upon inspection, it is peculiar that the Gd sample would show the largest saturation despite the second lowest expected moment. Analysis for $M^*(H = 7\text{ T})$ demonstrates good agreement for the Gd sample ($g_J J|_{exp} = 6.8$ compared to a calculated value $g_J J|_{cal} = 7$) where the orbital angular momentum is quenched, $L = 0$. For the remaining samples with $L \neq 0$ (Tb, Dy, Ho, Er, and Yb), the experimentally determined values of $g_J J$ from the magnetization at $T = 2$ K and $H = 7$ T are approximately 1/2 of the theoretically expected values

Table 4.3: $M(H)$ Data

Element	$\mathbf{g_J J}$ **(calculated)**	$\mathbf{g_J J}$**(7 T) (experiment)**
Gd	7	6.8
Tb	9	4.6
Dy	10	5.4
Ho	10	5.5
Er	9	4.8
Yb	4	1.8

Values of $g_J J$ calculated for triply ionized Ln ions and determined from M(H = 7 T) after subtracting contribution from $Cr_{12}Ln_4$.

determined by Hund's rules. This would correspond to a rotation of the total angular momentum by $\approx 60^o$ away from the applied field axis, independent of the magnitude of L. This suggests that a non-zero orbital angular momentum gives rise to large anisotropy arising crystal field or single ion effects. Similar Ising-like anisotropic behavior has been observed for intermetallic systems featuring Ln ions exhibiting AFM ordering between moment-bearing members [12–14]. For the Gd sample, on the other hand, the Gd ions act as model Heisenberg moments.

To summarize the DC magnetization data, plots of the low-field susceptibility and T-dependent magnetization demonstrate very similar behavior for the systems with no magnetic Ln ions present, with a $S = 0$ ground state. Magnetic properties for systems with magnetic Ln ions can be treated as a superpostion of properties from the Ln_4 tetrahedra and the $\{Cr_6\}_2$ horseshoes. The T-dependent susceptibility demonstrates good agreement between experimental values for χT and the calculated Curie values from four paramagnetic ions at high temperatures. At low temperatures, contributions from the Ln_4 ions demonstrate a Curie-Weiss behavior with a weak AFM interaction determined by the Weiss temperature. The magnetization data at 2 K shows a linear increase in M(H) for the non-magnetic systems in fields up to 7 T. On the other hand,

systems with magnetic Ln ions saturation exhibiting a Brillouin like behavior. While the magnitude for the orbitally quenched Gd sample agrees with the calculated values for four non-interacting triply-ionized Gd ions as determined by Hund's rules, the systems with orbital angular moment $L \neq 0$ saturate at 1/2 the expected value. This suggests the orbital contributions introduce a considerable anisotropy which reduces the z-component of the total angular momentum in an applied field at low temperatures, likely arising from crystal field effects or single-ion effects.

4.3 Dynamic susceptibility in pulsed fields

Pulsed field measurements were conducted in Chuck Agosta's pulsed magnetic field lab at Clark University following the same procedure as discussed for $Cr_{12}Cu_2$. Two different circuits measured simultaneously for each pulse with resonance frequencies f_1 = 24.39 MHz and f_2 = 29.62 MHz for circuits 1 and 2, respectively. Samples measured in circuit 1 include Dy, Ho, $\{Cr_6\}_2$, and Gd; samples measured in circuit 2 include Tb, Yb, Y, and Eu. Note that an Er sample was not available for pulsed field measurements. Fig. 4.6 shows dM/dH for the $Cr_{12}Ln_4$ family, at T = 600 mK and in fields up to 45 T, after subtracting the background for the empty coils.

The initial field dependence below $\approx$ 2 T likely arises from the paramagnetic contributions of the Ln ions. As such the $\{Cr_6\}_2$, Y, and Eu samples show almost no dM/dH-dependence at low fields, while the samples containing magnetic Ln ions show a decrease in dM/dH roughly proportional to the total angular momentum of the respective Ln ion. A precise analysis of this region was avoided since the task of precisely measuring the amount of sample successfully placed within the coil would have been extremely time intensive, and therefore impractical given the limited available pulse time. Above 2 T, peaks are observed in the susceptibility corresponding to level crossings between the H-dependent energy levels. At these fields, the paramagnetic Ln ions are

saturated and $dM/dH = 0$ is expected between level crossing peaks. The approximately linear H-dependent background observed for the $\{Cr_6\}_2$, Dy, and Ho samples likely arise due to a poor empty coil measurement for circuit 1.

In the inset of Fig. 4.6 below 1.5 T, the Tb sample (and possibly Dy) shows a large doublet peak in dM/dH near $H = 0.6$ T in the paramagnetic region, almost 2.5 times larger than the next largest peak. The feature is not reflected in the DC magnetization, however, the temperature for that measurement is much higher. While the origin of this peak is not clear at this time it is possible this corresponds to a step in the magnetization arising from Tb-Tb, or more likely Tb-Cr interactions noting that, from Table 4.2, the Tb sample shows a much larger Weiss temperature than the other Ln samples. A temperature of 600 mK might be a sufficiently low thermal energy to observe exchange coupling between Tb-Tb or Tb-Cr, but high enough that the remaining Ln systems behave as paramagnetic ions.

A plot of dM/dH for the pulse field data after subtracting the paramagnetic background is shown in Fig. 4.7 at temperatures of 600 mK and 2.5 K. Subtracting the background contribution for fields below 1 T can be difficult due to the large paramagnetic contributions and low-field dependence to magneto-resistance of coil and field dependence of resonator capacitance. In Fig. 4.7 (a) above 1 T, $\{Cr_6\}_2$ features six well defined peaks corresponding to ground state level crossings with $\Delta S = 1$, and a small bump near 5 T likely arising from an excited level crossing. The position of these peaks are, in Tesla: 2.9, 7.8, 15.6, 23.3, 30.3, 36.0, 38.0. The remaining systems observe only five peaks with some showing the onset of a sixth peak at the upper pulse limit. The presence of the non-magnetic Y and Eu Ln ions increases the field value for each level crossing, which becomes more dramatic at higher fields. For example, the peak position of the first peak and fifth peak for the Y and Eu samples are at 3.5 T and 36.0 T, compared to 2.9 T and 30.3 T $\{Cr_6\}_2$, respectively. The addition of a magnetic Ln ion indiscriminately pushes these level crossing fields slightly higher, with the first peak near

4 T, independent of Ln. This suggests that changing the rare earth ions can not be used to systematically manipulate the zero field energies in these magnetic molecule systems. This is likely a result of the exchange interactions for Cr-Ln sites are much weaker than the Cr-Cr sites. Fig. 4.7 (b) demonstrates the high resolution for which TDR can detect a rich spectrum of ground state and excited state level crossings in pulsed fields. Note the positions of many excited state level crossings are located directly in between ground state level crossings. These excited state level crossings arise from transitions with $\Delta S = 2$.

Fig. 4.8 shows the thermal evolution for the Y and Gd samples measured using a 14 T superconducting magnet with a slow sweep rate of 0.1 T/min. Below 700 mK, the Y sample features two peaks in dM/dH at $H = 3.5$ T and 9.6 T, while the Gd sample shows two doublet peaks shifted to slightly higher fields . The Gd peaks appear at slightly higher fields with the first doublet at $H = 4.4$ T and 5.6 T, and the second doublet at 10.1 T and 11.3 T. The doublet peak for the Gd sample are seen in both DC fields and pulsed fields for both ground and excited level crossings. In the pulsed field data, separation between peaks within a doublet decrease for level crossings at higher fields until only one peak is detected, similar to the behavior observed for $Cr_{10}Cu_2$ and $Cr_{12}Cu_2$ [31, 42]. Unfortunately there is no clear explanation for why this doublet feature is observed for only the $L = 0$ Gd sample.

4.4 Theoretical fits

Numerical calculations were performed in order to determine the Cr-Cr exchange coupling constants for $\{Cr_6\}_2$, as done in $Cr_{12}Cu_2$ using QMC. Simulations were conducted using a program called FIT-MART ("Fully Integrated Tool for Magnetic Analysis in Research & Teaching"), developed by Larry Engelhardt at Francis Marion University, which simulates relevant physical parameters (χ, $M(H)$, etc.) by direct numerical diagonaliza-

tion of spin matrix (dimension = $(2S+1)^N = 4096$) using a Heisenberg Hamiltonian. For small systems, these calculations are simple enough that they can be performed on a typical desktop computer. While $\{Cr_6\}_2$ is a rather simple system (calculations took several seconds to complete), a Cr_8 ring system will begin to push the limits/patience of the typical computer/user.

A minimum of two exchange constants were necessary to reproduce the peak at 5 K and shoulder near 20 K in the DC susceptibility, as show in Fig. 4.9. The best fit was obtained with J_1 = -8.55 K for the three inner Cr-Cr exchange paths and J_2 = -6.65 K corresponding to exchange paths at the two edge cites (see lower left inset in Fig. 4.9 (a)), for $S_{Cr} = 3/2, g_{Cr} = 1.98$. It should be noted that adding an additional exchange parameter to couple the two edge sites, even with small values, drastically led to poor agreement with the experimental susceptibility It is also important to note that reasonable fits are still obtainable when J_1 and J_2 differ by as much as $\pm 0.2K$. Systematically changing values for $J1$ and $J2$ it was quickly observed that increasing exchange values suppressed and broadened the susceptibility, while pushing the peak to higher temperatures. Using a $-2J\mathbf{s_n}\cdot\mathbf{s_{n+1}}$ Heisenberg representation, AFM rings typical exhibit a peak in the susceptibility in the area of J'.

The energy diagram calculated for the 4096 spin states is plotted in Fig. 4.10 showing a discrete spectrum for the lowest lying energy levels. There is a small energy gap (4 K, 0.345 meV) separating the total spin $S = 0$ grounds state from the $S = 1$ first excited state. The lowest lying energy levels for each spin states, commonly referred to as the L-band, follows Landé's interval rule where $E_S \propto S(S+1)$ represented by the solid black line. It can be seen from this energy level diagram that at low temperature the system will characterized by a discrete spectrum of energy levels with spins occupying only a few quantum states. At intermediate temperatures the number of occupied states will be best represented as a continuous spectrum of energy states and can be theoretically treated by classical approximations. This property of magnetic molecules offers a system

to experimentally study the transition from classical to quantum statistics.

Fig. 4.11 compares dM/dH for the pulsed field data and the FITMART simulations. Using the values noted above, a poor fit was obtain for dM/dH despite the quality agreement achieved for the DC susceptibility. The first calculated peak at H = 3.0 T is in good agreement with the experimental data with a peak position at H = 2.92 T, suggesting that the peak observed below 1 T results from poor background and low field effects from the circuit. For higher field peaks, the agreement between the experimentally observed peaks and simulations becomes gradually poorer. As mentioned above, a range of values for J_1 and J_2 resulted in good fits for χ, however, varying these values resulted in near identical plots for dM/dH. It should also be noted that attempts to fit dM/dH by varying J_1 and J_2 independent of the DC susceptibility could not produce a quality fit. Also, attempts to fit the $Cr_{12}Gd_4$ data with QMC were unsuccessful, and therefore will not be discussed here.

Attempts to fit the $Cr_{12}Y_4$ data on the other hand led to good agreement for both χ and dM/dH. Fig. 4.12 (a) shows the low temperature DC susceptibility and a FITMART simulation with three exchange parameters (the full temperature region is shown in the upper right inset). The antiferromagnetic exchange parameters J_1 = -8.5 K, J_2 = -8.85 K, and J_3 = -7.9 K corresponding to the exchange paths depicted in the lower left inset. The fit was achieved by treating each Cr_6 horseshoe independently and fitting to the susceptibility for the Y sample divided by two. This effectively reduced the system to a single Cr_6 horseshoe. A plot of the experimental and simulated dM/dH is shown in Fig. 4.12 (b), resulting in a much better agreement than observed for the plain Cr_6 horse shoe. For this fit, J_1 remain approximately the same, while the parameters J_2 and J_3 are larger than the values used for the corresponding exchange pathways in Cr_6. This suggests that the addition of the Ln ions "tightens" the outer Cr_6 exchange paths giving rise to the shifts towards higher fields in dM/dH.

4.5 Conclusions

DC susceptibility measurements indicate AFM ordering for Cr ions in the $\{Cr_6\}_2$ horseshoes with an $S = 0$ ground state. The addition of non magnetic Ln ions Y and Eu offer a negligible affect on the DC susceptibility and magnetization measurements. Systems containing magnetic Ln ions (Gd, Tb, Dy, Ho, Er, Yb), on the other hand, show a large contribution from these large $4f$ moments which behave like non-correlated paramagnetic ions. Curie-Weiss fits for the low temperature susceptibility suggest the onset of weak antiferromagnetic interactions at low temperatures. This result is surprising as many interactions featuring Gd and transition metals are ferromagnetic as a result of a charge transfer mechanism. Unfortunately DC measurements were limited to a base temperature of 2 K and a determination of the ground state was not possible. However, the χT data did leave open the possibility of a high spin ground state despite the apparent AFM interaction.

Plots of $M(H)$ at 7 T demonstrate a magnetic moment equivalent to half that expected for non-interacting triply-ionized Ln ions when the orbital angular momentum is not quenched, $L \neq 0$, however, the orbitally quenched $L = 0$ Gd sample shows good agreement with theoretical calculations for four paramagnetic Gd moments in field. This suggests the large anisotropy arising from the orbital angular momentum dramatically reduces the magnitude of the local moment at the Ln ions. This fact in itself is not surprising as the orbital anisotropy is well known to cause a canting of the Ln moments. What is surprising is that all $L \neq 0$ systems show a reduction of the local moment by precisely half the free ion magnitude, independent of g_J, S, L, and J.

The TDR measurements for dM/dH in pulsed fields show a rich spectrum of ground state and excited state level crossing transitions. The addition of Ln ions appears to act as a perturbation to the Cr horseshoes shifting the transitions to higher fields and not dramatically altering the quantum energy levels. The Gd sample demonstrates a

double feature for ground state and excited state transitions and it is not clear at this time whether this result is an effect of the quenched orbital angular momentum.

Attempts to characterize the dM/dH behavior by fitting the DC susceptibility for the Cr horseshoe by direct diagonalization and the Gd sample with QMC yielded poor agreement with the dM/dH data, with the discrepancy increasing at higher fields. Given the good fit for $\chi(T)$ it might be possible to attain a better fit in dM/dH by using additional exchange constants for the Cr horseshoe. Since $\chi(T)$ reflects the susceptibility of the complete energy spectrum, it is possible there exists another set of exchange values which well reproduce $\chi(T)$ and offers a better characterization of the lowest energy levels observed in dM/dH, as seen in $Cr_{10}Cu_2$ where two different sets of exchange constants accurately reproduce the weak-field susceptibility while slightly altering the field dependence of the ground state level crossings. Despite this poor agreement for the Cr_6 horseshoe, fits of $\chi(T)$ using three exchange parameters for $Cr_{12}Y_4$ reproduces the dM/dH data quite well. This fit slightly increases the magnitude of the exchange paths for the Cr sites at the edges of the horseshoe shifting the peaks in dM/dH towards higher fields with respect to the plain Cr_6 horseshoe.

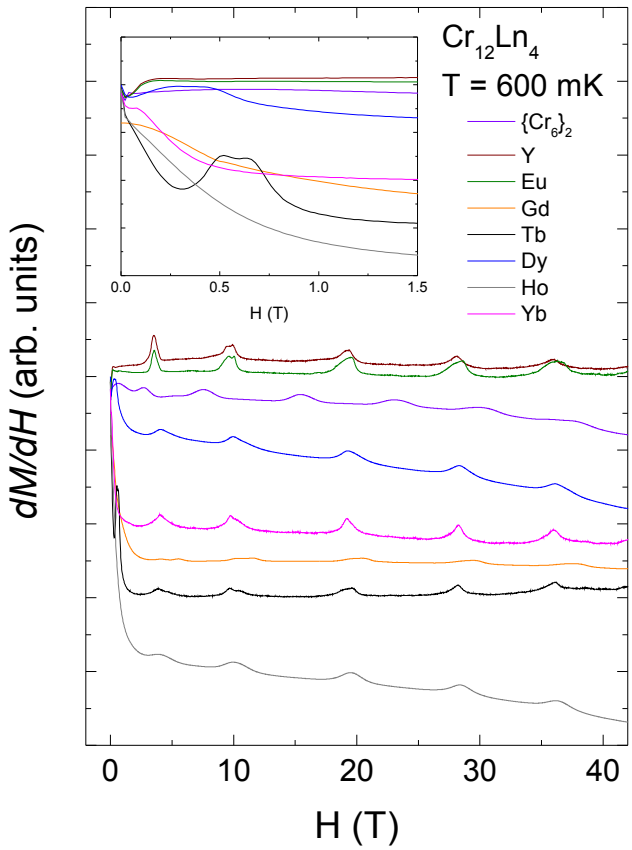

Figure 4.6: (Color online) Pulsed field data after subtracting background from the empty coil. The low-field behavior below 2 T arises from the 4 paramagnetic Ln ions, if present. Remaining linear background contributions arise from disparate pulse conditions compared to the empty coil shots. The inset shows peaks observed in the low field region below 1.5 T for the Dy and Tb samples.

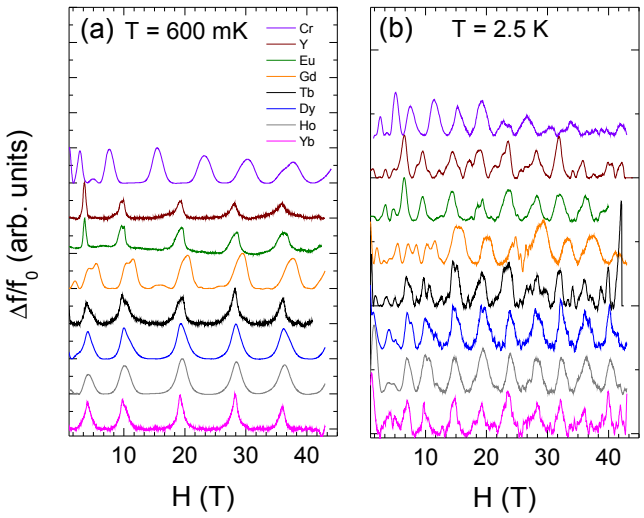

Figure 4.7: (Color online) Pulsed field data after subtracting the paramagnetic background at: (a) $T = 600$ mK and (b) $T = 2.5$ K. Even in pulsed fields, a rich spectra of excited level crossings are observed at 2.5 K.

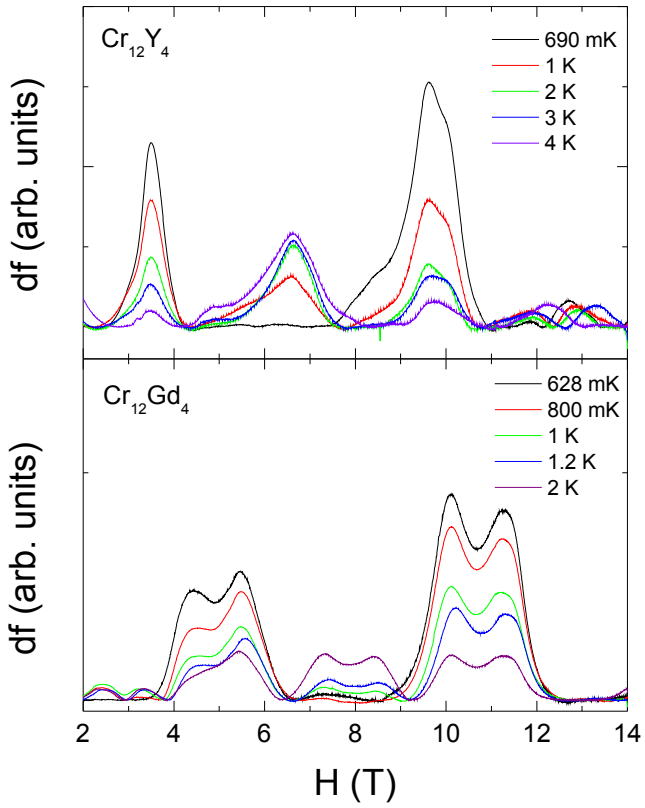

Figure 4.8: (Color online) Thermal evolution of H-dependent dM/dH for $Cr_{12}Y_4$ and $Cr_{12}Gd_4$ in DC field at a sweep rate of 0.1 T/min.

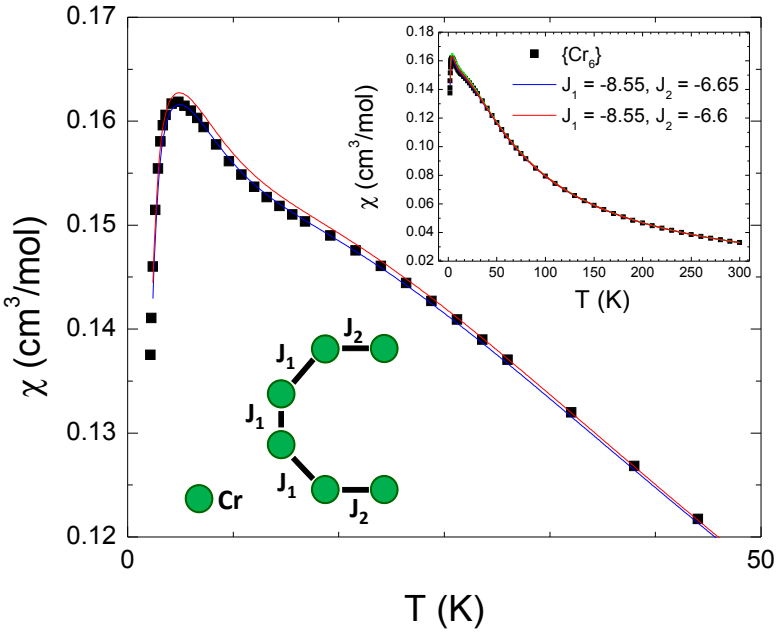

Figure 4.9: (Color online) FITMART fits of the DC susceptibility for $\{Cr_6\}_2$ for J_1 = -8.55 K and two values for $J2$. $J1$ corresponds to exchange values between three inner Cr-Cr sites, while $J2$ corresponds to the two Cr-Cr sites at each end of the horseshoe. A good fit is obtained which accounts for the peak at 4 K and the shoulder near 20 K. The top right inset shows the fit over the entire measured temperature region. The lower left inset is a cartoon depiction of the exchange parameters used.

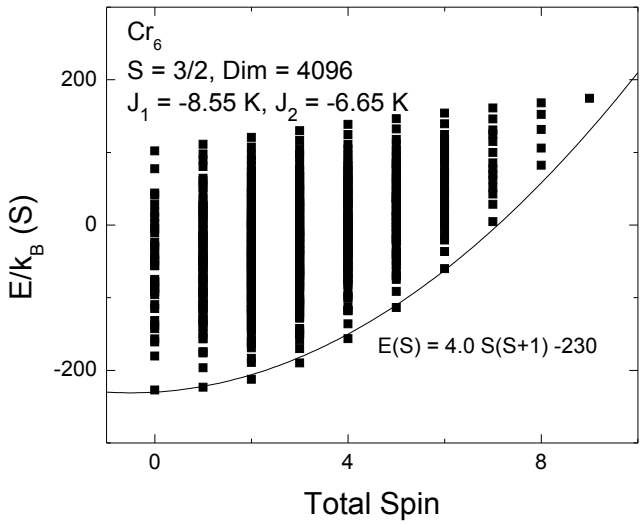

Figure 4.10: Energy diagram for the 4096 eigenstates [Dim $= (2S+1)^N$, $S = 3/2, N = 6$]. Lowest energy level per spin S can be fit with a quadratic equation.

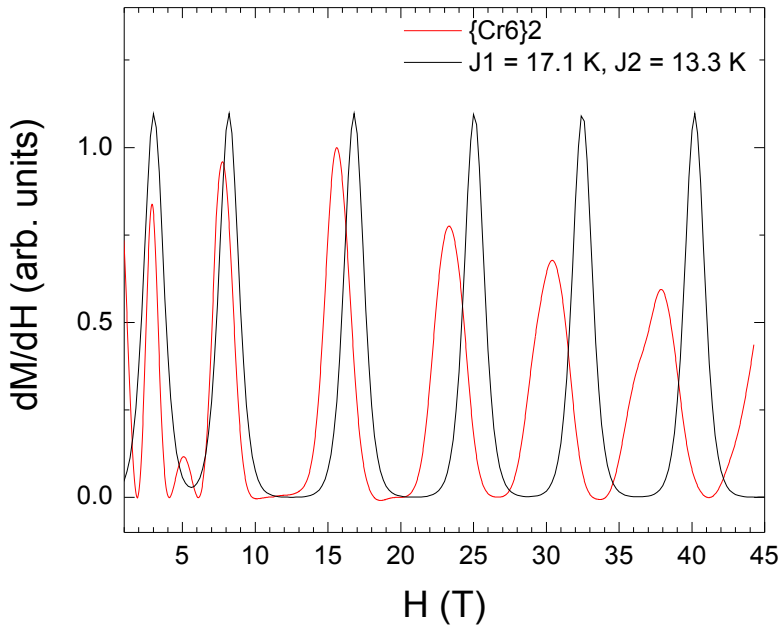

Figure 4.11: (Color online) Plot of dM/dH for $\{Cr_6\}_2$ measured in pulsed field (red) and calculated using FITMART with parameters $J1$ = -8.55 K, and $J2$ = -6.65 K. Calculated values overestimate peak positions in dM/dH with the disagreement increasing for higher fields.

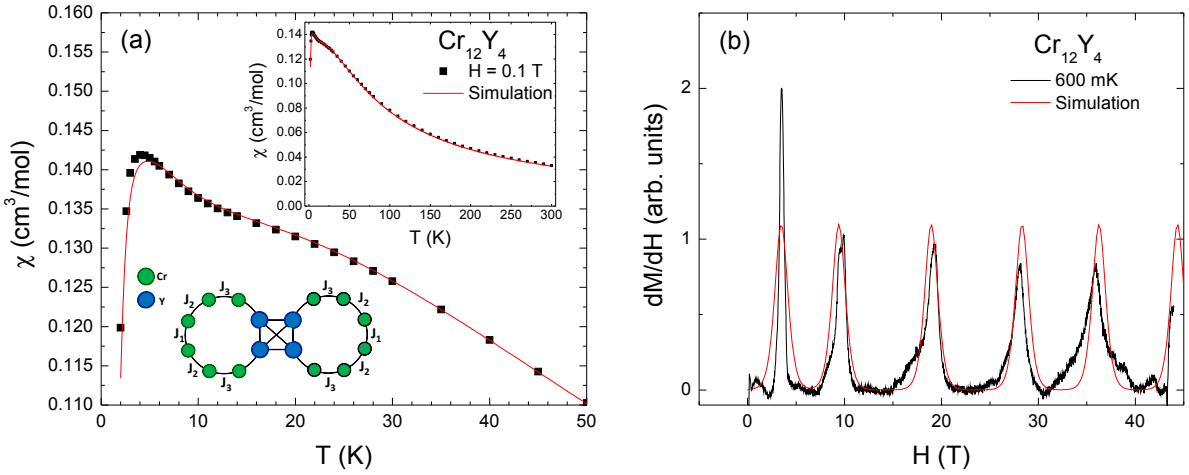

Figure 4.12: (Color online) (a) FITMART simulations of the DC susceptibility for $Cr_{12}Y_4$. The top right inset shows the fit over the entire measured temperature region. The lower left inset is a cartoon depiction for the three exchange parameters used with J_1 = -8.5 K, J_2 = -8.85 K, and J_3 = -7.9 K. (b) dM/dH

CHAPTER 5. INVESTIGATION OF FRUSTRATION IN $W_{72}V_{30}$ ICOSIDODECAHEDRON

5.1 Introduction

New successes in the area of polyoxometalate chemistry led to the synthesis of a family of large and quasi-spherical magnetic molecules consisting of 30 paramagnetic ions bridged by metal-oxygen ligands [5, 50–59]. The paramagnetic ions occupy the vertices of corner-sharing triangles of an icosidodecahedron - an Archimedian solid featuring 20 trangular faces and 12 pentagonal faces. The series consists of $Mo_{72}Fe_{30}$ [60–62], $Mo_{72}Cr_{30}$ [63], $Mo_{72}V_{30}$ [64, 65], and most recently $W_{72}V_{30}$ [66].

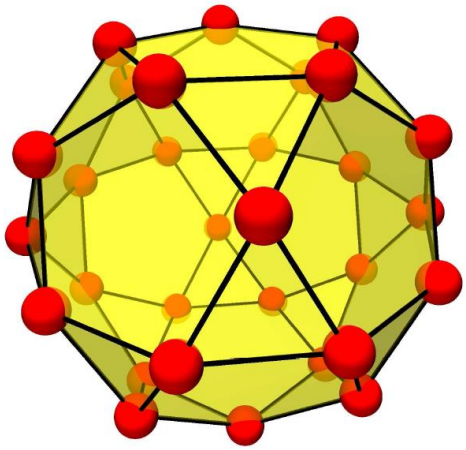

Figure 5.1: (Color online) Icosidodecahedron structure formed by the paramagnetic ions in the frustrated Keplerate magnetic molecules. The red spheres represent the 30 spin sites with 60 edges corresponding to exchange pathways between nearest-neighbor spins.

Fig. 5.1 illustrates the location of spin sites on the icosahedron. In this representation, the 60 black edge sites can be viewed as the interaction pathways between paramagnetic ions. If the interactions between ions in a triangular arrangement are antiferromagnetic in favor of an antiparallel aligned ground state, then the system is said to be geometrically frustrated [67–69]. In this sense the icosidoecahedron systems would serve as a finite-sized representation analogous to the archetypical class of two-dimensional frustrated systems known as kagomé lattice antiferromagnets [15, 16, 70–74].

These antiferromagnetically coupled frustrated systems exhibit unique properties compared to the 1-dimensional AFM ring systems discussed in Chapters 3 and 4 [75–77]. The first feature is the existence of many low-lying singlet states below the first excited state. The second feature is an extended plateau of the magnetization at an applied field of 1/3 the value of the saturation field at low temperatures. The third feature is a large jump to saturation as a function of applied fields associated with a large magnetocaloric effect [78, 79]. It is the hope that valuable insight about the physics of lattices such as the kagomé lattice can be gained by studying the DC magnetization, and local static and dynamic properties via NMR, and theoretical quantum calculations of these finite-size bodies.

Surprisingly, plots of the low-temperature magnetization versus external field H of $Mo_{72}Fe_{30}$ and $Mo_{72}Cr_{30}$ deviate substantially from the expectation for a regular icosidodecahedron with a single nearest-neighbor exchange interaction [55]. Although the temperature dependence of the weak-field susceptibility could be well reproduced by a Heisenberg model with a single exchange constant, the low-temperature magnetization could not. Later investigations revealed a strong dependence at low temperatures T of the differential susceptibility dM/dH on T and H [55, 80]. These results were explained in the framework of classical spin dynamics by assuming a distribution of random nearest-neighbor exchange interactions [55, 80]. This means that the exchange interactions between nearest neighbor spins of each molecule in the bulk sample are selected from

a random distribution whose mean exchange constant reproduces the high-temperature results. The mere fact that exchange interactions of a real substance might fluctuate around a mean value might not be surprising. What is indeed surprising is the large spread of values that had to be assumed: the exchange interactions J had to vary from half to twice the mean J (in the non-symmetric distribution) [55].

This work discuss the magnetic properties of a recent member of the family of Keplerates, $W_{72}V_{30}$, where 30 V^{4+} ions (spins $s = 1/2$) occupy the sites of the icosidodecahedron. In a previous work, the high temperature ($T > 70$ K) part of the susceptibility data measured at $H = 0.5$ T could be successfully explained using the quantum Monte Carlo method (QMC) on choosing the antiferromagnetic nearest-neighbor exchange constant J = -57.5 K and the spectroscopic splitting factor $g = 1.95$ [66]. These numerical values are associated with a Heisenberg Hamiltonian written as

$$\mathcal{H} = -2J \sum_{\langle i,j \rangle} \mathbf{S_i} \cdot \mathbf{S_j} + g\mu_B H \sum_i S_i^z. \tag{5.1}$$

Here $\langle i, j \rangle$ indicates a sum over distinct nearest-neighbor pairs and μ_B denotes the Bohr magneton. The QMC method could not be used to establish the magnetic properties of this system below 70 K due to the well-known negative-sign problem for frustrated spin systems [81]. Herein lies the important advantage of $W_{72}V_{30}$: Due to the small spin quantum number, $S = 1/2$, of the individual V^{4+} ions, rather than using classical methods, highly accurate quantum calculations can be performed despite the huge size ($2^{30} = 1,073,741,824$) of the Hilbert space dimension for this system. As shown below, we are able to calculate the relevant thermodynamic observables as functions of both temperature and applied field by means of the Finite-Temperature Lanczos Method (FTLM) [17, 18] conducted by Prof. Schnack. In particular, we are able to show that calculations based on Eqn. (5.1) on choosing a single value of J do not agree with the measured susceptibility data below 15 K and especially the field-dependence of the low-temperature magnetization. However, we are able to achieve reasonable agreement

between theory and experiment upon generalizing Eqn. (5.1) so that the numerical value of the exchange constant for any given nearest-neighbor pair is selected using a broad probability distribution constrained so that the mean value equals -115 K. Our analysis allows us to estimate the magnitude of the exchange disorder in the compound. As for the other Keplerates, that magnitude is surprisingly large, given the fact that x-ray structure investigations point to a highly symmetric exchange network.

5.2 Experimental details

Polycrystalline samples of $W_{72}V_30 = K_{14}(VO)_2$ [$K_{20} \subset \{(W)W_5O_{21}(SO_4)\}_{12}(VO)_{30}(SO_4)(H_2O)_{63}$] $\cdot$ ca.$150H_2O \equiv K_{14}(VO)_2 \cdot 1a$ *ca.*$150H_2O$ (MM = 25826.87 g/mol) were synthesized using the procedure given in Ref. [66]. The temperature dependence of the magnetic susceptibility $\chi = M/H$ for fixed $H = 0.1$ T was measured in a temperature range of 1.9 - 300 K using a Quantum Design Magnetic Properties Measurement System. Magnetization measurements were made at the high-field facilities at the Institute for Materials Research (IMR) of Tohoku University by Prof. Nojiri. Using pulsed fields, values of the magnetization were achieved for field strengths up to 50 T. Two types of cryostats, a conventional 4He bath type cryostat and a gas-flow type cryostat, were used for the low and high temperature ranges, respectively.

Nuclear magnetic resonance (NMR) measurements were carried out on ^{1}H ($I = 1/2, \gamma/(2\pi) = 42.5775$ MHz/T) and ^{51}V ($I = 7/2, \gamma/(2\pi) = 11.193$ MHz/T) by using an in-house phase-coherent spin-echo pulse spectrometer. The NMR spectra were obtained either by Fourier transform of the echo signal or by sweeping H. The NMR echo signal was obtained by means of a Hahn echo sequence with a typical $\pi/2$ pulse length of 1.0 μs. The nuclear spin-lattice relaxation time T_1 was measured by the saturation method with the frequency at the highest peak position of the NMR spectrum. For this system, NMR is a powerful tool for studying the magnetic properties and local spin dynamics of

the intrinsic susceptibility. This is because studies of the local behavior of the ^{1}H and ^{51}V nuclei are well suited to accurately decouple contributions from the impurity ions and the cluster of interest.

Numerical FTLM calculations for the Heisenberg model were performed on a supercomputer. We employed the SGI Altix 4700 as well as the SuperMIG cluster at the German Leibniz Supercomputing Center using openMP parallelization with up to 510 cores.

5.3 Weak field susceptibility

DC magnetization measurements were conducted in a Quantum Design SQUID magnetometer. A quantity of 150 mg of sample was placed into a gel capsule positioned inside a straw for measurements, with a 1×1 in^2 of Kimwipe tissue used to prevent the powder sample from shifting. To account for the diamagnetic background of the straw, capsule, and tissue, an empty background was measured. Fig. 5.2 (a) shows the temperature-dependent magnetic susceptibility χ in an external field of 0.1 T after correcting for the background, and diamagnetic and temperature-independent paramagnetic contributions from the sample. The raw experimental data, shown as the red open circles, follows a Curie-like behavior where the presence of two uncorrelated vanadyl ions (VO^{2+}) dominates the susceptibility at low temperatures. In order to observe the intrinsic susceptibility of interest arising from the 30 V ions of the icosidodecahedron it is necessary to subtract this contribution from the raw data. The calculated impurity susceptibility from the two V^{4+} ions of spin $S = 1/2$ (assuming $g = 2$) is calculated to be $\chi_{imp} = \frac{0.712}{T}$ cm^3/mol, and shown by the solid blue line in Fig. 5.2 (a). The vanadyl corrected result is given by the solid black circles corresponding to the intrinsic magnetic susceptibility χ_0 which features a broad peak near 20 K which rapidly decreases below 15 K indicating a singlet ground state. The data for χ_0 is shown in an expanded scale

in Fig. 5.2 (b). The solid curve corresponds to the results for χ_0 as obtained using the model Hamiltonian of Eqn. (5.1) for the above values $J = 115$ K and $g = 1.95$ (the "single-J model". Good agreement between theory and experiment is obtained only for $T > 15$ K. Below that temperature the two data sets depart markedly from each other.

5.4 Low temperature magnetization

In Fig. 5.3 the solid blue curve corresponds to our data for the intrinsic magnetization versus external field as obtained by pulsed-field measurements at 0.5 K. The experimental data is corrected for two lattice VO^{2+}. The black dashed-dotted curve is the result obtained for the single-J model. Note the striking staircase behavior of the theoretical curve for this temperature. Surprisingly, the experimental data shows no signs of staircase behavior. This negative result is similar to that for $Mo_{72}Fe_{30}$ and $Mo_{72}Cr_{30}$. The latter systems possess much smaller exchange couplings so one could imagine that the expected steps are more readily washed out due to structural fluctuations or possibly as a result of single-ion anisotropy or Dzyaloshinskii-Moriya interactions [62]. However, for the present system the magnetization steps of the theory are so well separated that one would expect to see at least a hint of them. Moreover, single-ion anisotropy is absent for V^{4+} ions with spin $s = 1/2$.

5.5 Distribution of nearest-neighbor couplings

In view of the above striking discrepancies between experiment and theory, and in particular the failure of the single-J model, we follow the idea of Ref. [55] and assume that, due to possible low-temperature structural distortions (as e.g. observed in some kagome lattices [82–84]) and the great sensitivity of the exchange interaction on the details of the local environment (highly charged anionic and cationic lattice with many dipolar water molecules that possibly order), the interaction strength between each nearest-neighbor

pair of spins is effectively randomly distributed. It is very important at this point to understand that a symmetric structural distortion that would express itself in just a few distinct exchange interactions would only alter the staircase in a minor way but could not wash it out completely. For this to happen one needs a very large number of different interactions within each and every molecule.

Since the calculations are very computer-intensive we aim for a coarse estimate of the size of the exchange variation. To this end we used a flat distribution with $\bar{J} - \Delta J < J < \bar{J} + \Delta J$ and evaluated the magnetic observables for $\Delta J/\bar{J} = 0.1, 0.2, 0.3, 0.5$, with the mean $\bar{J} = -115$ K. Fig. 5.4 shows the magnetization versus field for various choices of ΔJ. As can be deduced already from a small number of samples, step-like behavior persists for $\Delta J/\bar{J} = 0.2$ and below. It turns out that the data for $\Delta J/\bar{J} = 0.3$ comes closest to the experimental data, and that choice is shown as the red curve in Fig. 5.3. Since we averaged over only 50 samples that curve is still somewhat wiggly but it is sufficiently converged to warrant our conclusions.

Finally, shown in Fig. 5.5 are the results for the intrinsic susceptibility χ_0 as obtained from our measurements, for the single-J model, as well as for exchange variation with $\Delta J/\bar{J} = 0.3$. We conclude that the introduction of exchange variation yields results that are in reasonably good agreement with our experimental susceptibility data.

5.6 ^{1}H- and ^{51}V-NMR spectrum

The temperature-dependent ^{1}H-NMR spectra were measured for a manetic field $H = 2.86$ T from 1.8 to 150 K. A single NMR line is observed which broadens upon decreasing temperature. Fig. 5.6 shows the temperature dependence of the line width determined by the full width at half maximum (FWHM). For $W_{72}V_{30}$, the FWHM can be expressed as the sum $a + bM_{imp} + cM_0$. The constant term a originates from nuclear-nuclear dipole interactions of the order of 10 Oe. The second and third terms represent the dipolar field

contributions produced by the V^{4+} from the VO^{2+} ions and the 30 spins of the intrinsic magnetic molecule, respectively. The quantities M_{imp} and M_0 are the corresponding magnetizations and b and c are parameters related to the average dipolar hyperfine coupling associated with the two sets of V^{4+} spins. In particular M_{imp} is proportional to the standard expression $\tanh(\mu_B H/k_B T)$ for uncorrelated spins $s = 1/2$. The increase of the FWHM at low temperatures is well reproduced by the above expression with $a \sim 13$ Oe and $b \sim 6$ Oe/μ_B, as shown bt the solid lines in Fig. 5.6 (a). Subtracting these contributions from the total FWHM, we obtain the intrinsic line width denoted by $(\text{FWHM})_0$, which is proportional to M_0. That data is shown in Fig. 5.6 (b) and it has a broad peak around 10 K. The solid curve in Fig. 5.6 (b) corresponds to the theoretical result for M_0 for exchange disorder $\Delta J/\bar{J} = 0.3$ and for an external magnetic field of H = 2.86 T. The experimental data is in reasonable agreement with the theoretical result. In this context one should also keep in mind that the NMR relaxation deviates from a single exponential behavior due to many inequivalent proton positions of this water rich substance [85, 86].

Fig. 5.7 (a) shows typical ^{51}V-NMR spectra measured at f = 80.7 MHz at various temperatures. The ^{51}V nucleus has nuclear spin $I = 7/2$ so that one expects seven quadrupole-split lines. These spectra can be calculated using a simple nuclear spin Hamiltonian [87]

$$\mathcal{H} = -\gamma\hbar\mathbf{I}\cdot\mathbf{H_{eff}} + \frac{h\nu_Q}{6}(3I_z^2 - I(I+1)), \tag{5.2}$$

where $\mathbf{H_{eff}}$ is the effective field (the sum of the external field $\mathbf{H}$ and the hyperfine field $\mathbf{H_{hf}}$) at the V^{4+} site, h is Planck's constant, and ν_Q is the nuclear quadrupole frequency. The latter quantity is proportional to the Electric Field Gradient (EFG) at the V^{4+} site (an asymmetric parameter of the EFG is assumed to be zero for simplicity). The blue curve in Fig. 5.7 (a) shows a typical powder-pattern spectrum calculated from the simple Hamiltonian with $\nu_Q = 0.25$ MHz. In order to reproduce the observed spectrum, one needs to introduce a distribution of ν_Q. By taking $\sim$ 40% distributions ($\Delta\nu_Q \sim$

0.1 MHz), one can well reproduce the observed spectrum as shown by the red curve in the figure. The wide distribution of ν_Q, which reflects the distribution of the EFG, indicates a high degree of inhomogeneity of the local environments of the vanadium spins. In $W_{72}V_{30}$ the vanadium ions are sixfold coordinated. The vanadium-oxygen distances which bridge to neighboring vanadium ions vary by about ± 0.02 whereas the distances to the two remaining oxygen sites vary by 0.2 Åwhen comparing the various vanadium coordination spheres (see crystal structure in [66]). We speculate that this is one source of the distribution of exchange couplings discussed above.

The temperature dependence of the NMR shift (denoted by K) and FWHM for the ^{51}V-NMR spectrum is shown in Fig. 5.7 (b); both show a very weak temperature dependence. The hyperfine coupling constant can be estimated from the T-dependence of K by comparing with the T-dependence of χ_0. The resulting value is very small, less than 100 Oe/μ_B. Usually the hyperfine coupling constant for V^{4+} ions will be dominated by core-polarization, of the order of 100 kOe/μ_B [88], which is three orders of magnitude larger than our result. One might attempt to explain the very small value of K by suggesting that the separate contributions to the total hyperfine field from, first, intra-atomic interactions of d-electron orbitals and dipolar hyperfine field and, second, the transferred hyperfine field due to other V ions, nearly cancel. We believe, that this is not the case because $1/T_1$ of ^{51}V is almost 50 times smaller than that of ^{1}H as will be shown in the following section. Since $1/T_1$ is given by a sum of all contributions of the hyperfine fields and each contribution is proportional to the square of the hyperfine coupling constant, it follows that $1/T_1$ of ^{51}V should be larger than that of ^{1}H even if the total hyperfine field is small due to the cancellation. At present we do not have a clear explanation for the small hyperfine field on V in $W_{72}V_{30}$. It should however be noted that the observed V-NMR signal is not coming from non-magnetic V impurities as can be clearly seen in the $1/T_1$ data where ^{51}V-T_1 shows a similar T-dependence with that of ^{1}H-T_1.

5.7 Nuclear spin-lattice relaxation

To investigate the dynamical properties of the V^{4+} spins, we have carried out ^{1}H-T_1 measurements in the temperature range 1.5-100 K. We find that $1/T_1$ is almost independent of temperature above $\sim$ 30 K. Below $\sim$ 30 K, with decreasing temperature, $1/T_1$ starts to increase and then shows a peak around 6 K at $H = 1.17$ T. As the external magnetic field increases, the peak temperature of $1/T_1$ shifts to higher temperatures and at the same time the peak height decreases.

In recent years it has been found, that in many antiferromagnetic rings and clusters of spins $s > 1/2$ the quantity $1/T_1$ is well approximated by the formula

$$\frac{1}{T_1} = A\chi_0 T \frac{\Gamma}{\Gamma^2 + \omega_L^2}, \tag{5.3}$$

where the electronic correlation frequency Γ is given by a near-universal power law temperature dependence with an exponent in the range 3.5 ± 0.5, and A is a fitting constant independent of both H and T related to the hyperfine field [89–91]. The form of Eqn. (5.3) is due to the fact that the damping of the equilibrium fluctuations of the z-component of the total magnetization, S_z, is monoexponential. Specifically this is due to a dynamical decoupling of S_z from the slow degrees of freedom originating from the discreteness of the energy spectrum and the conservation law $[S_z, H_0]$, where H_0 denotes the Heisenberg model Hamiltonian of exchange coupled ion spins [92]. It follows from Eqn. (5.3) that the quantity $1/(T_1 T \chi_0)$, see Fig. 5.8 (a), has a maximum as a function of T and fixed H when $\Gamma = \omega_L$, and its maximum value is proportional to $1/H$. A quantitative microscopic theory explaining all of these features has been given in [93] for spins $s > 1/2$ and in particular the numerical value of the power law exponent originates from one-phonon acoustic processes. It is significant that, although $s = 1/2$, our data for $W_{72}V_{30}$ below 20 K exhibits the very same behavior, and we find $A = 4.7 \times 10^{11}$ rad Hz^2 mol/(Kcm^3) and $\Gamma = 6.3 \times 10^5 T^{3.5}$ rad Hz, where T denotes the temperature in units of Kelvins. In $W_{72}V_{30}$ we find that the paramagnetic fluctuations are dominant for the

high-temperature range where the fluctuation frequency is independent of T.

In general, one expects that Eqn. (5.3) should be supplemented by a second Lorentzian, where the nuclear Larmor frequency ω_L is replaced by the electron Larmor frequency ω_e. However, if Γ is of the order of ω_L, the contribution of the second Lorentzian is negligible. To confirm this experimentally, we performed $1/T_1$ measurements on two different nuclei, ^{1}H and ^{51}V. Values of T_1 for both nuclei were measured at $f = 77.8$ MHz for ^{51}V-NMR and at 298 MHz for ^{1}H-NMR, respectively, so as to achieve the same value of ω_e, that is the same magnetic field. The two sets of experimental data are shown in Fig. 5.8 (b) and they are both successfully fitted by Eqn. (5.3) (solid curves). If in Eqn. (5.3) one was to include ω_e, the peak position of $1/T_1$ must be observed at the same temperature. These measurements provide a firm confirmation that the fluctuation frequency of V^{4+} spins slow down to the order of MHz.[80]

In antiferromagnetic rings and clusters of spins $s > 1/2$ the peak in $1/(T_1 T \chi_0)$ is usually observed for temperatures of the order of the exchange coupling constant [89, 92]. In [93] this is explained by the fact that the relaxation mechanism when $s > 1/2$ is governed by the quasi-continuum portion of the quadrupolar fluctuation spectrum and not by the lowest excitation lines. By contrast, in $W_{72}V_{30}$ we find that the peak temperature ($\approx$ 6-10 K) is an order of magnitude smaller than $J = 115$ K. We speculate that this difference in behavior could be explained by invoking the modifications of the microscopic theory proposed in [93] for spins $s = 1/2$, namely by using a dipolar channel or fluctuating Dzyaloshinskii-Moriya interactions. However, this remains to be confirmed by detailed calculations that are outside the scope of the present work.

5.8 Conclusions

We have investigated magnetic properties and spin dynamics of $W_{72}V_{30}$ magnetic molecules by low temperature magnetization, magnetic susceptibility, proton and vana-

dium NMR measurements, and theoretical studies. Our most striking experimental finding is that the field-dependent magnetization at 0.5 K, as obtained using a pulsed magnetic field, increases monotonically up to 50 T without showing any sign of staircase behavior. This is contrary to the predictions of any model based on a single value of the nearest-neighbor exchange coupling. Also we find that a single-J model fails to describe the temperature dependence of the intrinsic weak-field magnetic susceptibility χ_0 below 15 K, as obtained from a SQUID measurement. However, both sets of experimental observations are reproduced to reasonable accuracy upon introducing a model based on a broad distribution of values of the nearest-neighbor coupling.

Complementing the SQUID and pulsed fields measurements we have also performed detailed ^{1}H-NMR and ^{51}V-NMR measurements. We find that the temperature dependence of χ_0 as estimated from the proton NMR spectrum is in satisfactory agreement with that obtained from our SQUID measurements. From ^{51}V-NMR spectrum measurements, a high degree of inhomogeneity of the local environment of V ions is suggested by the observation of a wide distribution of quadrupole frequencies. Inhomogeneity of the local environment is also suggested by the temperature dependence of the observed line width and NMR shift of ^{51}V-NMR. This characteristic of the local environment is consistent with a large distribution of J-values indicated by the theoretical studies. T_1 measurements of both ^{1}H and ^{51}V reveal the existence of slow spin dynamics at low temperatures. In particular, the fluctuation frequency of the interacting system of V^{4+} spins is found to show a power law behavior, of the form $T^{3.5}$ at temperatures below 30 K, i.e., the same behavior that has been found for many antiferromagnetic rings and clusters of spins $s > 1/2$ [90, 93]. Finally, we remark that the need for a multi-J model as suggested by our experimental and theoretical studies might be correlated to the presence of significant local distortions of the spherical shape of the $W_{72}V_{30}$ molecules at low temperatures. Thus it would be very helpful if low-temperature X-ray diffraction measurements could test this suggestion.

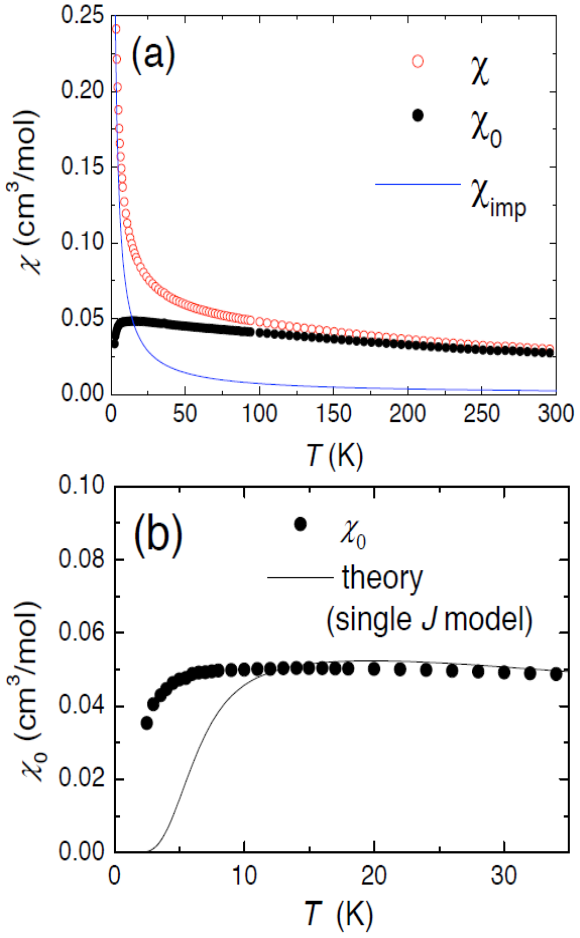

Figure 5.2: (Color online) Molar manetic susceptibility at $H = 0.1$ T as a function of temperature: (a) measured data of the compound (red circles), contribution of two lattice VO^{2+} (solid blue curve), and intrinsic susceptibility χ_0 of the Keplerate anion $W_{72}V_{30}$ (black circles). (b) intrinsic susceptibility χ_0 (black circles) and theoretical susceptibility using the single-J model (see text).

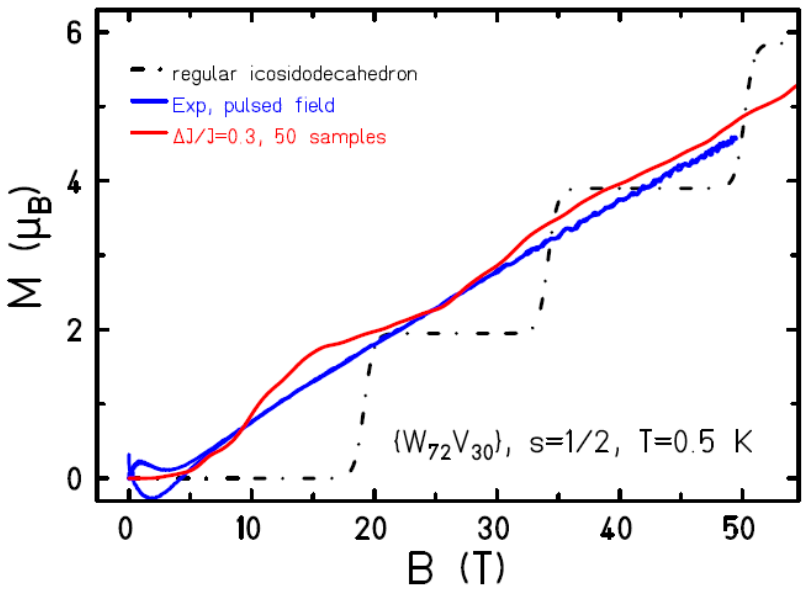

Figure 5.3: (Color online) Intrinsic magnetization of the Keplerate ion $W_{72}V_{30}$ as a function of applied field for $T = 0.5$ K. Pulsed field data are given by the blue curve, the theoretical magnetization for the single-J model is shown by the black dashed-dotted curve, and for the multiple-J model with $\Delta J/\bar{J} = 0.3$ by the red curve.

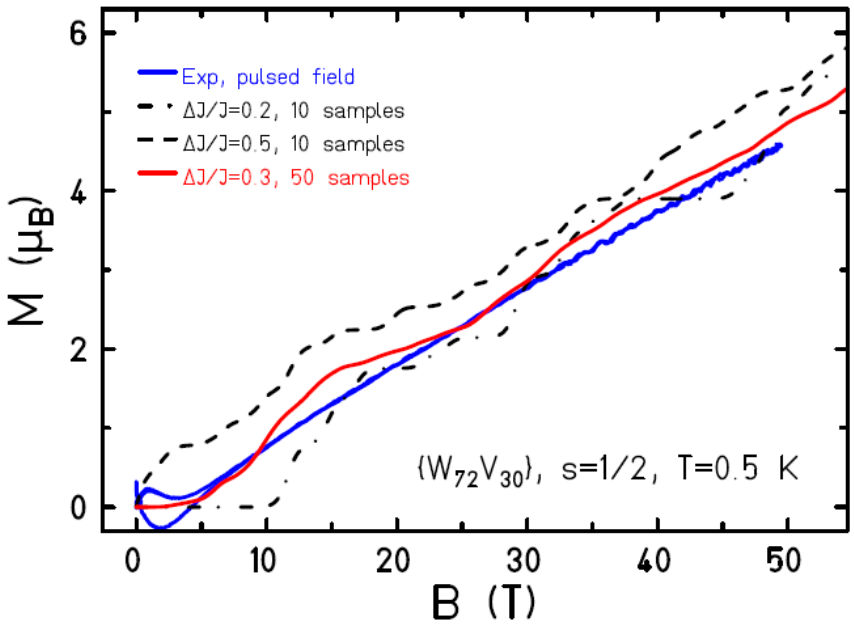

Figure 5.4: (Color online) Intrinsic magnetization of the Keplerate ion $W_{72}V_{30}$ as a function of applied field for $T = 0.5$ K. Curves for various exchange variations $\Delta J/\bar{J}$ are compared to the pulsed field data.

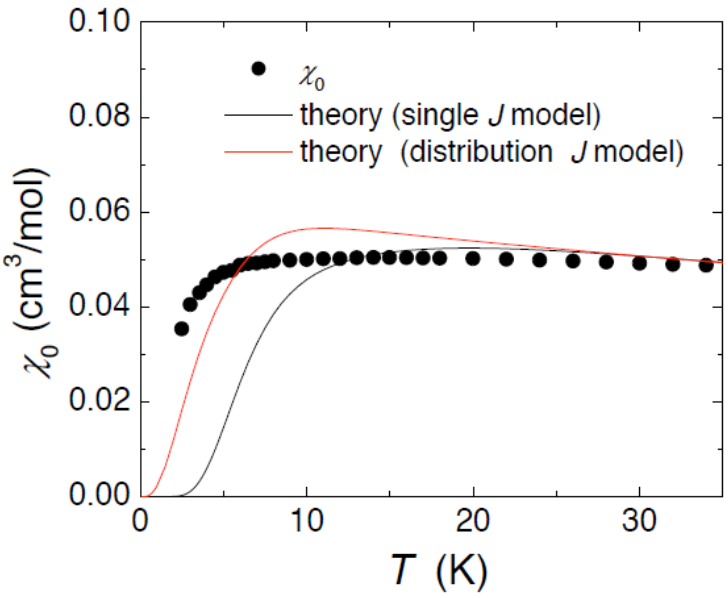

Figure 5.5: (Color online) Molar magnetic susceptibility, χ_0, at $H = 0.1$ T as a function of temperature. The curves are the result of our simulations for $\Delta J/\bar{J} = 0.3$ and 0.

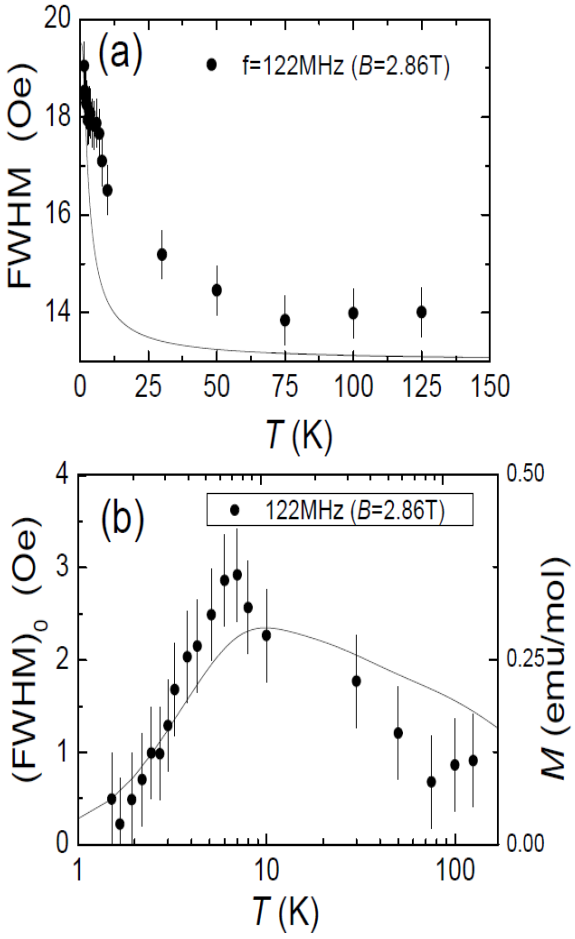

Figure 5.6: (a) ^{1}H-NMR line width (FWHM) at $H = 2.86$ T as a function of temperature. The solid curve shows the fitting result $a + bM_{imp}$ (see text). (b) T-dependence of the intrinsic line width, $(\mathrm{FWHM})_0$, given by cM_0. The solid line is calculated T-dependence of the magnetization with the exchange disorder $\Delta J/\bar{J} = 0.3$ for the same field.

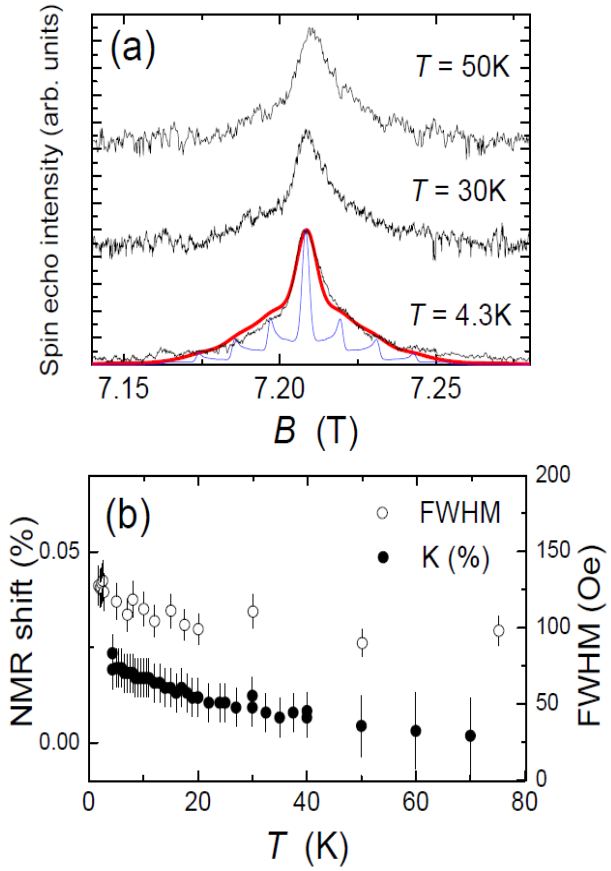

Figure 5.7: (Color online) (a) Typical ^{51}V-NMR spectra measured at $f = 80.7$ MHz for various temperatures. The blue curve shows a typical powder-pattern NMR spectrum with $\nu_Q = 0.25$ MHz. The red curve is the simulated NMR spectrum with $\sim$ 40% distribution of ν_Q. (b) Temperature dependence of ^{51}V NMR shift and line width (FWHM).

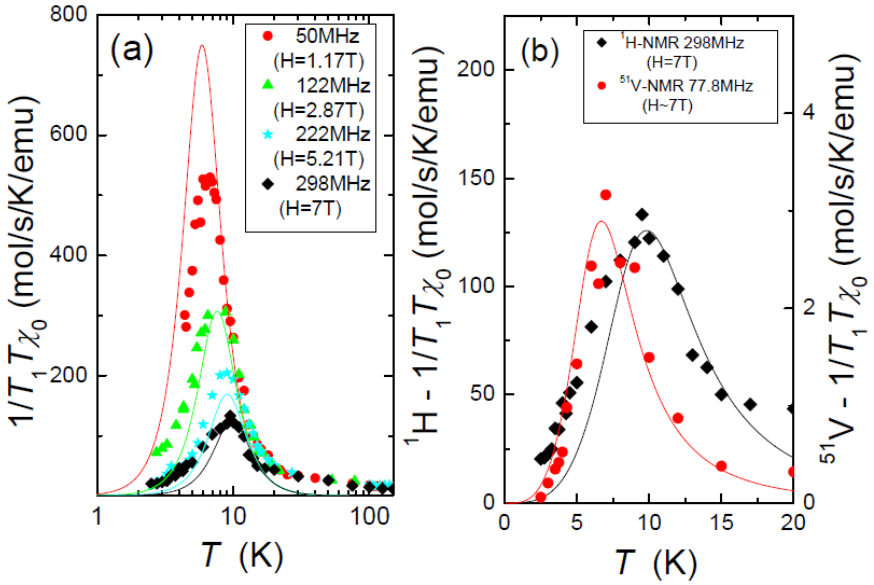

Figure 5.8: (Color online) (a) T-dependence of $1/(T_1T\chi_0)$ for ^{1}H-NMR. Solid lines are theoretical curves calculated by using Eqn. (5.3). (b) T-dependences of $1/(T_1T\chi_0)$ for ^{1}H-NMR (f = 298 MHz) and ^{51}V-NMR (f = 77.8 MHz) at the same magnetic field $H \approx 7$ T (that is, same electron Larmor frequency ω_e).

CHAPTER 6. ELECTRONIC AND MAGNETIC PROPERTIES OF $Ba_{1-x}K_xMn_2As_2$ STUDIED BY ^{55}Mn AND ^{75}As NMR

6.1 Introduction

The family of $BaTM_2As_2$ (T_M = Mn, Fe, Co, Ni, and Zn) compounds have sparked great research interest as variations in the $3d$ electron count yield a wide range of physical properties.[94–96] Systems which share characteristics with parent compounds of both iron pnictides and high-T_c cuprates could offer a pathway toward further understanding high-T_c superconductors. In both classes superconductivity can be induced by electron or hole doping, or by applying high pressures. For example, $BaFe_2As_2$ is metallic with antiferromagnetic (AFM) ordering arising from a spin-density wave from itinerant carriers[96], while La_2CuO_4 is a local moment AFM insulator [94]. $BaMn_2As_2$ and $Ba_{1-x}K_xMn_2As_2$ may lead to systems which help characterize the principles of high-T_c superconductivity.

$BaMn_2As_2$ crystallizes in the same elongated $ThCr_2Si_2$-type structure as other '122'systems. The magnetic properties are characterized as a G-type local moment AFM with a high Néel temperature, T_N = 625(1) K, and local moment μ = 3.88(4) μ_B/Mn at 10 K. The moments arise from Mn^{2+} ions with local moments of spin S=5/2. The electronic properties are characterized as a small-band-gap insulator with $E_{gap} \approx 0.05$ eV and an electronic linear heat capacity coefficient $\gamma = 0$ [96–98]. In this study we measure the spectra and spin-lattice relaxation process of ^{55}Mn and ^{75}As-NMR to investigate the

local magnetic and electronic properties from a microscopic point of view.

Electron doping[99] and pressure mesurements[100] of $BaMn_2As_2$ have demonstrated a transition to metallic ground states. Hole-doping by substitution of K for Ba results in the metallic system $Ba_{1-x}K_xMn_2As_2$ with the same $ThCr_2Si_2$ crystal structure and similar magnetic properties. This behavior is observed for x as low as 1.6%. The magnitude of the ordered Mn moment has been demonstrated to be nearly independent of x, but a strong T_N dependence on x which decrease by ≈ 140 K at $x = 0.4$, with respect to $T_N = 625$ K for $x = 0$, as determined by neutron diffraction (ND).[101] Recent studies of single crystals report a small ferromagnetic moment which coexists with the AFM local Mn moment. The FM arises below approximately 50 K and the low-T saturation moment is estimated at $0.02 - 0.08\ \mu_B$/Mn, aligned along the ab-plane.[102]

6.2 Experimental details

Single crystals of $BaMn_2As_2$ and $Ba_{1-x}K_xMn_2As_2$ were synthesized group using solid state reaction out of Sn flux by Dr. Abhishek Pandey of Prof. Johnston's group. $BaMn_2As_2$ crystals were grown in an alumina crucible then sealed in a quartz tube, whereas the K-doped systems were sealed inside Ta tubes. Chemical compositions were determined using energy dispersive x-ray analysis (EDX)[96, 99]. The K-concentration x for crystals used in this study ranged from $0 \leq x \leq 0.4$.

Nuclear magnetic resonance (NMR) spectra and spin-lattice relaxation measurements of ^{55}Mn ($I = 5/2$; $\gamma/2\pi = 10.5000$ MHz/T) and ^{75}As ($I = 3/2$; $\gamma/2\pi = 7.2919$ MHz/T) nuclei were conducted using a homemade phase-coherent spin-echo pulse spectrometer. A large internal field H_{int} from the AFM-ordered Mn ions allowed for zero-field and in-field measurements of the ^{55}Mn nuclei. The ^{75}As-NMR and most ^{55}Mn-NMR spectra measurements were collected by either sweeping the magnetic field or taking the Fourier transform of the echo signal. For K-doped systems, the ^{55}Mn-NMR spectra in zero field

and fields H $\parallel$ *ab*-plane were collected in steps of frequency by measuring the intensity of the Hahn spin-echo. The pulse conditions were optimized for the maximum echo intensity for each frequency point in the NMR spectra. The nuclear spin-lattice relaxation rates $1/T_1$ were obtained using a conventional single saturation pulse method at the central transition.

6.3 Zero-field ^{55}Mn-NMR spectrum

Fig. 6.1 shows the ^{55}Mn-NMR spectrum in the AFM-ordered state for $BaMn_2As_2$ and $Ba_{1-x}K_xMn_2As_2$ in zero external field at temperature $T = 5$ K. For the un-doped $BaMn_2As_2$ spectrum, five very sharp quadrupole-split transition peaks were observed, where the sharpness indicates a high quality sample. The resonance frequency of the central transition at $f = 242$ MHz corresponds to a local hyperfine field of $H_{hf} = 23.05$ T. H_{hf} is proportional to $A_{hf}\langle S\rangle$ where A_{hf} is a hyperfine coupling constant and $\langle S\rangle$ is the average Mn spin moment. The hyperfine field at the Mn sites mainly originates from core-polarization from 3*d* electrons and is oriented in a direction opposite to that of the Mn spin moment. For $H_{hf} = 23.05$ T and a reported AFM-ordered spin moment $\mu = 3.88(4)\ \mu_B$/Mn from neutron diffraction[97], the hyperfine coupling constant is estimated as $A_{hf} = -59.4$ kOe/μ_B. This experimental value is lower than previously reported values for Mn of $A_{hf} = -100$ kOe/μ_B[103] suggesting an additional transfer-hyperfine contribution of $A_{tran} \approx 10.1$ kOe/μ_B from each of the four nearest neighbor (n.n.) Mn ions. The temperature dependence of the ^{55}Mn spectrum shows only a slight decrease in resonance frequency, < 10 %, suggesting $T_N \gg 300$ K in agreement with a reported value of $T_N = 625(1)$ K neutron diffraction[97].

^{55}Mn-NMR spectra for K-doped systems show a broadening of the linewidth and a shift to lower frequency upon increasing x. The broadening of the linewidth is attributed to increased spin disorder due to lattice distortion as a result of doping. While five peaks

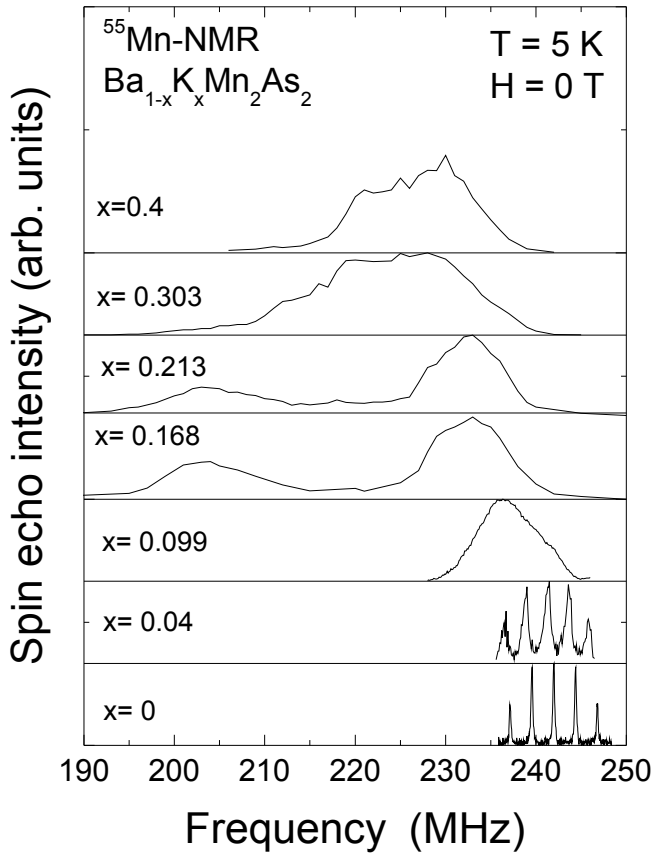

Figure 6.1: Zero-field ^{55}Mn NMR spectra at 5 K for different K-concentrations, x with five sharp quadrupole peaks are observed for $x = 0$ and 0.04. For larger x, broadening of the spectrum indicates spin disorder at the Mn sites. The peak observed near 203 MHz likely arises from a small MnAs impurity.

are observed for x=0.04, the linewidths for K-concentrations of $x \geq 0.099$ become too broad to observe distinct quadrupole split peaks. Further, for $x \geq 0.099$, a reduction of the rf power was needed to maximize the ^{55}Mn-NMR signal. This RF enhancement suggests coexistence of weak ferromagnetic (FM) ordering with the G-type AFM ordering in $Ba_{1-x}K_xMn_2As_2$ consistent with recent studies[102].

Fig. 6.2 plots the peak position of the ^{55}Mn spectra and average Mn spin moment as a function of K-concentration x. Increasing x shifts the spectrum towards lower

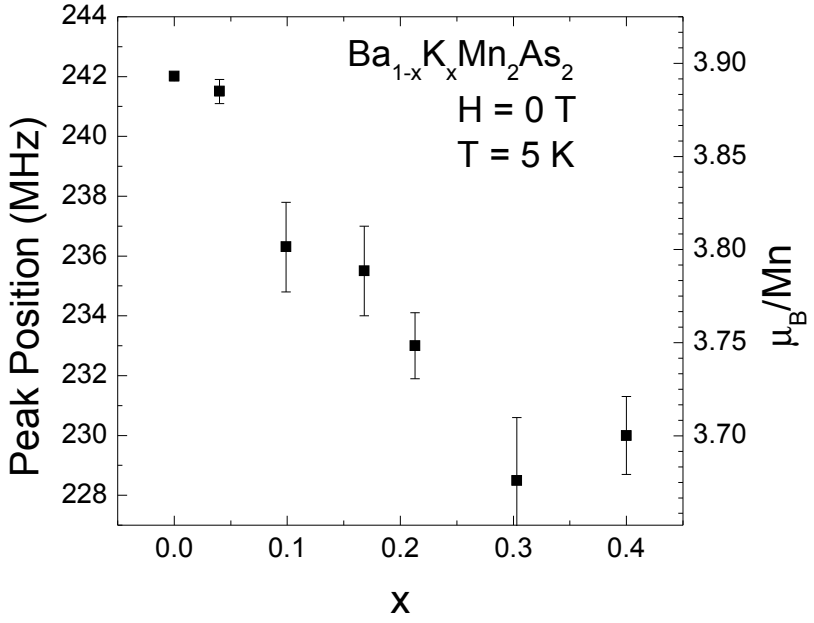

Figure 6.2: Plot of the central transition peak for zero-field ^{55}Mn NMR spectra and corresponding magnetic moment per Mn ion assuming a constant hyperfine coupling constant $A_{hf} = 59.4$ kOe/μ_B. This suggests a net decrease in the local moment as K-concentration increases.

frequencies, indicating a decrease in the local hyperfine field. If one were to assume the same hyperfine coupling constant A_{hf} for the K-doped system as for the un-doped system, then this indicates a decrease in the average Mn spin moment. The resonance frequency (average Mn spin moment) decreases by approximately 5 % over the observed concentrations. This is in contrast to results from neutron diffraction which report almost no change in the Mn moment from $\mu = 3.88(4)$ to 3.85(15) for $x = 0$ and $x = 0.4$ single crystals, or a possible small increase to $\mu = 4.21(12)$ and 4.25(12) for $x = 0.05$ and $X = 0.25$ powder samples.[99, 101]

A second NMR peak observed near 203 MHz for intermediate concentrations x=0.168 and 0.303 is likely ^{75}As from a small FM MnAs impurity. The existence of a weak FM transition near $T = 325$ K in DC magnetization, strong RF enhancement, and the

observation of a Korringa relation for $1/T_1$ are consistent with previous NMR studies on MnAs [104]. If this signal indeed arises from MnAs impurity, then one would expect a superposition of the intrinsic ^{55}Mn spectrum and an impurity contribution near 231 MHz $\leq f \leq$ 239 MHz.

6.4 In-field ^{55}Mn-NMR spectrum

In applied fields, the local field at the Mn nuclei will be given by $\overrightarrow{H}_{loc} = \overrightarrow{H}_{app} + \overrightarrow{H}_{hf}$, where H_{app} is the applied magnetic field and H_{hf} is the local hyperfine field. For G-type AFM ordering, n.n. Mn moments in the tetragonal plane and Mn moments between successive planes along the c-axis are antiferromagnetically aligned with ordered moments oriented along the tetragonal c-axis.

Fig. 6.3 (a) shows a splitting of the zero-field ^{55}Mn-NMR spectra in $BaMn_2As_2$ for $H_{app} \parallel c$-axis at 4.2 K. In zero-field the local field at the Mn nuclei is equal to the hyperfine field: $H_{app} = 0$ T; $H_{loc} = H_{hf} = 23.05$ T. For Mn spin moments aligned parallel (antiparallel) to the c-axis, core-polarization from the Mn $3d$-elecrons will yield hyperfine fields H_{hf} antiparallel (parallel) to the c-axis at the Mn nuclei. Assuming H_{hf} stays constant, Mn spin moments aligned with the c-axis will observe a decrease in H_{loc} upon increasing H_{app}, for $H_{app} \parallel c$-axis and $|H_{app}| < |H_{hf}|$. This is observed as a shift in the ^{55}Mn-NMR spectrum towards lower frequencies. Conversely, shifts towards higher frequencies correspond to an increase in H_{hf} arising from Mn spin moments aligned antiparallel to the c-axis. The field dependent spectra still observe five sharp quadrupole split peaks suggesting a homogeneous distribution of the nuclear Mn spins. Fig. 6.3 (b) plots the peak position of the quadrupole-split ^{55}Mn NMR spectra as a function of applied field. The slope is $\approx$ 10.5 MHz/T, corresponding to the nuclear gyromagnetic ratio γ for ^{55}Mn.

Fig. 6.3 (c) shows the ^{55}Mn-NMR spectra for $H_{app} \parallel ab$-plane at T=4.2 K. In

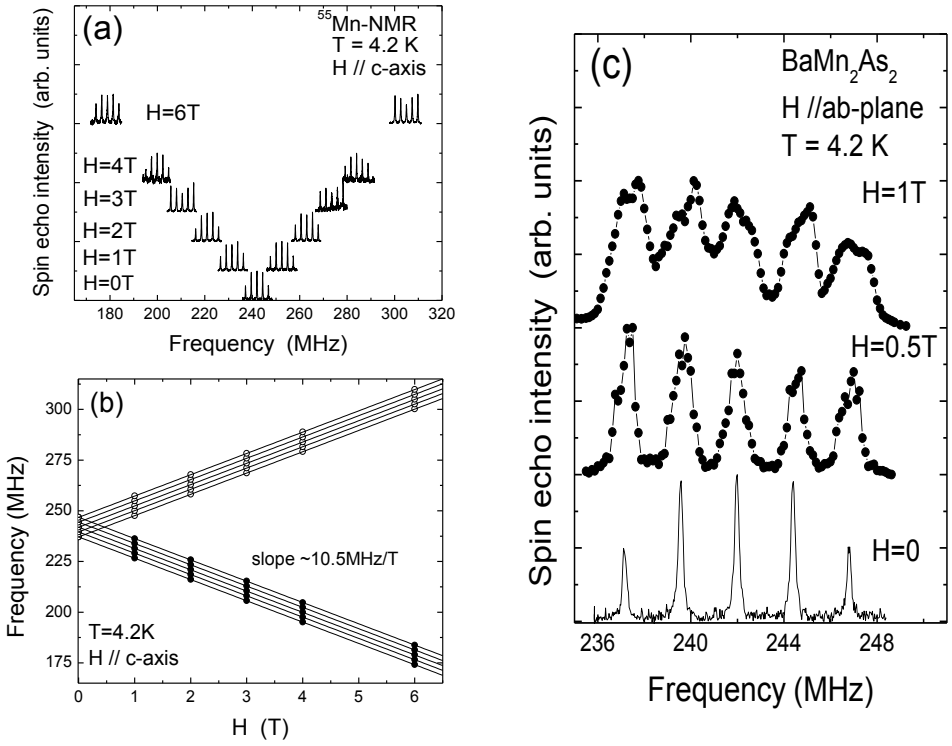

Figure 6.3: Field dependent ^{55}Mn NMR spectra. (a) The five quadrupole spectrum peaks split for external fields applied parallel to the crystallographic c-axis. (b) Field-dependence of the five quadrupole peak positions for applied field parallel to the c-axis. (c) Field-dependent spectra for external field applied parallel to ab-plane shows no shift, but rather a broadening. Field-dependent splitting in (a) and broadening in (c) of the zero-field spectrum supports G-type AMF ordering along the c-axis of $BaMn_2As_2$.

contrast to $H_{app} \parallel c$-axis, no splitting of the ^{55}Mn-NMR spectra is observed, but rather a broadening. In this orientation the applied field is orthogonal to the ordered Mn spin moments and H_{hf}, so $H_{loc} = \sqrt{H_{app}^2 + H_{hf}^2}$. For our applied field range, $H_{hf} \gg H_{app}$, so $H_{loc} \approx H_{hf}$ and any shift in the spectral frequency would be small. Broadening is likely caused by field induced canting of the Mn moments causing an inhomogeneous distribution of H_{loc} at the Mn nuclei. For measurements in higher fields, one would expect further broadening and a quadratic shift of the spectrum towards higher frequencies.

The observed field-dependence for ^{55}Mn-NMR spectra from the K-doped systems was similar to the undoped $BaMn_2As_2$ discussed above. These results support a local-moment

G-type AFM ordering for $BaMn_2As_2$ and $Ba_{1-x}K_xMn_2As_2$ as previously reported.

6.5 ^{75}As-NMR spectrum

A clear quadrupole splitting of the ^{75}As-NMR spectrum is observed for $BaMn_2As_2$ as a function of temperature in Fig. 6.4. The resonance and quadrupole frequencies are approximately T-independent for both field orientations in our observed temperature range. The central transition peak lies just below the reference Larmor field denoted by the vertical dashed line suggesting the average internal field at the As-nuclei is approximately zero. The slightly larger shift observed by the central transition for spectra with $H \parallel ab$-plane, compared to $H \parallel c$-axis, likely results from field-induced canting of the Mn-spin moments in large applied fields, $H \sim 7.5$ T.

Fig. 6.5 shows the ^{75}As spectrum for K-doped for $H \parallel c$-axis. A broadening was observed for all K-concentrations washing out the sharp quadrupole peaks observed in the un-doped system. The broadening increased upon increasing K-concentration x and reduced signal intensity requiring measurements be taken at low temperatures. Despite the broad spectra, the average internal field is approximately zero as observed in the un-doped system.

Consider the high-symmetry position of As, located at the center of a square formed in the ab-plane by four Mn atoms and offset along the c-axis (for further reference see Johnston *et al.*[98]). At the As site for G-type ordering, one would expect a complete cancellation of the fields due to the symmetry of the four n.n. Mn spins. This contrasts with stripe-type ordering, where Mn spin moments order antiferromagnetically along the b-axis and ferromagnetically along the a-axis, in which the As site would experience a net internal field along the b-axis. The lack of any observed internal field from the ^{75}As spectra further supports a local-moment G-type AFM ordering for the parent and K-doped systems.

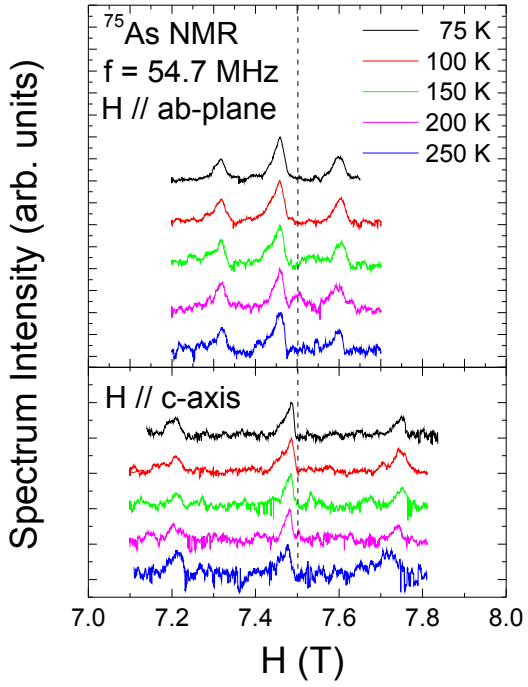

Figure 6.4: (Color online) Three quadrupole split peaks observed for ^{75}As NMR spectra as a function of temperature for fields applied parallel to the ab-plane (top) and c-axis(bottom) for $BaMn_2As_2$. The small shift from the reference Larmor field indicates the average internal hyperfine field from the Mn ions is almost zero. The slightly large shift observed for $H \parallel ab$-plane likely results from field-induced canting of Mn moments ordered antiferromagnetically along the c-axis.

6.6 ^{55}Mn and ^{75}As spin-lattice relaxation

The T-dependencies of the nuclear spin-lattice relaxation rates for ^{55}Mn in zero field and ^{75}As were measured at the central transition peak. The longitudinal nuclear magnetization recoveries following saturation were fit using standard multi-exponential expressions. The recoveries for ^{55}Mn ($I = 5/2$) were fit with the function[105]

$$\frac{M_z(\infty) - M_z(t)}{M_z(\infty)} = \frac{1}{35}\exp\Big(-\frac{t}{T_1}\Big) + \frac{8}{45}\exp\Big(-\frac{6t}{T_1}\Big) + \frac{50}{63}\exp\Big(-\frac{15t}{T_1}\Big), \tag{6.1}$$

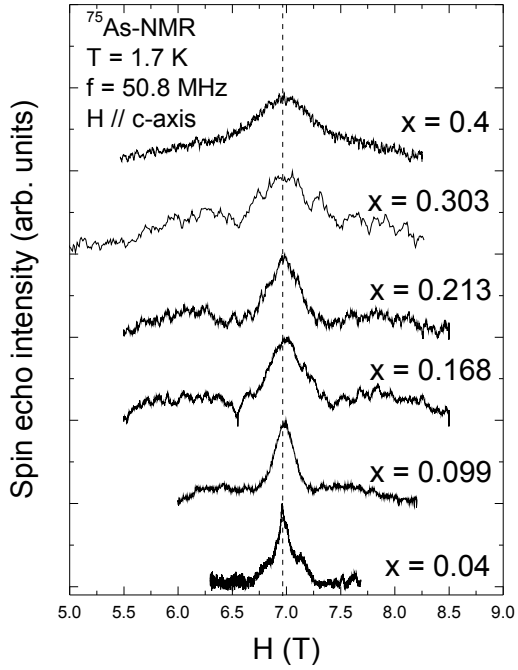

Figure 6.5: ^{75}As NMR spectra with external field parallel to the c-axis for $Ba_{1-x}K_xMn_2As_2$ as a function of K-concentration x.

and ^{75}As ($I = 3/2$) were fit with the function[106]

$$\frac{M_z(\infty) - M_z(t)}{M_z(\infty)} = 0.1 \exp -\frac{t}{T_1} + 0.9 \exp -\frac{6t}{T_1}, \tag{6.2}$$

where $1/T_1$ is the nuclear spin-lattice relaxation rate and $M(t)$ and $M(\infty)$ are the nuclear magnetization after saturation at time t and the nuclear equilibrium magnetization after sufficiently long time $t \to \infty$, respectively.

The T-dependencies of $1/T_1$ for ^{55}Mn in zero field and for ^{75}As in an external field H = 7.5 T are shown in Fig. 6.6(a) and Fig. 6.6(b), respectively. Measurements of $1/T_1$ for ^{75}As were measured with the field applied in both orientations where $H \parallel c$-axis is represented by solid circles and $H \parallel ab$-plane represented by hollow circles in the figure for respective K-concentrations. Maximum temperatures were limited by signal intensity which was reduced due to broadening upon doping for both nuclei.

For the un-doped $BaMn_2As_2$ system, both nuclei observe a $1/T_1 \propto T^n$ dependence

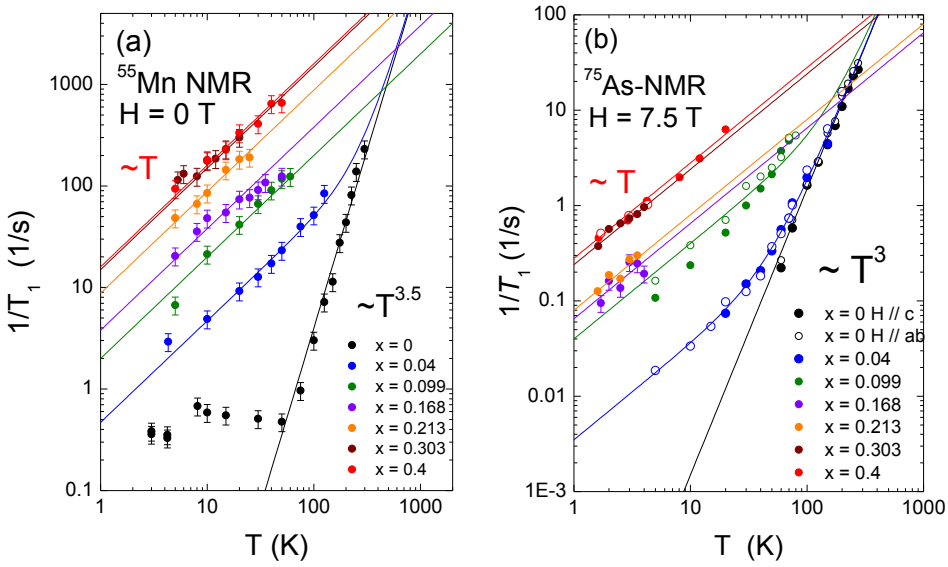

Figure 6.6: (Color online) Temperature-dependent spin-lattice relaxation rate $1/T_1$of $Ba_{1-x}K_xMn_2As_2$ for (a) ^{55}Mn NMR in zero field and (b) ^{75}As NMR for fields parallel to c-axis (solid circles) and parallel to ab-plane (open circles). For both nuclei, a power law behavior for $x = 0$ indicates an insulating ground state while the linear behavior for $x > 0$ indicates a conducting ground state with conduction electrons in the Mn-3d and As-4p bands.

for $T > 40$ K. The deviation from T^n behavior for ^{55}Mn below 40 K is likely due to relaxation associated with defects and/or impurities. For $T > 40$ K, a good fit for ^{55}Mn is given by $1/^{55}T_1 = (4.0 \times 10^{-7} s^{-1} K^{-3.5}) T^{3.5}$ with $n \approx 3.5$ and for ^{75}As by $1/^{75}T_1 = (1.5 \times 10^{-6} s^{-1} K^{-3}) T^3$ with $n \approx 3$. This power law T-dependence for the nuclear relaxation is consistent with a two-magnon Raman process as the main relaxation mechanism for an AFM insulating state when $T \gg \Delta/k_B$, where Δ is the anisotropy gap in the spin wave spectrum.[107]

Upon K-doping, both ^{55}Mn and ^{75}As follow a Korringa relation, $(T_1T)^{-1} =$ constant, offering direct evidence of conduction electrons in the Mn 3d and As 4p bands. This confirms that hole-doping, even at our lowest observed concentration $x = 0.04$, results in a metallic state for $Ba_{1-x}K_xMn_2As_2$. Metallic behavior has been reported for K-

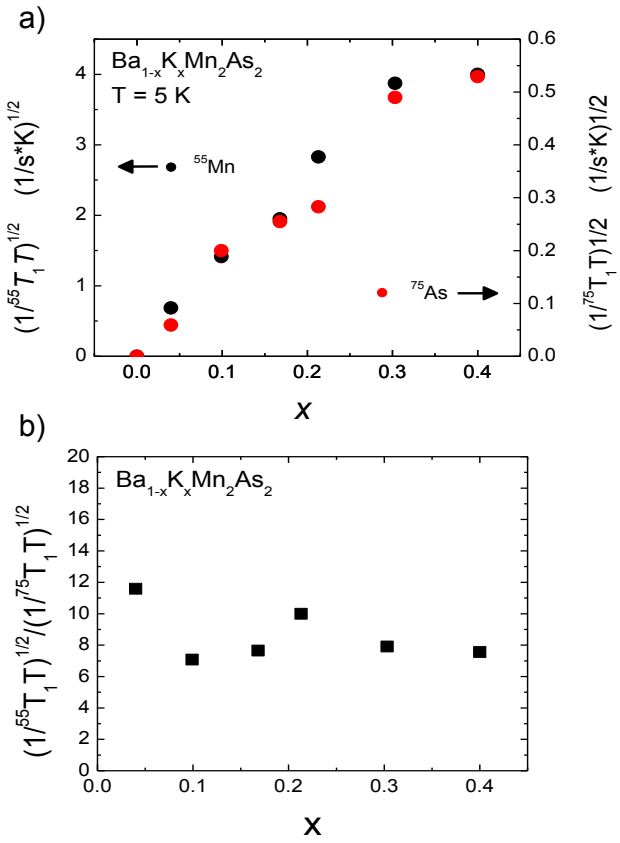

Figure 6.7: (Color online) (a) Plot of $(T_1T)^{-1/2}$ for ^{55}Mn and ^{75}As NMR as determined by the fits in Fig. 6.6 indicating an increase in conduction carriers upon increasing K-concentration x. (b) Plot of the ratio of $(T_1T)^{-1/2}$ for ^{55}Mn and ^{75}As NMR indicating the orbital-decomposed $N(E_F)$ remains constant upon increasing x.

concentration as low as $x = 0.016$.[99] The spin-lattice relaxation rate can be expressed in terms of the density of states as

$$1/T_1 = 4\pi\gamma_e\gamma_n hFA_{hf}^2 N(E_F)^2 T, \tag{6.3}$$

or

$$(1/T_1T)^{1/2} = const * A_{hf}N(E_F). \tag{6.4}$$

where γ_e and γ_n are the gyromagnetic ratios for the electron and the measured nucleus, h is Planck's constant, F is a reduction factor arising from orbital degeneracy, and $N(E_F)$ is the renormalized density of states (DOS) at the Fermi level.[108] Fig. 6.7(a) shows

$(T_1T)^{-1/2}$ for ^{55}Mn and ^{75}As both increase, indicating an increase in DOS and the Mn $3d$ and As $4p$ upon increasing K-concentration x. When plotted as a ratio for ^{55}Mn and ^{75}As,

$$\frac{(1/^{55}T_1T)^{1/2}}{(1/^{75}T_1T)^{1/2}} = \frac{[A_{hf}N(E_F)]_{55}}{[A_{hf}N(E_F)]_{75}} \approx 8, \tag{6.5}$$

suggests the ratio for the orbital-decomposed $N(E_F)$ of Mn $3d$ and As $4p$ is almost constant over our range of K-concentrations.

6.7 Conclusions

In summary, we report ^{55}Mn and ^{75}As NMR results for band-insulating $BaMn_2As_2$ and hole-doped metallic $Ba_{1-x}K_xMn_2As_2$ ($x = 0.04 \rightarrow 0.4$) single crystals. Spectrum measurements confirm similar G-type local-moment AFM structures for all systems despite a transition from an insulating to metallic states upon K-doping. Shifts of the zero-field ^{55}Mn spectra towards lower fields suggests increasing K-concentration x results in a decrease of the local Mn spin moments. The observation of an NMR enhancement effect in zero-field ^{55}Mn spectra for $x \geq 0.213$ supports recent reports of weak ferromagnetic moment, in addition to the confirmed G-type AFM.

Spin-lattice relaxation measurements T_1 for ^{55}Mn and ^{75}As NMR confirm an insulating ground state with $1/T_1 \propto T^n$ for $BaMn_2As_2$ and metallic states which follow a Korringa relation for $Ba_{1-x}K_xMn_2As_2$, evidence of conduction electrons in the Mn $3d$ and As $4p$ bands. While increasing x increases $^{\mathrm{Mn}}N(E_F)$ and $^{\mathrm{As}}N(E_F)$, the ratio $^{\mathrm{Mn}}N(E_F)/^{\mathrm{As}}N(E_F)$ appears to be independent of x suggesting orbitally decomposed Mn-$3d$ and As-$4f$ density of states remain constant for all x. The absence of a structural phase transition in neutron diffraction measurements and no appreciable shift observed in the ^{75}As spectra suggest evidence of a previously unobserved coexistence of AFM ordered Mn spin-moments and weak itinerant ferromagnetism from the Mn $3d$ orbitals.

CHAPTER 7. UPPER-CRITICAL FIELD MEASUREMENTS OF $SrFe_2(As_{1-x}P_x)_2$

7.1 Introduction

Superconductivity in the $AEFe_2As_2$ (AE = Ba, Sr or Ca) family of compounds, frequently referred to as 122 iron pnictides, can be induced in a variety of ways. It can be achieved by hole-doping with alkali A metal substitution of alkali earth metal AE [109–111] as in $(Ba_{1-x}K_x)Fe_2As_2$, transition metal substitution on Fe site as in $AE(Fe_{1-x}TM_x)_2As_2$ [112, 113], or isoelectron substitution on As site as in $AEFe_2(As_{1-x}P_x)_2$ [114–117]. In the rest of this chapter materials will be labeled by the type of AE and dopant elements, such as BaK122, BaTM122, or BaP122.

Approximately the same maximum T_c of about 30 K is achieved for most alkali earth elements and substitutions, which suggests common origin of superconductivity for this class [118–120]. Another unifying feature is universal observation of superconductivity in close proximity to stripe-type antiferromagnetic order, with maximum $T_c(x)$ observed at a doping level close to a critical point where the antiferromagnetic ordering temperature $T_N(x) \to 0$.

Despite this common phenomenology, studies of the normal state resistivity [121–124] and superconducting state properties, see for example [125, 126] for review, revealed unexpected diversity. For example, studies of the superconducting gap structure from penetration depth [126–128], directional heat transport [129], and heat capacity [130–133] as a function of doping suggested full gap at optimal doping universally in BaTM122

and BaK122 [134], evolving towards strongly anisotropic and nodal in the under-doped and overdoped regimes. A similar trend is found in the other families of iron pnictides, e.g. Co- and environmentally doped NaFeAs [135] and Ca10-3-8 [136]. In sharp contrast, the gap is nodal in BaP122 at optimal doping [137], it remains nodal for all compositions, and clear signatures of a quantum critical point can be tracked in the properties of the superconducting condensate [138].

Limited data about the superconducting gap structure available for compounds with other alkali earth metals, different from Ba, suggest that these unique properties of phosphorus doped compositions may be universal, and are at least observed in SrP122 [139, 140]. It is therefore of interest to get a broader insight into the properties of P-doped materials.

The upper critical field of iron pnictides was studied systematically over the phase diagram of BaCo122 [141, 142] and revealed a clear distinction between underdoped and over-doped regimes. This distinction was suggested to be linked with change of the topology of the Fermi surface, however, it can be related to the evolution of the superconducting gap anisotropy in this family as well. Indeed, in stoichiometric iron-pnictide superconductors, full gap LiFeAs [143, 144], and nodal KFe_2As_2 [145–150], studies of the upper critical fields [2, 3, 151, 152] reveal significantly different temperature dependences. Relatively little is known about $H_{c2}(T)$ of P-doped materials in which measurements so far were limited to a temperature range close to zero-field T_c [153–155], and in view of suggested nodal gap structure it is of interest to get insight into the temperature dependent upper critical field of this system.

This work we reported measurements of the anisotropic upper critical field in single crystals of optimally doped SrP122, $x = 0.35$, using the pulsed magnetic field facility at Los Alamos National High Magnetic Field Laboratory [156]. We find a clear difference between the temperature-dependent H_{c2} for fields along and transverse to the tetragonal c-axis. The dependence for $H \parallel c$ is close to T-linear, which is very similar to the

behavior found in previous studies on nodal KFe_2As_2 [3], but very dissimilar with that of full-gap LiFeAs [2]. In addition, we find monotonic suppression of T_c, $H_{c2,a}$ and $H_{c2,c}$ with heavy-ion irradiation.

7.2 Experimental details

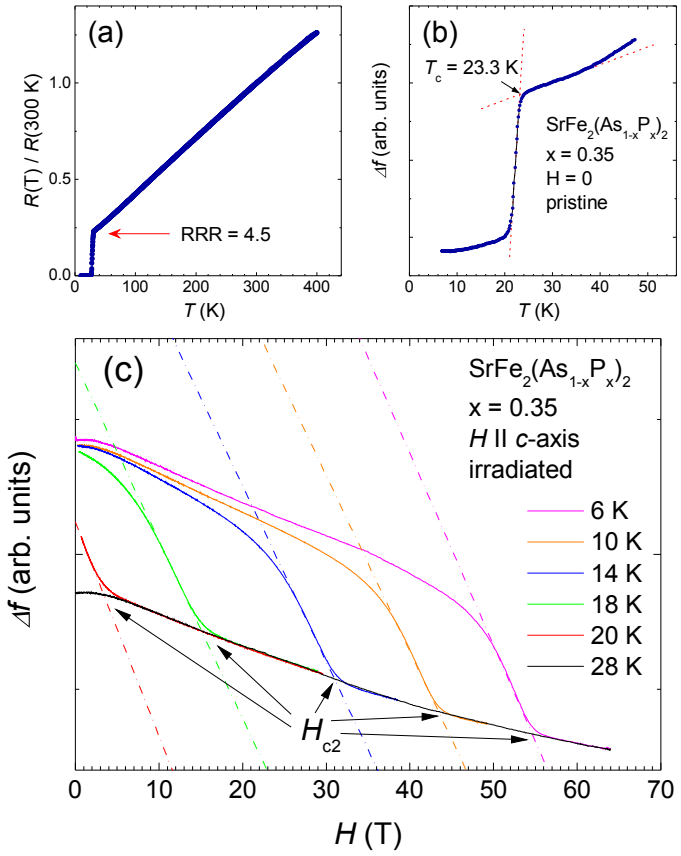

Figure 7.1: (Color online) (a) Temperature dependent in-plane resistivity of the representative sample of pristine $SrFe_2(As_{1-x}P_x)_2$, $x = 0.35$. Close to perfect T-linear dependence is observed in the temperature range from T_c up to 400 K. Resistive transition ends at ~ 25 K, close to the magnetic transition observed in zero-field TDR measurements (b). The bottom panel (c) shows TDR frequency shift (in arbitrary units) measured as a function of magnetic field during pulsed field experiments at indicated temperatures. The lines show the way the H_{c2} was defined from the data as a cross-over point of linear extrapolation of the rapid frequency drop to the level of the background signal.

Single-crystalline samples of $SrFe_2(As_{1-x}P_x)_2$ were grown using the self-flux method.Typically samples had a shape of irregular platelets, with in-plane dimensions (0.3-1)*(0.3-1) mm^2

and thickness 0.02 to 0.1 mm. A sample composition of x=0.35 was determined using EDX analysis. For our study we used several samples from the same batch. Four Sn-soldered contacts [157] were attached to one of the samples to measure in-plane resistivity, plotted using normalized $\rho(T)/\rho(300K)$ in Fig. 7.1(a). The value of $\rho(300K)$ was about 300 $\mu\Omega \cdot cm$, close to a value found in BaP122. [158]. Samples show very close to perfect T-linear temperature dependence, which is similar to the dependence found in BaP122 at optimal doping, both for in-plane [137] and inter-plane [158] transport. The resistive transition is rather sharp, $\Delta T_c \sim 2$ K, and its end point at 25 K is close to an onset of a sharp frequency shift in zero-field TDR experiments.

For this study we used two small single crystals from the same batch. One sample was irradiated with 1.4 GeV $^{208}Pb^{56+}$ ions at the Argonne Tandem Linear Accelerator System (ATLAS) with ion flux of 5x10^{11} ions·s^{-1}·m^{-2}. The thickness of this sample of approximately 20 μm was much smaller than stopping distance of the ions, ≈ 60 μm, thus allowing creation of columnar defects. Assuming that each defect acts as a pinning center for one magnetic flux quantum, this irradiation corresponds to a matching magnetic field of approximately 25 T, corresponding to a dose of 12x10^{12} ions·m^{-2}.

Zero-field measurements on the samples used in pulsed field studies at NHMFL were performed in a separate TDR setup in Ames laboratory. A typical temperature-scan for pristine sample of SrP122 is shown in Fig. 7.1(b). Onset of superconductivity at T_c = 25 K provides a clear change of the TDR frequency. Similar frequency variations are found in isothermal pulsed magnetic field sweeps, as shown in Fig. 7.1(c).

During pulsed field experiments samples were glued with GE varnish to a pancake coil for the TDR setup. The whole assembly was aligned under the microscope with respect to sample holder, providing the accuracy within 2° with respect to the principal crystallographic directions.

7.3 Results and discussion

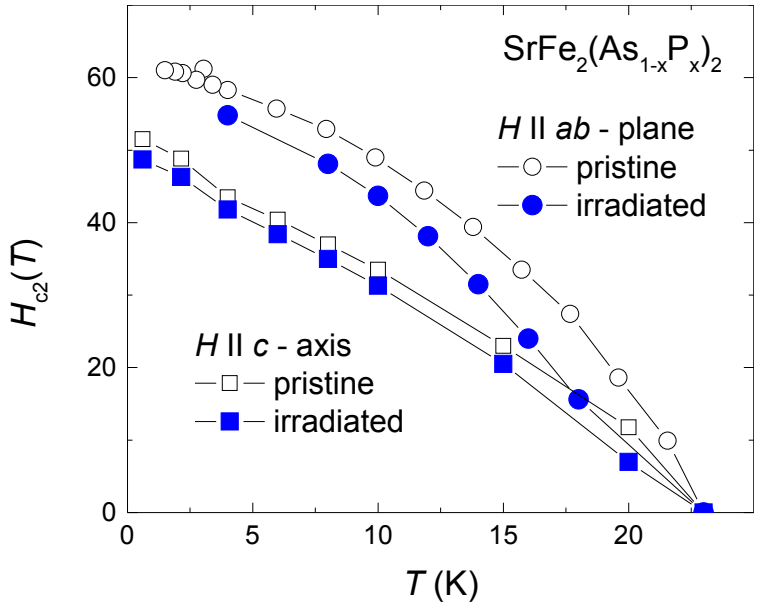

Figure 7.2: (Color online) The temperature dependent upper critical fields for pristine (black open symbols) and irradiated (closed blue symbols) samples of optimally doped $SrFe_2(As_{1-x}P_x)_2$ with $x = 0.35$, as determined from pulsed field measurements in magnetic fields parallel to the c-axis (squares) and to the conducting $ab-$plane (circles). The lines connect data points and do not show true position of zero-field T_c, determined in separate experiments.

In Fig. 7.2 we plot $H_{c2}(T)$ as determined from pulsed field TDR measurements at different temperatures for pristine and irradiated samples. Note, that zero-field T_c was determined in a separate experiment, so that the $H_{c2}(T)$ behavior close to zero field $T_c(H = 0)$ is not well defined. Several features of the data should be mentioned. The data for magnetic fields perpendicular to the plane field orientation, $H_{c2,c}(T)$, in general follow a T-linear dependence. The data for magnetic fields parallel to the plane, $H_{c2,a}$(T), show a clear tendency for saturation approaching $T = 0$, which is a common expectation for both orbital [159] and paramagnetic [160] limiting mechanisms of the upper critical field.

In Fig. 7.3 we plot the temperature-dependent anisotropy parameter, $\gamma \equiv H_{c2,a}/H_{c2,c}$, for pristine and irradiated samples of SrP122. As is common for iron-arsenide supercon-

ductors, the anisotropy parameter is strongly temperature dependent. In most of the iron-arsenides the anisotropy parameter monotonically decreases upon cooling [161–163]. Taken in conjunction with flattening of $H_{c2,a}(T)$, this fact is frequently discussed as a signature of paramagnetic effects in magnetic fields parallel to the plane [160]. Alternatively, the same feature of monotonically decreasing upon cooling $\gamma(T)$ is explained as a consequence of strong multi-band effects in iron pnictides [162].

For the description of the upper critical field in SrP122, it is important to understand the superconducting gap structure of this material. Although the detailed measurements as a function of doping were not performed yet, the available NMR [139], microwave [140], and radio-frequency London penetration depth measurements suggest that the superconducting gap of optimally doped SrP122 is nodal.

The effect of the nodal gap structure on the temperature and angular dependence of the upper critical field is a long standing problem in the field of unconventional superconductivity, stemming back to the early 80's [164]. While these effects in multi-band superconductors may be far too complicated [162], we decided to take a purely empirical approach and compare the temperature dependent H_{c2} for various iron-based materials. Stoichiometric superconductors provide a good reference point. There is ample evidence that the superconducting gap of LiFeAs, believed to be representative of slightly overdoped regime [165], is full and practically isotropic with only minor multi-band effects [143, 144]. The superconducting gap of KFe_2As_2 is nodal, as suggested by a plethora of various experiments, although the exact origin (accidental $S^{\pm}$ or symmetry imposed d-wave) and location of the nodes is heavily debated [149, 150].

In Fig. 7.4 we compare the $H_{c2}(T)$ curves for two principal directions of the applied magnetic field in SrP122 with those for LiFeAs and KFe_2As_2. One feature of the data is obvious. While the $H_{c2,c}(T)$ flattens in LiFeAs, as expected for s-wave superconductors in Werthamer-Helfand-Hohenberg (WHH) theory [159], the dependence is roughly linear in SrP122 and KFe_2As_2, - the materials with the nodal superconducting gap. The behavior

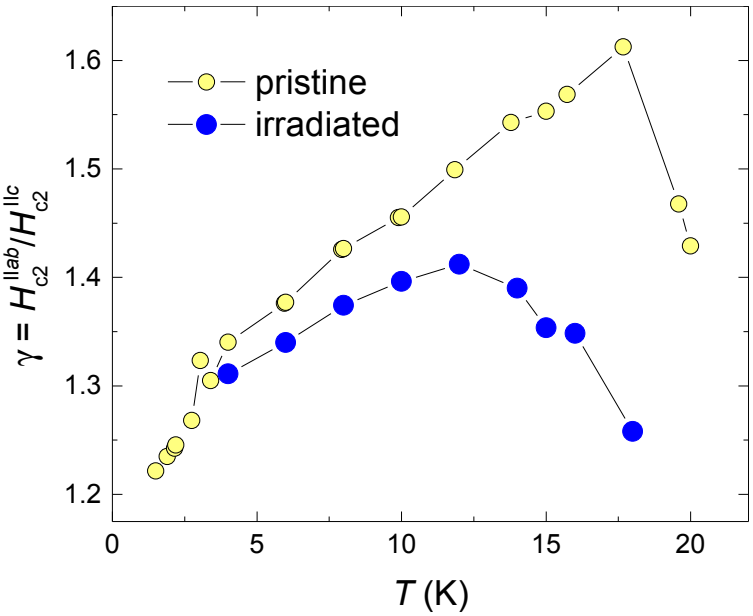

Figure 7.3: (Color online) The temperature-dependent anisotropy parameter $\gamma(T) \equiv H_{c2,a}(T)/H_{c2,c}(T)$ in pristine (open circles) and irradiated (closed circles) samples of $SrFe_2(As_{1-x}P_x)_2$, $x = 0.35$.

in magnetic field parallel to the plane is not as different, with all compounds showing clear signatures of saturation on approaching $T = 0$.

In Fig. 7.5 we compare the temperature-dependent anisotropy parameter, $\gamma(T)$, of pristine samples of optimally doped SrP122 with $\gamma(T/T_c)/\gamma(0)$ in nodal KFe_2As_2 and full-gap LiFeAs. Reflecting mainly the difference in the behavior of $H_{c2,c}(T)$, the behavior of $\gamma(T)$ is dramatically different for nodeless and nodal materials.

While the saturation of $H_{c,a2}(T)$ on approaching T=0 in magnetic field parallel to Fe-As planes is in line with the predictions of both orbital and paramagnetic mechanisms of $H_{c2,a}(T)$ [159, 160], a near T-linear dependence for $H \parallel c$ is quite exotic, and its origin is not well understood. Several experimental studies reported nearly T-linear $H_{c2,c}(T)$. Nearly straight $H_{c2,c}(T)$ for $H \parallel c$ was observed in MgB2 [166] and was explained in the orbital-limiting model for two-band superconductivity in the dirty limit. If the two bands are characterized by the equal diffusivities $D_1 = D_2$, the $H_{c2}(T)$ follows WHH type dependence [159], however, if the diffusivity in a weaker band D_2 is much smaller

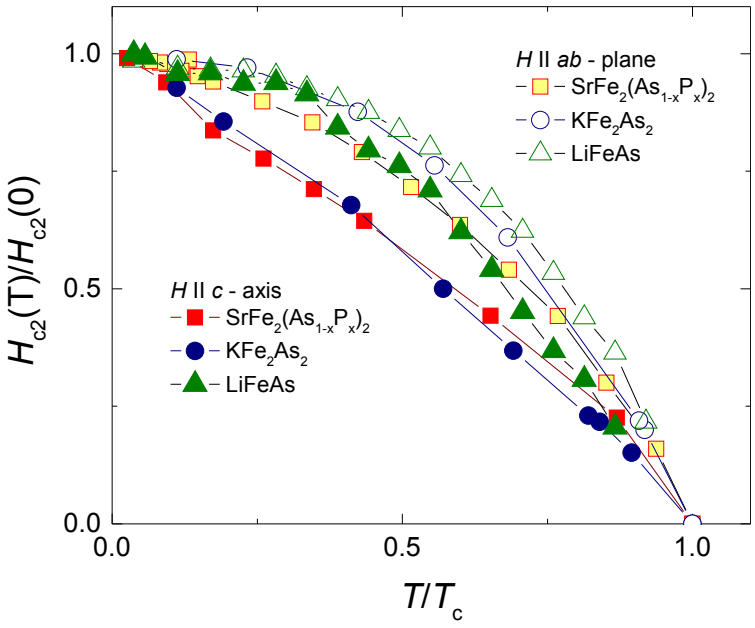

Figure 7.4: (Color online) The $H-T$ phase diagram of $SrFe_2(As_{1-x}P_x)_2$, $x = 0.35$ (red). Normalized $H/H_{c2}(0)$ is plotted vs. normalized temperature, $T/T_c(0)$. Solid symbols show $H_{c2} \parallel c-$axis and open symbols show $H_{c2} \parallel ab-$plane. For reference we show similar plots for full-gap superconductor LiFeAs (green up-triangles) [2], and nodal KFe_2As_2 (blue circles) [3].

than the diffusivity D_1 in a stronger band, $H_{c2}(T)$ has upward curvature. Thus, there is a ratio D_2/D_1 at which H_{c2}(T) becomes nearly straight. Similarly, near T-linear $H_{c2}(T)$ was observed in doped iron-based superconductors, BaCo122 [167], BaK122, and FeSeTe [168]. However, due to very high values of $H_{c2}(0)$ it is not clear whether this linear behavior will change to a saturation at the lowest temperatures. In all these materials the linear $T-$dependence was explained in a similar multi-band scenario in the dirty limit, as in MgB_2, but the question of whether the dirty limit is achieved is still open [163]. The $T-$linear dependence of H_{c2} was found in other superconductors. In KOs_2O_6 it was explained in terms of orbital limiting mechanism, due to missing spatial inversion symmetry [169]. In organic superconductor κ-(BEDT-TTF)$_2$Cu[N(CN)$_2$]Br, T-linear dependence was found in magnetic fields parallel to the two-dimensional plane [170, 171]. Interestingly, here the behavior at ambient pressure closely follows a square root dependence as expected for paramagnetic Pauli limiting [172], while with pressure this

dependence becomes close to T-linear [170, 171]. A similar trend is found in other organic superconductors [173], and possible relation of T-linear dependence to the formation of inhomogeneous Fulde-Ferelle-Larkin-Ovchinnikov state [174] was suggested by the experiments on samples with varying disorder [175].

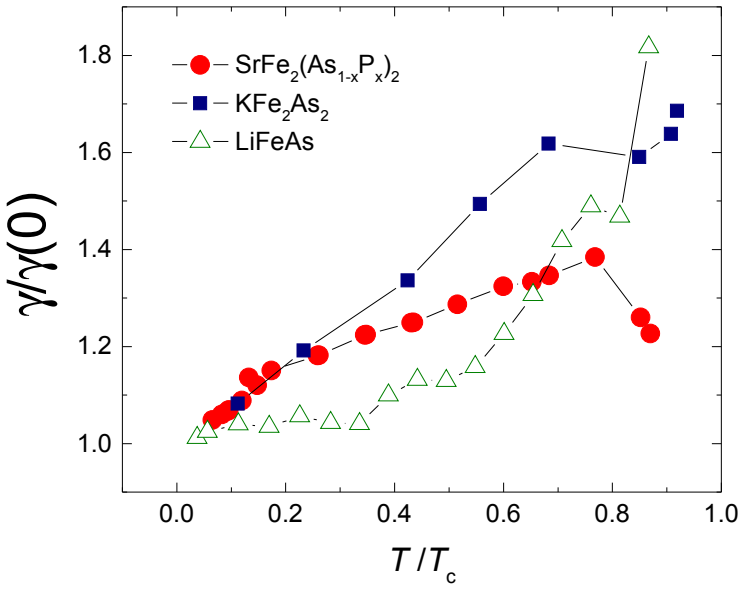

Figure 7.5: (Color online) The temperature-dependent anisotropy parameter $\gamma(T) \equiv H_{c2,a}(T)/H_{c2,c}(T)$ normalized to its value at $T = 0$ in pristine $SrFe_2(As_{1-x}P_x)_2$, $x = 0.35$ (filled red circles). For the reference we show $\gamma(T/T_c)/\gamma(0)$ in clean iron-pnictide superconductors, - nodal KFe_2As_2 (blue squares) [3], and full-gap LiFeAs (green triangles) [2].

7.4 Conclusions

In summary, using pulsed field tunnel-diode resonator (TDR) measurements, we have determined the upper critical fields along two principal crystallographic directions in single crystals of isoelectron-substituted $SrFe_2(As_{1-x}P_x)_2$ at optimal doping, $x = 0.35$. We found that the shape of $H_{c2}(T)$ curves is different for the fields perpendicular and parallel to the tetragonal $c-$axis. It shows WHH-like behavior with clear saturation as $T \to 0$ for $H \parallel ab-$plane and practically T-linear variation for $H \parallel$ c-axis. We show that the shape of the $H_{c2}(T)$ curves is not affected much by heavy ion irradiation, which

suppresses T_c and $H_{c2}(0)$ by the same amount. We do not see any special features in the $H_{c2,c}(T)$ line, corresponding to a matching field of 25 T in heavy-ion irradiated samples. The temperature dependence of H_{c2} for two principal directions in $SrFe_2(As_{1-x}P_x)_2$ is similar to that found in a nodal superconductor KFe_2As_2 [3], but is different from that of fully gapped LiFeAs[2]. This similarity may be suggestive that the anomalous linear shape of $H_{c2,c}(T)$ in iron pnictides may be related to a nodal superconducting gap.

CHAPTER 8. CONCLUSIONS

This thesis focused on the use of radio-frequency techniques to investigate the static and dynamic properties of novel magnetic and superconducting materials. A tunnel-diode resonator is capable of highly precise measurements of the bulk dynamic magnetic susceptibility, dM/dH. This work has demonstrated the effectiveness of using TDR in pulsed magnetic fields for investigating the quantum energy levels of antiferromagnetically correlated magnetic molecules $Cr_{12}Cu_2$ and $Cr_{12}Ln_4$, and the anisotropic upper-critical fields of the P-doped SrP122 superconductor. Nuclear magnetic resonance is a powerful technique for obtaining a vast range of physical information by investigating local static and dynamic magnetic properties via hyperfine interactions with high resolution. NMR spectrum and spin-lattice relaxation measurements illustrate an inhomogeneous magnetic environment for the 30 V^{4+} ions in $W_{72}V_{30}$, revealing a critical slowing down of the spin dynamics at low temperatures. In $Ba_{1-x}K_xMn_2As_2$, NMR spectra measurements are capable of determining the nature of the local AFM environment while spin-lattice relaxation measurements characterize the conducting and insulating electronic properties.

The work presented on $Cr_{12}Cu_2$ in Ch. 3 successfully demonstrates the first implementation of TDR for detecting quantum spin transitions of magnetic molecules in pulsed magnetic fields. TDR demonstrates the ability to detect, not only transitions between H-dependent magnetic ground states, but also transitions involving excited energy levels which cannot be observed in conventional static magnetometry methods employed in pulsed magnetic fields (see Fig. 3.3 and Fig. 3.4). In order to observe the excited

level crossings, there must exist some weak anisotropic contribution to the spin Hamiltonian introducing a small energy gap, δ, in the form of an avoided level crossing. If the thermal energy is sufficiently high as to allow significant population of excited energy levels, then these otherwise forbidden energy level crossings are observed if the TDR frequency is sufficiently large compared to the energy gap, $\hbar\omega \geq \delta$. Previous theoretical worked achieved a theoretical description used QMC with a purely isotropic Heisenberg Hamiltonian to characterize the weak-field susceptibility. The system was well described by three exchange constants which were then used to calculate the low-temperature differential susceptibility versus magnetic field. Experimental results were compared with these QMC calculations showing excellent agreement for the field values of the energy level crossings. Therefore, this work determines that TDR, in conjunction with QMC,is a successful and unique tool for investigating the spectra of low lying energy levels in AFM magnetic molecules.

Studies in Ch. 4 of the family of AFM magnetic molecules $Cr_{12}Ln_4$ use DC SQUID magnetometry and TDR measurements of the dynamic susceptibility in pulsed fields to study $3d$-$4f$ interactions in finite-sized spin clusters. DC susceptibility measurements indicate AFM ordering for Cr ions in the $\{Cr_6\}_2$ horseshoes, and for systems containing non magnetic Ln ions Y and Eu, with an $S = 0$ ground state. Systems containing magnetic Ln ions (Gd, Tb, Dy, Ho, Er, Yb), on the other hand, show a large contribution from the $4f$ moments. Curie-Weiss fits for the low temperature susceptibility suggest the onset of weak antiferromagnetic interactions at low temperatures, a surprising result as many Gd-transition metal interactions are ferromagnetic as a result of a charge transfer mechanism. While DC measurements of χT were unable to definitively determine a $S = 0$ ground state, leaving open the possibility of high spin ground states despite the apparent AFM interaction for systems with magnetic Ln ions.

Plots of the DC magnetization $M(H)$ at $T = 2$ K were used to determine the values of $g_J J$ for systems containing magnetic Ln ions. For the Gd sample, with quenched

orbital angular momentum $L = 0$, the Gd ions act as model Heisenberg moment in good agreement with theoretical calculations. Results for systems with Ln ions where $L \neq 0$ suggest a large anisotropy arising from the orbital angular momentum, reduces the magnitude of the local moment to approximately half the free ion value, independent of g_J, S, L, and J.

The TDR measurements for dM/dH in pulsed fields show a rich spectrum of ground state and excited state level crossing transitions. The addition of Ln ions appears to act as a perturbation to the Cr horseshoes shifting the transitions to higher fields, without dramatically altering the quantum energy levels. The Gd sample demonstrates a double feature for ground state and excited state transitions and it is not clear at this time whether this result is an effect of the quenched orbital angular momentum. Further, the observation of a large peak at low field for the Tb sample is likely the result of a quantum spin transition arising from Tb-Cr interactions.

Attempts to were made to characterize dM/dH for the Cr horseshoe and $Cr_{12}Y_4$ by characterizing the DC susceptibility with an isotropic Hamiltonian. While the exchange parameters were adjusted to obtain good fits for χ, but only fits for the Y sample demonstrated good agreement in dM/dH with the TDR data. A better fit of dM/dH for the Cr horseshoe might be attainable using a third exchange constant. However, we note that since $\chi(T)$ provides a probe of the complete energy spectrum, it is possible another set of exchange values could also reproduce $\chi(T)$ and better characterize experimental observations. This argument can be justified as two different sets of exchange constants accurately reproduce the weak-field susceptibility for $Cr_{10}Cu_2$ slightly altering the field dependence of the ground state level crossings.

Investigations of the low temperature magnetization, magnetic susceptibility, proton and vanadium NMR, and theoretical studies presented in Ch. 5 were conducted to investigate the magnetic properties and spin dynamics of the geometrically frustrated magnetic molecule $W_{72}V_{30}$, and finite representation of the 2-dimensional kagomé lattice.

The most striking experimental finding is that the field-dependent magnetization at 0.5 K, as obtained using a pulsed magnetic field, increases monotonically up to 50 T without showing any sign of staircase behavior in contrast to predictions based on single value nearest-neighbor exchange coupling. Further, we find that a single-J model fails to describe the temperature dependence of the intrinsic weak-field magnetic susceptibility χ_0 below 15 K, as obtained from SQUID measurements. However, both sets of experimental observations are reproduced to reasonable accuracy upon introducing a model based on a broad distribution of values of the nearest-neighbor coupling.

^{1}H-NMR and ^{51}V-NMR measurements were conducted to investigate the local magnetic properties. We find the temperature dependence of χ_0 estimated from the proton NMR spectrum is in satisfactory agreement with SQUID measurements. A high degree of inhomogeneity of the local environment of V ions is suggested by the observation of a wide distribution of quadrupole frequencies, as well as the temperature dependence of the observed line width and NMR shift for ^{51}V-NMR spectrum measurements. This characteristic of the local environment is consistent with a large distribution of J-values indicated by the theoretical studies. T_1 measurements of both ^{1}H and ^{51}V reveal the existence of slow spin dynamics at low temperatures. In particular, the fluctuation frequency of the interacting system of V^{4+} spins is found to show a power law behavior, of the form $T^{3.5}$ at temperatures below 30 K, i.e., the same behavior that has been found for many antiferromagnetic rings and clusters of spins $s > 1/2$ [90, 93]. The need for a multi-J model as suggested by experimental and theoretical studies might be correlated to the presence of significant local distortions of the spherical shape of the $W_{72}V_{30}$ molecules at low temperatures which could be tested by low-temperature X-ray diffraction measurements.

Ch. 6 presents ^{55}Mn and ^{75}As NMR spectra and spin-lattice relaxation studies to investigate the local magnetic and electronic properties for band-insulating $BaMn_2As_2$ and hole-doped metallic $Ba_{1-x}K_xMn_2As_2$ ($x = 0.04 \rightarrow 0.4$) single crystals. Spectrum

measurements confirm all systems possess similar G-type local-moment AFM structures despite a transition from insulating to metallic states. Shifts of the zero-field ^{55}Mn spectra towards lower fields suggests increasing K-concentration x results in a decrease of the local Mn spin moments. The observation of an NMR enhancement effect in zero-field ^{55}Mn spectra for $x \geq 0.213$ supports recent reports of weak ferromagnetic moment, in addition to the confirmed G-type AFM.

Spin-lattice relaxation measurements T_1 for ^{55}Mn and ^{75}As NMR confirm an insulating ground state with $1/T_1 \propto T^n$ for $BaMn_2As_2$ and metallic states which follow a Korringa relation for $Ba_{1-x}K_xMn_2As_2$, evidence of conduction electrons in the Mn $3d$ and As $4p$ bands. While increasing x increases $^{\mathrm{Mn}}N(E_F)$ and $^{\mathrm{As}}N(E_F)$, the ratio $^{\mathrm{Mn}}N(E_F)/^{\mathrm{As}}N(E_F)$ appears to be independent of x suggesting orbitally decomposed Mn-$3d$ and As-$4f$ density of states remain constant for all x. The absence of a structural phase transition in neutron diffraction measurements and no appreciable shift observed in the ^{75}As spectra suggest evidence for a previously unseen coexistence of AFM ordered Mn spin-moments and weak itinerant ferromagnetism from the Mn $3d$ orbitals.

In Ch. 7, pulsed field tunnel-diode resonator (TDR) measurements determined the upper critical fields along two principal crystallographic directions in single crystals of isoelectron-substituted $SrFe_2(As_{1-x}P_x)_2$ at optimal doping, $x = 0.35$. The shape of the $H_{c2}(T)$ curves demonstrate an anisotropy for fields perpendicular and parallel to the tetragonal $c-$axis showing WHH-like behavior with clear saturation as $T \to 0$ for $H \parallel ab-$plane and practically T-linear variation for $H \parallel$ c-axis. It is shown that the shape of the $H_{c2}(T)$ curves is not affected by heavy ion irradiation, which suppresses T_c and $H_{c2}(0)$ by the same amount. We do not see any special features in the $H_{c2,c}(T)$ line, corresponding to a matching field of 25 T in heavy-ion irradiated samples. The temperature dependence of H_{c2} in $SrFe_2(As_{1-x}P_x)_2$ is similar to that found in a nodal superconductor KFe_2As_2 [3], but different from that of fully gapped LiFeAs[2]. This similarity may be suggestive that the anomalous linear shape of $H_{c2,c}(T)$ in iron pnictides

may be related to a nodal superconducting gap.

In conclusion, this thesis demonstrates the diversity of physical systems where RF techniques are effective tools for studying magnetic and superconducting properties. The utility of TDR has grown over recent years to explore more materials and effects and is well suited for detecting quantum spin transitions and phase transitions. Meanwhile, NMR is an already well understood method exploited across a diverse span of scientific disciplines. In the physical sciences, these powerful techniques will continue to develop in order to discover new and exciting physics.

BIBLIOGRAPHY

[1] M. D. Vannette, Ph.D. thesis, Iowa State University (2008).

[2] K. Cho, H. Kim, M. A. Tanatar, Y. J. Song, Y. S. Kwon, W. A. Coniglio, C. C. Agosta, A. Gurevich, and R. Prozorov, Phys. Rev. B **83**, 060502 (2011), URL http://link.aps.org/doi/10.1103/PhysRevB.83.060502.

[3] T. Terashima, M. Kimata, H. Satsukawa, A. Harada, K. Hazama, S. Uji, H. Harima, G.-F. Chen, J.-L. Luo, and N.-L. Wang, Journal of the Physical Society of Japan **78**, 063702 (2009), URL http://jpsj.ipap.jp/link?JPSJ/78/063702/.

[4] O. Kahn, *Molecular Magnetism* (VCH Publishers, New York, 1993).

[5] A. Mller, F. Peters, M. T. Pope, and D. Gatteschi, Chemical Reviews **98**, 239 (1998), http://pubs.acs.org/doi/pdf/10.1021/cr9603946, URL http://pubs.acs.org/doi/abs/10.1021/cr9603946.

[6] Y.-Z. Zheng, M. Evangelisti, and R. E. P. Winpenny, Chem. Sci. **2**, 99 (2011), URL http://dx.doi.org/10.1039/C0SC00371A.

[7] T. C. Stamatatos, K. A. Abboud, W. Wernsdorfer, and G. Christou, Polyhedron **26**, 2095 (2007), ISSN 0277-5387, URL http://www.sciencedirect.com/science/article/pii/S0277538706005808.

[8] M. Leuenberger, Nature **410**, 789 (2001).

[9] X. Wang, Phys. Rev. A **66**, 034302 (2002), URL http://link.aps.org/doi/10.1103/PhysRevA.66.034302.

[10] E. Morosan, S. Budko, P. Canfield, M. Torikachvili, and A. Lacerda, Journal of Magnetism and Magnetic Materials **277**, 298 (2004), ISSN 0304-8853, URL http://www.sciencedirect.com/science/article/pii/S0304885303009260.

[11] A. S. Sefat, S. L. Budko, and P. C. Canfield, Journal of Magnetism and Magnetic Materials **320**, 120 (2008), ISSN 0304-8853, URL http://www.sciencedirect.com/science/article/pii/S0304885307006877.

[12] K. Myers, S. Bud'ko, I. Fisher, Z. Islam, H. Kleinke, A. Lacerda, and P. Canfield, Journal of Magnetism and Magnetic Materials **205**, 27 (1999), ISSN 0304-8853, URL http://www.sciencedirect.com/science/article/pii/S0304885399004722.

[13] S. Bud'ko, Z. Islam, T. Wiener, I. Fisher, A. Lacerda, and P. Canfield, Journal of Magnetism and Magnetic Materials **205**, 53 (1999), ISSN 0304-8853, URL http://www.sciencedirect.com/science/article/pii/S0304885399004862.

[14] I. R. Fisher, K. O. Cheon, A. F. Panchula, P. C. Canfield, M. Chernikov, H. R. Ott, and K. Dennis, Phys. Rev. B **59**, 308 (1999), URL http://link.aps.org/doi/10.1103/PhysRevB.59.308.

[15] J. L. Atwood, Nature Materials **1**, 91 (2002).

[16] P. Sindzingre, G. Misguich, C. Lhuillier, B. Bernu, L. Pierre, C. Waldtmann, and H.-U. Everts, Phys. Rev. Lett. **84**, 2953 (2000), URL http://link.aps.org/doi/10.1103/PhysRevLett.84.2953.

[17] J. Jaklič and P. Prelovšek, Phys. Rev. B **49**, 5065 (1994), URL http://link.aps.org/doi/10.1103/PhysRevB.49.5065.

[18] J. Schnack and O. Wendland, The European Physical Journal B **78**, 535 (2010), ISSN 1434-6028, URL http://dx.doi.org/10.1140/epjb/e2010-10713-8.

[19] C. T. VanDegrift, Ph.D. thesis, University of California, Irvine (1975).

[20] A. Abragam, *Principles of Nuclear Magnetism* (Clarendon Press, Oxford, 1961).

[21] C. Slichter, *Principles of Magnetic Resonance* (Springer-Verlag, Berlin, 1990).

[22] J. Aslam and W. Weyhmann, Review of Scientific Instruments **44**, 71 (1973), URL http://link.aip.org/link/?RSI/44/71/1.

[23] B. V. Riet and L. V. Gerven, Journal of Physics E: Scientific Instruments **15**, 558 (1982), URL http://stacks.iop.org/0022-3735/15/i=5/a=019.

[24] R. B. Clover and W. P. Wolf, Review of Scientific Instruments **41**, 617 (1970), URL http://link.aip.org/link/?RSI/41/617/1.

[25] F. Habbal, G. E. Watson, and P. R. Elliston, Review of Scientific Instruments **46**, 192 (1975), URL http://link.aip.org/link/?RSI/46/192/1.

[26] J. N. Fox and J. U. Trefny, American Journal of Physics **43**, 622 (1975), URL http://link.aip.org/link/?AJP/43/622/1.

[27] C. T. V. Degrift, Review of Scientific Instruments **46**, 599 (1975), URL http://link.aip.org/link/?RSI/46/599/1.

[28] R. Kubo, Journal of the Physical Society of Japan **12**, 570 (1957), URL http://jpsj.ipap.jp/link?JPSJ/12/570/.

[29] K. Saito, S. Miyashita, and H. De Raedt, Phys. Rev. B **60**, 14553 (1999), URL http://link.aps.org/doi/10.1103/PhysRevB.60.14553.

[30] E. L. Hahn, Phys. Rev. **80**, 580 (1950), URL http://link.aps.org/doi/10.1103/PhysRev.80.580.

[31] C. Martin, L. Engelhardt, M. L. Baker, G. A. Timco, F. Tuna, R. E. P. Winpenny, P. L. W. Tregenna-Piggott, M. Luban, and R. Prozorov, Phys. Rev. B **80**, 100407 (2009), URL http://link.aps.org/doi/10.1103/PhysRevB.80.100407.

[32] L. Engelhardt, C. Muryn, R. Pritchard, G. Timco, F. Tuna, and R. Winpenny, Angewandte Chemie International Edition **47**, 924 (2008), ISSN 1521-3773, URL http://dx.doi.org/10.1002/anie.200704132.

[33] O. F. Syljuåsen and A. W. Sandvik, Phys. Rev. E **66**, 046701 (2002), URL http://link.aps.org/doi/10.1103/PhysRevE.66.046701.

[34] S. R. White, Phys. Rev. B **48**, 10345 (1993), URL http://link.aps.org/doi/10.1103/PhysRevB.48.10345.

[35] U. Schollwöck, Rev. Mod. Phys. **77**, 259 (2005), URL http://link.aps.org/doi/10.1103/RevModPhys.77.259.

[36] C. Benelli and D. Gatteschi, Chemical Reviews **102** (2002), http://pubs.acs.org/doi/pdf/10.1021/cr010303r, URL http://pubs.acs.org/doi/abs/10.1021/cr010303r.

[37] N. D. M. N. W. Ashcroft, *Solid State Physics* (W. B. Saunders, 1976).

[38] C. Kittel, *Introduction to Solid State Physics* (Wiley, 1996).

[39] A. McRobbie, A. R. Sarwar, S. Yeninas, H. Nowell, M. L. Baker, D. Allan, M. Luban, C. A. Muryn, R. G. Pritchard, R. Prozorov, et al., Chem. Commun. **47**, 6251 (2011), URL http://dx.doi.org/10.1039/C1CC11516B.

[40] N. Hoshino, M. Nakano, H. Nojiri, W. Wernsdorfer, and H. Oshio, Journal of the American Chemical Society **131**, 15100 (2009), pMID: 19803515, http://pubs.acs.org/doi/pdf/10.1021/ja9066496, URL http://pubs.acs.org/doi/abs/10.1021/ja9066496.

[41] E. J. McInnes, S. Piligkos, G. A. Timco, and R. E. Winpenny, Coordination Chemistry Reviews **249**, 2577 (2005), ISSN 0010-8545, URL http://www.sciencedirect.com/science/article/pii/S0010854505000421.

[42] L. Engelhardt, C. Martin, R. Prozorov, M. Luban, G. A. Timco, and R. E. P. Winpenny, Phys. Rev. B **79**, 014404 (2009), URL http://link.aps.org/doi/10.1103/PhysRevB.79.014404.

[43] F. H. Spedding, C. C. Moss, and R. C. Waller, The Journal of Chemical Physics **8**, 908 (1940), URL http://link.aip.org/link/?JCP/8/908/1.

[44] V. Baskar, K. Gopal, M. Helliwell, F. Tuna, W. Wernsdorfer, and R. E. P. Winpenny, Dalton Trans. **39**, 4747 (2010), URL http://dx.doi.org/10.1039/B927114G.

[45] P. Khuntia, M. Mariani, A. V. Mahajan, A. Lascialfari, F. Borsa, T. D. Pasatoiu, and M. Andruh, Phys. Rev. B **84**, 184439 (2011), URL http://link.aps.org/doi/10.1103/PhysRevB.84.184439.

[46] X.-Q. Zhao, Y. Lan, B. Zhao, P. Cheng, C. E. Anson, and A. K. Powell, Dalton Trans. **39**, 4911 (2010), URL http://dx.doi.org/10.1039/C002841J.

[47] V. Mereacre, M. N. Akhtar, Y. Lan, A. M. Ako, R. Clerac, C. E. Anson, and A. K. Powell, Dalton Trans. **39**, 4918 (2010), URL http://dx.doi.org/10.1039/B926899E.

[48] T. D. Pasatoiu, M. Etienne, A. M. Madalan, M. Andruh, and R. Sessoli, Dalton Trans. **39**, 4802 (2010), URL http://dx.doi.org/10.1039/B925425K.

[49] R. E. P. Winpenny, Chem. Soc. Rev. **27**, 447 (1998), URL http://dx.doi.org/10.1039/A827447Z.

[50] A. Mller, Science **300**, 749 (2003), http://www.sciencemag.org/content/300/5620/749.full.pdf, URL http://www.sciencemag.org/content/300/5620/749.short.

[51] A. Mller, P. Kgerler, and A. Dress, Coordination Chemistry Reviews **222**, 193 (2001), ISSN 0010-8545, URL http://www.sciencedirect.com/science/article/pii/S0010854501003915.

[52] A. Mller, E. Krickemeyer, H. Bgge, M. Schmidtmann, and F. Peters, Angewandte Chemie International Edition **37**, 3359 (1998), ISSN 1521-3773, URL http://dx.doi.org/10.1002/(SICI)1521-3773(19981231)37:24<3359::AID-ANIE3359>3.0.CO;2-J.

[53] M. Axenovich and M. Luban, Phys. Rev. B **63**, 100407 (2001), URL http://link.aps.org/doi/10.1103/PhysRevB.63.100407.

[54] M. Exler and J. Schnack, Phys. Rev. B **67**, 094440 (2003), URL http://link.aps.org/doi/10.1103/PhysRevB.67.094440.

[55] C. Schröder, R. Prozorov, P. Kögerler, M. D. Vannette, X. Fang, M. Luban, A. Matsuo, K. Kindo, A. Müller, and A. M. Todea, Phys. Rev. B **77**, 224409 (2008), URL http://link.aps.org/doi/10.1103/PhysRevB.77.224409.

[56] A. Furrer and O. Waldmann, Rev. Mod. Phys. **85**, 367 (2013), URL http://link.aps.org/doi/10.1103/RevModPhys.85.367.

[57] V. O. Garlea, S. E. Nagler, J. L. Zarestky, C. Stassis, D. Vaknin, P. Kögerler, D. F. McMorrow, C. Niedermayer, D. A. Tennant, B. Lake, et al., Phys. Rev. B **73**, 024414 (2006), URL http://link.aps.org/doi/10.1103/PhysRevB.73.024414.

[58] P. Kogerler, B. Tsukerblat, and A. Muller, Dalton Trans. **39**, 21 (2010), URL http://dx.doi.org/10.1039/B910716A.

[59] U. Kortz, A. Mller, J. van Slageren, J. Schnack, N. S. Dalal, and M. Dressel, Coordination Chemistry Reviews **253**, 2315 (2009), ISSN 0010-8545, ¡ce:title¿Deutsche Forschungsgemeinschaft Molecular Magnetism Research Report¡/ce:title¿, URL http://www.sciencedirect.com/science/article/pii/S0010854509000101.

[60] A. Mller, S. Sarkar, S. Q. N. Shah, H. Bgge, M. Schmidtmann, S. Sarkar, P. Kgerler, B. Hauptfleisch, A. X. Trautwein, and V. Schnemann, Angewandte Chemie International Edition **38**, 3238 (1999), ISSN 1521-3773, URL http://dx.doi.org/10.1002/(SICI)1521-3773(19991102)38:21<3238::AID-ANIE3238>3.0.CO;2-6.

[61] A. Mller, M. Luban, C. Schrder, R. Modler, P. Kgerler, M. Axenovich, J. Schnack, P. Canfield, S. Bud'ko, and N. Harrison, ChemPhysChem **2**, 517 (2001), ISSN 1439-7641, URL http://dx.doi.org/10.1002/1439-7641(20010917)2:8/9<517::AID-CPHC517>3.0.CO;2-1.

[62] M. Hasegawa and H. Shiba, Journal of the Physical Society of Japan **73**, 2543 (2004), URL http://jpsj.ipap.jp/link?JPSJ/73/2543/.

[63] A. Todea, A. Merca, H. Bgge, J. van?Slageren, M. Dressel, L. Engelhardt, M. Luban, T. Glaser, M. Henry, and A. Mller, Angewandte Chemie International Edition **46**, 6106 (2007), ISSN 1521-3773, URL http://dx.doi.org/10.1002/anie.200700795.

[64] A. Mller, A. M. Todea, J. van Slageren, M. Dressel, H. Bgge, M. Schmidtmann, M. Luban, L. Engelhardt, and M. Rusu, Angewandte Chemie International Edition **44**, 3857 (2005), ISSN 1521-3773, URL http://dx.doi.org/10.1002/anie.200500697.

[65] B. Botar, P. Kogerler, and C. L. Hill, Chem. Commun. **0**, 3138 (2005), URL http://dx.doi.org/10.1039/B504491J.

[66] A. M. Todea, A. Merca, H. Bogge, T. Glaser, L. Engelhardt, R. Prozorov, M. Luban, and A. Muller, Chem. Commun. **0**, 3351 (2009), URL http://dx.doi.org/10.1039/B907188A.

[67] J. Schnack, Dalton Trans. **39**, 4677 (2010), URL http://dx.doi.org/10.1039/B925358K.

[68] A. Ramirez, Annu. Rev. Mater. Sci **24**, 453 (1994).

[69] J. E. Greedan, J. Mater. Chem. **11**, 37 (2001), URL http://dx.doi.org/10.1039/B003682J.

[70] R. Moessner, Canadian Journal of Physics **79**, 1283 (2001), http://www.nrcresearchpress.com/doi/pdf/10.1139/p01-123, URL http://www.nrcresearchpress.com/doi/abs/10.1139/p01-123.

[71] H.-J. Schmidt, J. Richter, and R. Moessner, Journal of Physics A: Mathematical and General **39**, 10673 (2006), URL http://stacks.iop.org/0305-4470/39/i=34/a=006.

[72] R. Moessner, Journal of Physics: Conference Series **145**, 012001 (2009), URL http://stacks.iop.org/1742-6596/145/i=1/a=012001.

[73] I. Rousochatzakis, A. M. Läuchli, and F. Mila, Phys. Rev. B **77**, 094420 (2008), URL http://link.aps.org/doi/10.1103/PhysRevB.77.094420.

[74] J. A. Quilliam, F. Bert, R. H. Colman, D. Boldrin, A. S. Wills, and P. Mendels, Phys. Rev. B **84**, 180401 (2011), URL http://link.aps.org/doi/10.1103/PhysRevB.84.180401.

[75] J. Schnack, H.-J. Schmidt, J. Richter, and J. Schulenburg, The European Physical Journal B - Condensed Matter and Complex Systems **24**, 475 (2001), ISSN 1434-6028, URL http://dx.doi.org/10.1007/s10051-001-8701-6.

[76] J. Schulenburg, A. Honecker, J. Schnack, J. Richter, and H.-J. Schmidt, Phys. Rev. Lett. **88**, 167207 (2002), URL http://link.aps.org/doi/10.1103/PhysRevLett.88.167207.

[77] C. Schröder, H. Nojiri, J. Schnack, P. Hage, M. Luban, and P. Kögerler, Phys. Rev. Lett. **94**, 017205 (2005), URL http://link.aps.org/doi/10.1103/PhysRevLett.94.017205.

[78] J. Schnack, R. Schmidt, and J. Richter, Phys. Rev. B **76**, 054413 (2007), URL http://link.aps.org/doi/10.1103/PhysRevB.76.054413.

[79] M. E. Zhitomirsky, Phys. Rev. B **67**, 104421 (2003), URL http://link.aps.org/doi/10.1103/PhysRevB.67.104421.

[80] C. Schrder, X. Fang, Y. Furukawa, M. Luban, R. Prozorov, F. Borsa, and K. Kumagai, Journal of Physics: Condensed Matter **22**, 216007 (2010), URL http://stacks.iop.org/0953-8984/22/i=21/a=216007.

[81] P. Henelius and A. W. Sandvik, Phys. Rev. B **62**, 1102 (2000), URL http://link.aps.org/doi/10.1103/PhysRevB.62.1102.

[82] S. A. Reisinger, C. C. Tang, S. P. Thompson, F. D. Morrison, and P. Lightfoot, Chemistry of Materials **23**, 4234 (2011), http://pubs.acs.org/doi/pdf/10.1021/cm201762f, URL http://pubs.acs.org/doi/abs/10.1021/cm201762f.

[83] H. Yoshida, Y. Michiue, E. Takayama-Muromachi, and M. Isobe, J. Mater. Chem. **22**, 18793 (2012), URL http://dx.doi.org/10.1039/C2JM32250A.

[84] T. Kambe, Y. Nogami, K. Oshima, W. Fujita, and K. Awaga, Journal of the Physical Society of Japan **73**, 796 (2004), URL http://jpsj.ipap.jp/link?JPSJ/73/796/.

[85] J. K. Jung, D. Procissi, R. Vincent, B. J. Suh, F. Borsa, P. Kögerler, C. Schröder, and M. Luban, Journal of Applied Physics **91**, 7388 (2002), URL http://link.aip.org/link/?JAP/91/7388/1.

[86] J. Lago, E. Micotti, M. Corti, A. Lascialfari, A. Bianchi, S. Carretta, P. Santini, D. Procissi, S. H. Baek, P. Kögerler, et al., Phys. Rev. B **76**, 064432 (2007), URL http://link.aps.org/doi/10.1103/PhysRevB.76.064432.

[87] G. C. Carter, L. H. Bennett, and K. K. Kahan, *Metallic Shift in NMR* ((Pergamon, New York), 1977).

[88] Y. Furukawa, Y. Nishisaka, K.-i. Kumagai, P. Kögerler, and F. Borsa, Phys. Rev. B **75**, 220402 (2007), URL http://link.aps.org/doi/10.1103/PhysRevB.75.220402.

[89] S. H. Baek, M. Luban, A. Lascialfari, E. Micotti, Y. Furukawa, F. Borsa, J. van Slageren, and A. Cornia, Phys. Rev. B **70**, 134434 (2004), URL http://link.aps.org/doi/10.1103/PhysRevB.70.134434.

[90] A. L. F. Borsa, Y. Furukawa, *Novel NMR and EPR Techniques* ((Springer, New York), 2006).

[91] P. Santini, S. Carretta, E. Liviotti, G. Amoretti, P. Carretta, M. Filibian, A. Lascialfari, and E. Micotti, Phys. Rev. Lett. **94**, 077203 (2005), URL http://link.aps.org/doi/10.1103/PhysRevLett.94.077203.

[92] I. Rousochatzakis, Phys. Rev. B **76**, 214431 (2007), URL http://link.aps.org/doi/10.1103/PhysRevB.76.214431.

[93] I. Rousochatzakis, A. Läuchli, F. Borsa, and M. Luban, Phys. Rev. B **79**, 064421 (2009), URL http://link.aps.org/doi/10.1103/PhysRevB.79.064421.

[94] D. C. Johnston, Advances in Physics **59**, 803 (2010).

[95] A. Hellmann, A. Löhken, A. Wurth, and A. Mewis, Z. Naturforsch **62b**, 155 (2007).

[96] Y. Singh, A. Ellern, and D. C. Johnston, Phys. Rev. B **79**, 094519 (2009), URL http://link.aps.org/doi/10.1103/PhysRevB.79.094519.

[97] Y. Singh, M. A. Green, Q. Huang, A. Kreyssig, R. J. McQueeney, D. C. Johnston, and A. I. Goldman, Phys. Rev. B **80**, 100403 (2009), URL http://link.aps.org/doi/10.1103/PhysRevB.80.100403.

[98] D. C. Johnston, R. J. McQueeney, B. Lake, A. Honecker, M. E. Zhitomirsky, R. Nath, Y. Furukawa, V. P. Antropov, and Y. Singh, Phys. Rev. B **84**, 094445 (2011), URL http://link.aps.org/doi/10.1103/PhysRevB.84.094445.

[99] A. Pandey, R. S. Dhaka, J. Lamsal, Y. Lee, V. K. Anand, A. Kreyssig, T. W. Heitmann, R. J. McQueeney, A. I. Goldman, B. N. Harmon, et al., Phys. Rev. Lett. **108**, 087005 (2012), URL http://link.aps.org/doi/10.1103/PhysRevLett.108.087005.

[100] A. T. Satya, A. Mani, A. Arulraj, N. V. C. Shekar, K. Vinod, C. S. Sundar, and A. Bharathi, Phys. Rev. B **84**, 180515 (2011), URL http://link.aps.org/doi/10.1103/PhysRevB.84.180515.

[101] J. Lamsal, G. S. Tucker, T. W. Heitmann, A. Kreyssig, A. Jesche, A. Pandey, W. Tian, R. J. McQueeney, D. C. Johnston, and A. I. Goldman, ArXiv e-prints (2013), 1303.7420.

[102] J.-K. Bao, H. Jiang, Y.-L. Sun, W.-H. Jiao, C.-Y. Shen, H.-J. Guo, Y. Chen, C.-M. Feng, H.-Q. Yuan, Z.-A. Xu, et al., Phys. Rev. B **85**, 144523 (2012), URL http://link.aps.org/doi/10.1103/PhysRevB.85.144523.

[103] A. J. Freeman and R. E. Watson, *Magnetism* (Academic Press, New York, 1965).

[104] S. Pinjare and K. R. Rao, Journal of Magnetism and Magnetic Materials **30**, 27 (1982), ISSN 0304-8853, URL http://www.sciencedirect.com/science/article/pii/0304885382900051.

[105] A. Narath, Physicsal Review **162**, 320 (1967).

[106] W. W. Simmons, W. J. O'Sullivan, and W. A. Robinson, Phys. Rev. **127**, 1168 (1962), URL http://link.aps.org/doi/10.1103/PhysRev.127.1168.

[107] D. Beeman and P. Pincus, Phys. Rev. **166**, 359 (1968), URL http://link.aps.org/doi/10.1103/PhysRev.166.359.

[108] Y. Furukawa, I. Okamura, K. Kumagai, T. Goto, T. Fukase, Y. Taguchi, and Y. Tokura, Phys. Rev. B **59**, 10550 (1999), URL http://link.aps.org/doi/10.1103/PhysRevB.59.10550.

[109] M. Rotter, M. Tegel, and D. Johrendt, Phys. Rev. Lett. **101**, 107006 (2008), URL http://link.aps.org/doi/10.1103/PhysRevLett.101.107006.

[110] K. Sasmal, B. Lv, B. Lorenz, A. M. Guloy, F. Chen, Y.-Y. Xue, and C.-W. Chu, Phys. Rev. Lett. **101**, 107007 (2008), URL http://link.aps.org/doi/10.1103/PhysRevLett.101.107007.

[111] P. M. Shirage, K. Miyazawa, H. Kito, H. Eisaki, and A. Iyo, Applied Physics Express **1**, 081702 (2008), URL http://apex.jsap.jp/link?APEX/1/081702/.

[112] A. S. Sefat, R. Jin, M. A. McGuire, B. C. Sales, D. J. Singh, and D. Mandrus, Phys. Rev. Lett. **101**, 117004 (2008), URL http://link.aps.org/doi/10.1103/PhysRevLett.101.117004.

[113] N. Kumar, R. Nagalakshmi, R. Kulkarni, P. L. Paulose, A. K. Nigam, S. K. Dhar, and A. Thamizhavel, Phys. Rev. B **79**, 012504 (2009), URL http://link.aps.org/doi/10.1103/PhysRevB.79.012504.

[114] S. Jiang, H. Xing, G. Xuan, C. Wang, Z. Ren, C. Feng, J. Dai, Z. Xu, and G. Cao, Journal of Physics: Condensed Matter **21**, 382203 (2009), URL http://stacks.iop.org/0953-8984/21/i=38/a=382203.

[115] Z. Ren, Q. Tao, S. Jiang, C. Feng, C. Wang, J. Dai, G. Cao, and Z. Xu, Phys. Rev. Lett. **102**, 137002 (2009), URL http://link.aps.org/doi/10.1103/PhysRevLett.102.137002.

[116] H. L. Shi, H. X. Yang, H. F. Tian, J. B. Lu, Z. W. Wang, Y. B. Qin, Y. J. Song, and J. Q. Li, Journal of Physics: Condensed Matter **22**, 125702 (2010), URL http://stacks.iop.org/0953-8984/22/i=12/a=125702.

[117] S. Kasahara, T. Shibauchi, K. Hashimoto, Y. Nakai, H. Ikeda, T. Terashima, and Y. Matsuda, Phys. Rev. B **83**, 060505 (2011), URL http://link.aps.org/doi/10.1103/PhysRevB.83.060505.

[118] R. L. G. J. Paglione, Nat. Phys. **6**, 645 (2010).

[119] D. C. Johnston, Advances in Physics **59**, 803 (2010).

[120] G. R. Stewart, Rev. Mod. Phys. **83**, 1589 (2011), URL http://link.aps.org/doi/10.1103/RevModPhys.83.1589.

[121] L. Taillefer, Annual Review of Condensed Matter Physics **1**, 51 (2010), http://www.annualreviews.org/doi/pdf/10.1146/annurev-conmatphys-070909-104117, URL http://www.annualreviews.org/doi/abs/10.1146/annurev-conmatphys-070909-104117.

[122] M. A. Tanatar, N. Spyrison, K. Cho, E. C. Blomberg, G. Tan, P. Dai, C. Zhang, and R. Prozorov, Phys. Rev. B **85**, 014510 (2012), URL http://link.aps.org/doi/10.1103/PhysRevB.85.014510.

[123] N. Spyrison, M. A. Tanatar, K. Cho, Y. Song, P. Dai, C. Zhang, and R. Prozorov, Phys. Rev. B **86**, 144528 (2012), URL http://link.aps.org/doi/10.1103/PhysRevB.86.144528.

[124] I. R. Fisher, L. Degiorgi, and Z. X. Shen, Reports on Progress in Physics **74**, 124506 (2011), URL http://stacks.iop.org/0034-4885/74/i=12/a=124506.

[125] P. J. Hirschfeld, M. M. Korshunov, and I. I. Mazin, Reports on Progress in Physics **74**, 124508 (2011), URL http://stacks.iop.org/0034-4885/74/i=12/a=124508.

[126] R. Prozorov and V. G. Kogan, Reports on Progress in Physics **74**, 124505 (2011), URL http://stacks.iop.org/0034-4885/74/i=12/a=124505.

[127] R. T. Gordon, C. Martin, H. Kim, N. Ni, M. A. Tanatar, J. Schmalian, I. I. Mazin, S. L. Bud'ko, P. C. Canfield, and R. Prozorov, Phys. Rev. B **79**, 100506 (2009), URL http://link.aps.org/doi/10.1103/PhysRevB.79.100506.

[128] C. Martin, H. Kim, R. T. Gordon, N. Ni, V. G. Kogan, S. L. Bud'ko, P. C. Canfield, M. A. Tanatar, and R. Prozorov, Phys. Rev. B **81**, 060505 (2010), URL http://link.aps.org/doi/10.1103/PhysRevB.81.060505.

[129] M. A. Tanatar, J.-P. Reid, H. Shakeripour, X. G. Luo, N. Doiron-Leyraud, N. Ni, S. L. Bud'ko, P. C. Canfield, R. Prozorov, and L. Taillefer, Phys. Rev. Lett. **104**, 067002 (2010), URL http://link.aps.org/doi/10.1103/PhysRevLett.104.067002.

[130] S. L. Bud'ko, N. Ni, and P. C. Canfield, Phys. Rev. B **79**, 220516 (2009), URL http://link.aps.org/doi/10.1103/PhysRevB.79.220516.

[131] J. S. Kim, B. D. Faeth, Y. Wang, P. J. Hirschfeld, G. R. Stewart, K. Gofryk, F. Ronning, A. S. Sefat, K. Y. Choi, and K. H. Kim, Phys. Rev. B **86**, 014513 (2012), URL http://link.aps.org/doi/10.1103/PhysRevB.86.014513.

[132] J. S. Kim, B. D. Faeth, and G. R. Stewart, Phys. Rev. B **86**, 054509 (2012), URL http://link.aps.org/doi/10.1103/PhysRevB.86.054509.

[133] G. Mu, J. Tang, Y. Tanabe, J. Xu, S. Heguri, and K. Tanigaki, Phys. Rev. B **84**, 054505 (2011), URL http://link.aps.org/doi/10.1103/PhysRevB.84.054505.

[134] J.-P. Reid, A. Juneau-Fecteau, R. T. Gordon, S. R. de Cotret, N. Doiron-Leyraud, X. G. Luo, H. Shakeripour, J. Chang, M. A. Tanatar, H. Kim, et al., Superconductor Science and Technology **25**, 084013 (2012), URL http://stacks.iop.org/0953-2048/25/i=8/a=084013.

[135] K. Cho, M. A. Tanatar, N. Spyrison, H. Kim, Y. Song, P. Dai, C. L. Zhang, and R. Prozorov, Phys. Rev. B **86**, 020508 (2012), URL http://link.aps.org/doi/10.1103/PhysRevB.86.020508.

[136] K. Cho, M. A. Tanatar, H. Kim, W. E. Straszheim, N. Ni, R. J. Cava, and R. Prozorov, Phys. Rev. B **85**, 020504 (2012), URL http://link.aps.org/doi/10.1103/PhysRevB.85.020504.

[137] S. Kasahara, T. Shibauchi, K. Hashimoto, K. Ikada, S. Tonegawa, R. Okazaki, H. Shishido, H. Ikeda, H. Takeya, K. Hirata, et al., Phys. Rev. B **81**, 184519 (2010), URL http://link.aps.org/doi/10.1103/PhysRevB.81.184519.

[138] K. Hashimoto, K. Cho, T. Shibauchi, S. Kasahara, Y. Mizukami, R. Katsumata, Y. Tsuruhara, T. Terashima, H. Ikeda, M. A. Tanatar, et al., Science **336**, 1554 (2012), http://www.sciencemag.org/content/336/6088/1554.full.pdf, URL http://www.sciencemag.org/content/336/6088/1554.abstract.

[139] T. Dulguun, H. Mukuda, T. Kobayashi, F. Engetsu, H. Kinouchi, M. Yashima, Y. Kitaoka, S. Miyasaka, and S. Tajima, Phys. Rev. B **85**, 144515 (2012), URL http://link.aps.org/doi/10.1103/PhysRevB.85.144515.

[140] H. Takahashi, T. Okada, Y. Imai, K. Kitagawa, K. Matsubayashi, Y. Uwatoko, and A. Maeda, Phys. Rev. B **86**, 144525 (2012), URL http://link.aps.org/doi/10.1103/PhysRevB.86.144525.

[141] N. Ni, M. E. Tillman, J.-Q. Yan, A. Kracher, S. T. Hannahs, S. L. Bud'ko, and P. C. Canfield, Phys. Rev. B **78**, 214515 (2008), URL http://link.aps.org/doi/10.1103/PhysRevB.78.214515.

[142] M. Kano, Y. Kohama, D. Graf, F. Balakirev, A. S. Sefat, M. A. Mcguire, B. C. Sales, D. Mandrus, and S. W. Tozer, Journal of the Physical Society of Japan **78**, 084719 (2009), URL http://jpsj.ipap.jp/link?JPSJ/78/084719/.

[143] H. Kim, M. A. Tanatar, Y. J. Song, Y. S. Kwon, and R. Prozorov, Phys. Rev. B **83**, 109903 (2011), URL http://link.aps.org/doi/10.1103/PhysRevB.83.109903.

[144] M. A. Tanatar, J.-P. Reid, S. René de Cotret, N. Doiron-Leyraud, F. Laliberté, E. Hassinger, J. Chang, H. Kim, K. Cho, Y. J. Song, et al., Phys. Rev. B **84**, 054507 (2011), URL http://link.aps.org/doi/10.1103/PhysRevB.84.054507.

[145] H. Fukazawa, T. Yamazaki, K. Kondo, Y. Kohori, N. Takeshita, P. M. Shirage, K. Kihou, K. Miyazawa, H. Kito, H. Eisaki, et al., Journal of the Physical Society of Japan **78**, 033704 (2009), URL http://jpsj.ipap.jp/link?JPSJ/78/033704/.

[146] J. K. Dong, S. Y. Zhou, T. Y. Guan, H. Zhang, Y. F. Dai, X. Qiu, X. F. Wang, Y. He, X. H. Chen, and S. Y. Li, Phys. Rev. Lett. **104**, 087005 (2010), URL http://link.aps.org/doi/10.1103/PhysRevLett.104.087005.

[147] K. Hashimoto, A. Serafin, S. Tonegawa, R. Katsumata, R. Okazaki, T. Saito, H. Fukazawa, Y. Kohori, K. Kihou, C. H. Lee, et al., Phys. Rev. B **82**, 014526 (2010), URL http://link.aps.org/doi/10.1103/PhysRevB.82.014526.

[148] J. S. Kim, E. G. Kim, G. R. Stewart, X. H. Chen, and X. F. Wang, Phys. Rev. B **83**, 172502 (2011), URL http://link.aps.org/doi/10.1103/PhysRevB.83.172502.

[149] J.-P. Reid, M. A. Tanatar, A. Juneau-Fecteau, R. T. Gordon, S. R. de Cotret, N. Doiron-Leyraud, T. Saito, H. Fukazawa, Y. Kohori, K. Kihou, et al., Phys. Rev. Lett. **109**, 087001 (2012), URL http://link.aps.org/doi/10.1103/PhysRevLett.109.087001.

[150] K. Okazaki, Y. Ota, Y. Kotani, W. Malaeb, Y. Ishida, T. Shimojima, T. Kiss, S. Watanabe, C.-T. Chen, K. Kihou, et al., Science **337**, 1314 (2012), http://www.sciencemag.org/content/337/6100/1314.full.pdf, URL http://www.sciencemag.org/content/337/6100/1314.abstract.

[151] N. Kurita, K. Kitagawa, K. Matsubayashi, A. Kismarahardja, E.-S. Choi, J. S. Brooks, Y. Uwatoko, S. Uji, and T. Terashima, Journal of the Physical Society of Japan **80**, 013706 (2011), URL http://jpsj.ipap.jp/link?JPSJ/80/013706/.

[152] J. L. Zhang, L. Jiao, F. F. Balakirev, X. C. Wang, C. Q. Jin, and H. Q. Yuan, Phys. Rev. B **83**, 174506 (2011), URL http://link.aps.org/doi/10.1103/PhysRevB.83.174506.

[153] S. K. Goh, Y. Nakai, K. Ishida, L. E. Klintberg, Y. Ihara, S. Kasahara, T. Shibauchi, Y. Matsuda, and T. Terashima, Phys. Rev. B **82**, 094502 (2010), URL http://link.aps.org/doi/10.1103/PhysRevB.82.094502.

[154] S. Chong, S. Hashimoto, and K. Kadowaki, Solid State Communications **150**, 1178 (2010), ISSN 0038-1098, URL http://www.sciencedirect.com/science/article/pii/S0038109810002358.

[155] C. Chaparro, L. Fang, H. Claus, A. Rydh, G. W. Crabtree, V. Stanev, W. K. Kwok, and U. Welp, Phys. Rev. B **85**, 184525 (2012), URL http://link.aps.org/doi/10.1103/PhysRevB.85.184525.

[156] S. Yeninas, M. A. Tanatar, J. Murphy, C. P. Strehlow, O. E. Ayala-Valenzuela, R. D. McDonald, U. Welp, W. K. Kwok, T. Kobayashi, S. Miyasaka, et al., Phys. Rev. B **87**, 094503 (2013), URL http://link.aps.org/doi/10.1103/PhysRevB.87.094503.

[157] M. A. Tanatar, N. Ni, S. L. Budko, P. C. Canfield, and R. Prozorov, Superconductor Science and Technology **23**, 054002 (2010), URL http://stacks.iop.org/0953-2048/23/i=5/a=054002.

[158] M. Tanatar, K. Hashimoto, S. Kasahara, T. Shibauchi, Y. Matsuda, and R. Prozorov, Phys. Rev. B (2013).

[159] N. R. Werthamer, E. Helfand, and P. C. Hohenberg, Phys. Rev. **147**, 295 (1966), URL http://link.aps.org/doi/10.1103/PhysRev.147.295.

[160] A. M. Clogston, Phys. Rev. Lett. **9**, 266 (1962), URL http://link.aps.org/doi/10.1103/PhysRevLett.9.266.

[161] M. A. Tanatar, N. Ni, C. Martin, R. T. Gordon, H. Kim, V. G. Kogan, G. D. Samolyuk, S. L. Bud'ko, P. C. Canfield, and R. Prozorov, Phys. Rev. B **79**, 094507 (2009), URL http://link.aps.org/doi/10.1103/PhysRevB.79.094507.

[162] V. G. Kogan and R. Prozorov, Reports on Progress in Physics **75**, 114502 (2012), URL http://stacks.iop.org/0034-4885/75/i=11/a=114502.

[163] A. Gurevich, Reports on Progress in Physics **74**, 124501 (2011), URL http://stacks.iop.org/0034-4885/74/i=12/a=124501.

[164] L. Gor'kov, Sov. Sci. Rev. A Phys. **1** (1987).

[165] M. Gooch, B. Lv, J. H. Tapp, Z. Tang, B. Lorenz, A. M. Guloy, and P. C. W. Chu, EPL (Europhysics Letters) **85**, 27005 (2009), URL http://stacks.iop.org/0295-5075/85/i=2/a=27005.

[166] W. Dai, V. Ferrando, A. V. Pogrebnyakov, R. H. T. Wilke, K. Chen, X. Weng, J. Redwing, C. W. Bark, C.-B. Eom, Y. Zhu, et al., Superconductor Science and Technology **24**, 125014 (2011), URL http://stacks.iop.org/0953-2048/24/i=12/a=125014.

[167] A. Yamamoto, J. Jaroszynski, C. Tarantini, L. Balicas, J. Jiang, A. Gurevich, D. C. Larbalestier, R. Jin, A. S. Sefat, M. A. McGuire, et al., Applied Physics Letters **94**, 062511 (pages 3) (2009), URL http://link.aip.org/link/?APL/94/062511/1.

[168] C. Tarantini, A. Gurevich, J. Jaroszynski, F. Balakirev, E. Bellingeri, I. Pallecchi, C. Ferdeghini, B. Shen, H. H. Wen, and D. C. Larbalestier, Phys. Rev. B **84**, 184522 (2011), URL http://link.aps.org/doi/10.1103/PhysRevB.84.184522.

[169] T. Shibauchi, L. Krusin-Elbaum, Y. Kasahara, Y. Shimono, Y. Matsuda, R. D. McDonald, C. H. Mielke, S. Yonezawa, Z. Hiroi, M. Arai, et al., Phys. Rev. B **74**, 220506 (2006), URL http://link.aps.org/doi/10.1103/PhysRevB.74.220506.

[170] S. Kamiya, Y. Shimojo, M. A. Tanatar, T. Ishiguro, H. Yamochi, and G. Saito, Phys. Rev. B **65**, 134510 (2002), URL http://link.aps.org/doi/10.1103/PhysRevB.65.134510.

[171] Y. Shimojo, S. Kamiya, M. Tanatar, E. Ohmichi, A. Kovalev, T. Ishiguro, H. Yamochi, G. Saito, J. Yamada, H. Anzai, et al., Synthetic Metals **133134**, 197 (2003), ISSN 0379-6779, URL http://www.sciencedirect.com/science/article/pii/S0379677902004071.

[172] A. E. Kovalev, T. Ishiguro, T. Kondo, and G. Saito, Phys. Rev. B **62**, 103 (2000), URL http://link.aps.org/doi/10.1103/PhysRevB.62.103.

[173] T. Ishiguro, J. Phys. IV France **10**, 3 (2000).

[174] P. Fulde and R. A. Ferrell, Phys. Rev. **135**, A550 (1964), URL http://link.aps.org/doi/10.1103/PhysRev.135.A550.

[175] M. A. Tanatar, T. Ishiguro, H. Tanaka, and H. Kobayashi, Phys. Rev. B **66**, 134503 (2002), URL http://link.aps.org/doi/10.1103/PhysRevB.66.134503.